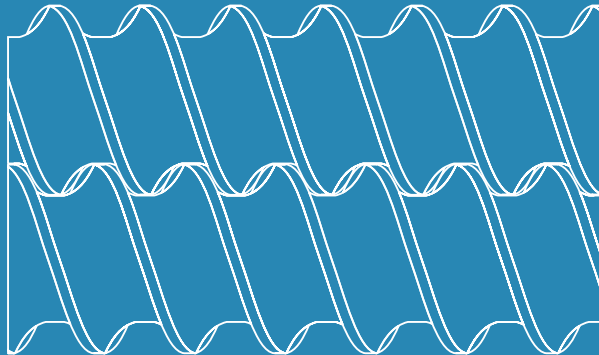
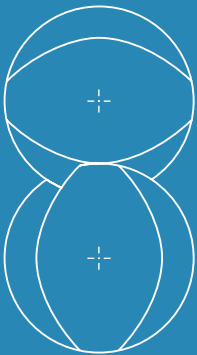
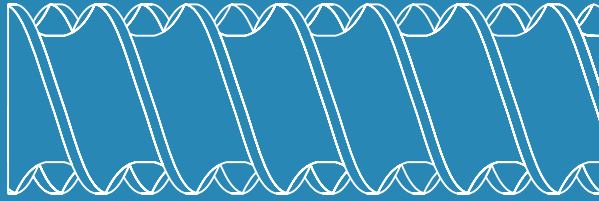


5.



6. Conclusions and recommendations
5. Three-dimensional periodic flows in dynamic devices
4. Three-dimensional space-periodic flows in static devices
3. Three-dimensional time-periodic prototype flows
2. Two-dimensional time-periodic prototype flows
1. Introduction

Analysis and Optimization of Laminar Mixing.

*Design, Development and Application
of the Mapping Method.*

Peter Kruijt

A5

Analysis and Optimization of Laminar Mixing

**Design, Development and Application
of the Mapping Method**

CIP-DATA LIBRARY TECHNISCHE UNIVERSITEIT EINDHOVEN

Kruijt, Pieter G. M.

Analysis and optimization of laminar mixing : design, development and application of the mapping method / by Pieter G.M. Kruijt. – Eindhoven: Technische Universiteit Eindhoven, 2000. – Proefschrift. Thesis – 110p.– with references – with summary in Dutch.

ISBN 90-386-2991-5

NUGI 841

Trefwoorden: menging / polymeerverwerking ; menging / menging ; numerieke analyse

Subject headings: mixing / polymer processing ; mixing / mixing ; numerical analysis

Copyright © 2000 P.G.M. Kruijt

All rights reserved. No part of this book may be reproduced, stored in a database or retrieval system, or published, in any form or in any way, electronically, mechanically, by print, photoprint, microfilm or any other means without prior written permission of the author.

This thesis was prepared with the $\text{\LaTeX} 2_{\epsilon}$ document preparation system.

Printed in the Netherlands

This research was financially supported by the Dutch Technology Foundation STW; grant no. EWT 44.3453

Analysis and Optimization of Laminar Mixing

**Design, Development and Application
of the Mapping Method**

Proefschrift

ter verkrijging van de graad van doctor aan de
Technische Universiteit Eindhoven,
op gezag van de Rector Magnificus, prof.dr. M. Rem,
voor een commissie aangewezen door het
College voor Promoties
in het openbaar te verdedigen op
dinsdag 5 september 2000 om 16.00 uur

door

Pieter Gijsbertus Maria Kruijt

geboren te Gilze en Rijen

Dit proefschrift is goedgekeurd door de promotoren:

prof.dr.ir. H.E.H. Meijer
en
prof.dr.ir. G.J.F. van Heijst

Copromotor:

dr.ir. G.W.M. Peters

Contents

1. <i>Introduction</i>	1
1.1 Problem definition	1
1.2 Current methods and their shortcomings	2
1.3 Approach to solve complex mixing problems	4
1.4 Lay-out of this thesis	4
2. <i>Two-dimensional time-periodic prototype flows</i>	7
2.1 Introduction	7
2.2 Poincaré methods	8
2.3 Adaptive boundary tracking	9
2.4 Mapping approach	10
2.4.1 Basics of the mapping method	10
2.4.2 Comparison of mapping with traditional methods	13
2.5 Long term mixing behaviour; optimization	15
2.6 Mapping of morphology	20
2.7 Conclusions and discussion	22
3. <i>Three-dimensional time-periodic prototype flows</i>	25
3.1 Introduction	25
3.2 Computational method and boundary conditions	25
3.3 Three-dimensional mapping approach	26
3.4 Verification	28
3.5 Results	29
3.5.1 Influence of spatial discretization	29
3.5.2 Comparison of mixing protocols	31
3.6 Conclusions and discussion	35
4. <i>Three-dimensional space-periodic flows in static devices</i>	37
4.1 Introduction; the multiflux static mixer	37
4.2 Computational method and boundary conditions	38
4.3 Determination of the mapping matrix	39
4.4 Results	42
4.5 Conclusions and discussion	44
5. <i>Three-dimensional periodic flows in dynamic devices</i>	47
5.1 Introduction; co-rotating twin screw extruders	47
5.2 Time- and space-periodicity	48

5.3	Geometry of the screw	50
5.4	Computational method and boundary conditions	50
5.5	Determination of the mapping matrix	52
5.6	Results	56
5.7	Conclusions and discussion	63
6.	<i>Conclusions and Recommendations</i>	67
6.1	Conclusions	67
6.2	Recommendations	68
A.	<i>Mixing measures</i>	71
B.	<i>Boundary and surface tracking</i>	75
B.1	Adaptive boundary tracking in two dimensions	75
B.2	Adaptive boundary tracking in three dimensions	75
B.3	Determination of intersecting areas and volumes	77
C.	<i>Area tensor</i>	81
D.	<i>Converting between area tensors and droplet shape tensors</i>	85
	<i>Samenvatting</i>	95
	<i>Summary</i>	97
	<i>Acknowledgements</i>	99
	<i>Curriculum Vitae</i>	101

List of Figures

1.1	Bakers transformation.	2
1.2	Dependence of mixing behaviour on location.	3
1.3	Multiflux static mixer.	4
2.1	Cavity properties.	8
2.2	Poincaré map for $D = 8.0$	8
2.3	Deformed blob after 5 periods of motion.	9
2.4	Sub-domain advection.	10
2.5	Error propagation.	12
2.6	Coarse mesh advection in the cavity flow.	12
2.7	Comparison of mapping with the Poincaré method.	13
2.8	Influence of resolution on concentration distribution.	14
2.9	Comparison between mapping and tracking.	15
2.10	Intensity of segregation after five periods	17
2.11	Concentration distributions for different protocols.	18
2.11	(b) Figure 2.11a continued.	19
2.12	Indication of error in efficiency plots.	20
2.13	Efficiency plots for four different mixing protocols.	21
2.14	Scale of segregation plots for different protocols.	22
2.15	Evolution of concentration and trace of the area tensor.	23
3.1	Prototype mixing flow in a cubic cavity with moving front and back walls.	26
3.2	Comparison of front tracking and mapping in 3D.	28
3.3	Cross-sections on which concentration distribution is displayed and initial concentration distribution.	29
3.4	Dependence of mixing pattern on spatial resolution.	30
3.5	Evolution of intensity of segregation.	31
3.6	Comparison of different protocols with equal energy input.	33
3.7	Dependence of the mixing efficiency on dimensionless displacement.	34
3.8	Intensity of segregation vs wall displacement.	35
4.1	Two multiflux static mixer configurations.	37
4.2	Conventional and improved multiflux mixer elements.	38
4.3	Schematic representation of the subdomains in the multiflux mixer.	40
4.4	Extrapolation of untracked subdomains.	41
4.5	Concentration distributions on cross-sections in the different multiflux mixers.	43
4.6	Residence time distribution in three multiflux geometries.	44
5.1	Basic types of twin screw extruder elements.	47

5.2	Space-periodicity in a twin screw extruder.	48
5.3	Time-periodicity of a twin screw extruder.	49
5.4	Profile of a self-wiping screw pair.	51
5.5	TSE flow domain and surface description.	52
5.6	Symmetry in a transport element.	53
5.7	Volume concentration error.	54
5.8	Schematic representation of contribution to Φ_s and Φ_n	54
5.9	Residence time and point of entry determination.	55
5.10	Mapping operation on a screw.	55
5.11	Mapping configuration.	57
5.12	(a) Concentration distribution in cross-sections.	58
5.12	(b) Figure 5.12a continued.	59
5.13	Concentration distribution in the transport section.	60
5.14	Intensity of segregation along the extruder.	61
5.15	Checkerboard sizes.	61
5.16	Intensity of segregation per slice and evolution in time.	62
5.17	Residence time in cross-sections of an extruder.	63
5.18	Output and cumulative output.	64
A.1	Difference between scale of segregation S and intensity of segregation I	73
B.1	Refinement of triangles.	76
B.2	Triangle quality improvement.	77
B.3	Determination of intersected areas.	78

Chapter 1

Introduction

1.1 Problem definition

Understanding the principles of mixing of viscous fluids becomes increasingly more important since more stringent requirements are demanded from the properties of (bio-)polymer blends and food. When the principles of mixing are understood, it will be possible to design better mixers by numerically evaluating the influence of changes in mixing protocols, screw configurations or mixer geometries.

To study mixing behaviour various techniques have been proposed: residence time and strain distribution by [Tadmor & Gogos \(1979\)](#), [Hobbs & Muzzio \(1997\)](#), Poincaré maps by [Ottino \(1989\)](#), [Ling \(1994\)](#), [Jana et al. \(1994b\)](#), manifold and periodic point analysis by [Ottino \(1989\)](#), [Franjione et al. \(1989\)](#), [Franjione & Ottino \(1992\)](#), [Meleshko & Peters \(1996\)](#), [Anderson et al. \(1999\)](#) and interface tracking techniques by [Noh & Woodward \(1976\)](#), [Hirt & Nichols \(1981\)](#), [Avalosse & Crochet \(1997b\)](#), [Rudman \(1997\)](#), [Galaktionov et al. \(2000b\)](#). Most of these techniques are of an *indirect* nature, i.e. the boundary between two fluids needs to be reconstructed from related properties such as traced labels or concentration. In other cases the size or structure of manifolds is regarded as a measure of mixing performance. Optimization of mixing processes can only be solved by using *direct* techniques ([Souvaliotis et al., 1995](#)), that give the instantaneous state of a mixture in terms of relevant quantities as concentration distribution and morphology. At the macro scale, the smallest object of interest is a subdomain and the largest is the entire mixture. The smallest subdomain size should be chosen such that the relevant quantities for the mixture can be described.

In optimization of mixing flows, parameters of the flow have to be adapted and the analysis needs to be repeated. Since optimization generally requires numerous analyses, the methods listed above are not efficient, or even useless, and an improved, more engineering, method to evaluate mixing behaviour is required.

The question on how to determine mixing performance concentrates on what to do after a velocity field for a particular flow is obtained. How can this velocity field be used to analyse a number of different mixing protocols or geometries? Is it possible to regard a mixing operation as a transformation from one state to the next, as e.g. is the case with the bakers transformation, which is a repetition of stretching and folding (see figure 1.1). Following this line of thinking, solving complex mixing problems implies, as a first step, being able to break down a mixing flow into a number of independent flow domains or flow situations. Accordingly, these independent situations need to be analysed separately in such a way that they can be combined at a later stage. If it is, subsequently, possible to break down the mixing problem in a number of smaller problems, and a transformation can be determined for each

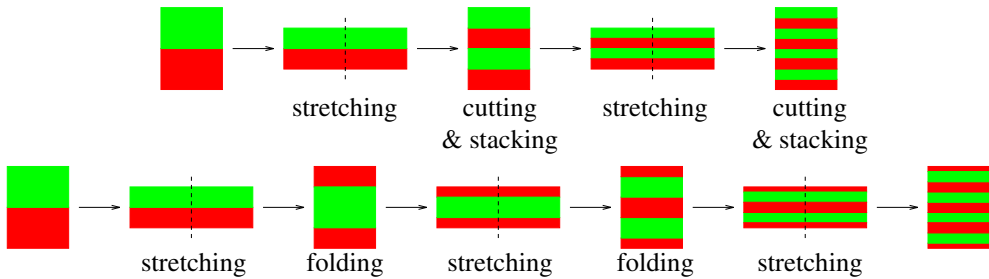


Fig. 1.1: Two schematic representations of the baker's transformation. The top figure illustrates a stretching–cutting–stacking sequence which yields 2^{n+1} layers after n operations; the bottom figure illustrates a stretch–and–fold sequence which yields $2^n + 1$ layers after n operations.

of the smaller problems, then the analysis of the mixing behaviour of the entire problem may become easier.

Based upon these considerations, the mapping method has been developed. This method describes the transformation (map) from one state of the mixture to the next. This transformation will be different for different mixing elements or flows, but once computed for different elements of e.g. an extruder, they can be combined in arbitrary order to investigate the influence of different mixing protocols or different screw configurations on mixing behaviour. A similar, but rather restrictive approach applied to the most simple problem, that of the baker's transformation, was used by [Spencer & Wiley \(1951\)](#) and describes a discrete map of the flow domain over some time-span. Methods like these have recently become attractive due to development of accurate adaptive tracking methods ([Galaktionov et al. \(1997\)](#), [Galaktionov et al. \(2000b\)](#)) and the availability of powerful computational resources.

1.2 Current methods and their shortcomings

Methods used to analyse mixing start by determining the velocity field. Once the velocity field is acquired, a number of different approaches are used. The simplest method tracks a cluster of initially closely spaced particles. After tracking these particles for an amount of time, the spatial distribution is studied ([Carey & Shen \(1995\)](#), [Hutchinson et al. \(1999\)](#)). This procedure is easy to implement and gives an indication how particles are spread through the geometry. However, these particles are passive and infinitely small and, therefore, give no indication how much fluid is convected or how the material has stretched. The final distribution is completely determined by the initial location of the cluster, but most important, however, is that spreading of particles is, in principle, not a good measure of mixing since no information on the distribution of actual fluid is computed.

To overcome the problem of infinitesimal small particles, the particle tracking method can be adapted to a boundary tracking method ([Noh & Woodward \(1976\)](#), [Hirt & Nichols \(1981\)](#), [Avalosse & Crochet \(1997a\)](#), [Avalosse & Crochet \(1997b\)](#), [Rudman \(1997\)](#), [Galaktionov et al. \(1999\)](#)). In this case the boundary of an arbitrary blob (area in two dimensions, volume in three dimensions) is tracked. Adaptive tracking is required when points describing the boundary become separated too far or the angle between three points becomes too small (e.g. in folds); points

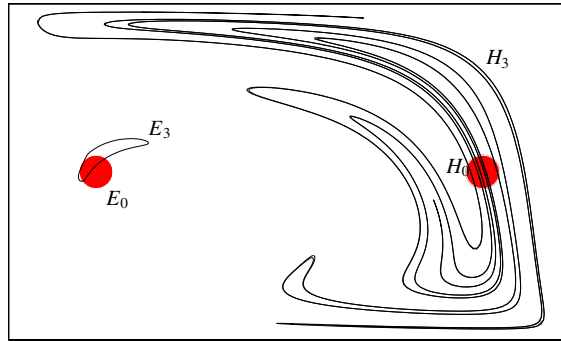


Fig. 1.2: Dependence of the initial location of marker fluid on the mixing behaviour in the flow. Blob E_0 is located in the neighbourhood of an elliptic point and after three periods is spread as indicated by E_3 . Blob H_0 is located near a hyperbolic point, and after three periods is spread much more through the cavity as indicated by H_3 .

are added in between at an earlier time-level, in order to maintain accuracy. This approach results in a description of the actual material distribution. However, the results are still largely dependent on the initial location of the blob (see figure 1.2). Also, tracking a boundary for a larger time is computationally expensive, in time as well as memory, and gradually becomes impossible given the exponential increase in surface area as obtained in the chaotic flows that characterize good mixing processes.

It is well agreed upon that the introduction of periodicity in a flow can cause the flow to behave chaotically ((Ottino, 1989), Ottino *et al.* (1992), Aref & El Naschie (1995)). Introducing chaos into a system in general results in a better mixing performance since areas of fluid are stretched and folded repeatedly. This stretching and folding occurs under the influence of periodic points, i.e. points in the fluid that return to their initial location after exactly n periods ($n \in \mathbb{N}$). These n^{th} order periodic points can be either of an elliptic, hyperbolic or parabolic nature. Elliptic periodic points are present within ‘islands’: areas of fluid that rotate around the elliptic point and slightly deform, but are surrounded by a boundary over which no fluid is exchanged. Hyperbolic periodic points are located in unstable regions of the flow: an area of fluid located around a hyperbolic point is exponentially stretched. Parabolic periodic points are the degenerate case, and are, if at all, found in two-dimensional flows only on the boundaries of the flow domain, whereas in three-dimensional flows they also exist on periodic lines where the nature of the points on that line changes from hyperbolic to elliptic.

Since periodic points clearly influence the mixing behaviour of a flow, locating and classifying them will help in understanding and evaluating the mixing efficiency of a flow. However, this is a laborious endeavour, unless, as shown by Meleshko & Peters (1996) for the two-dimensional case and Anderson *et al.* (1999) for the three-dimensional case of a lid-driven cavity, some kind of symmetry of the flow field can be used.

A simpler means to get an impression of the chaotic behaviour of a mixing flow (or periodic phenomena in general), is the Poincaré method. This method tracks a small number of points in a periodic flow and records their position after every period. These positions are cumulatively plotted in a Poincaré map. This map shows the presence and size of unmixed

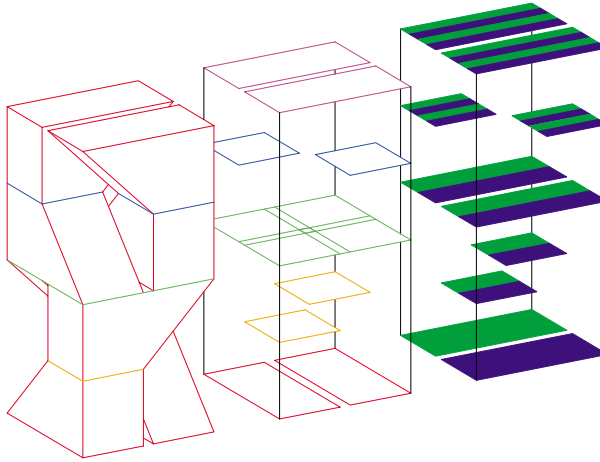


Fig. 1.3: Schematic diagram and working principle of the multiflux static mixer. The multiflux static mixer mimics the bakers transformation by continuously stretching, cutting and stacking alternating layers of fluid.

and well-mixed regions in the mixing flow. The disadvantage of the method is that it shows the long-term behaviour of the flow, that is often not reached in practice. Another drawback is that it is not well suited for open flows, although it is applicable as shown by [Ottino \(1989\)](#).

1.3 Approach to solve complex mixing problems

Comparing mixing devices requires that the quality of the resulting mixture can be quantified. Although in most cases the eye is a good sensor to determine the state of the mixture, it does not return a single value (or small set of values) that allows for comparison with other mixtures that are seemingly equally well mixed. Consequently, automated searching for a (local) maximum in mixing quality is not possible if the mixing quality is not quantified. A number of mixing measures have been proposed by e.g. [Danckwerts \(1952\)](#), [Danckwerts \(1953\)](#), [Welander \(1955\)](#), [Tucker \(1981\)](#), [Tucker \(1991\)](#). The measure to choose strongly depends on the requirements like e.g. the total the interface created, the importance of the maximum thickness of striations, or the size of unmixed regions. The variance of the concentration of one fluid in the other may be of most interest; if so, what should be the size of the sampling area or volume?

1.4 Lay-out of this thesis

In chapter 2 the different methods to analyse mixing behaviour are introduced. To this purpose, a two-dimensional prototype mixing flow is examined. This problem is based upon the well-known lid-driven cavity flow as introduced by [Chien *et al.* \(1986\)](#). On the basis of this time-periodic problem, classical methods are applied, and the mapping method is introduced

and validated. The results of the different methods are, finally, compared with experimental data.

Next, in chapter 3, the two-dimensional method will be extended to a three-dimensional, time-periodic, prototype flow: the lid-driven cubic cavity flow. Accurate boundary tracking methods (Galaktionov *et al.* (1997), Galaktionov *et al.* (2000b)) are applied and the results are compared with the results of the mapping method and experimental data.

In chapter 4, the focus is on industrially more relevant, spatially periodic flows, notably the multiflux static mixer (Sluijters, 1965). This mixer is used to create thin, alternating layers of polymer materials, and is constructed from a stacked array of channels that closely imitate the bakers transformation (see figure 1.3). In this static mixer, the flow is largely determined by the pressure distribution over the elements. In order to optimize for layer thickness, a number of variations on the original design have been proposed by van der Hoeven *et al.* (2000). The influence of these adjustments on layer thickness and residence time distribution is investigated using the mapping method. Using the mapping method, the layer distribution and residence time distribution are analysed for a number of stacked elements. So far, no other numerical simulations are known that are able to predict residence time and concentration distribution for more than two elements.

In chapter 5 the last, spatially periodic, mixing device considered is the co-rotating twin-screw extruder. The transport section of a twin screw extruder will be analysed to show that the mapping method is able to handle complex geometries in dynamic mixers.

Finally, in chapter 6, conclusions and recommendations for future research are discussed.

Chapter 2

Two-dimensional time-periodic prototype flows*

2.1 Introduction

In order to gain understanding in mixing behaviour in laminar flows, a two-dimensional prototype flow is examined. This flow, a lid-driven cavity flow, has already been investigated extensively by a number of groups ([Chien *et al.* \(1986\)](#), [Leong & Ottino \(1990\)](#), [Jana *et al.* \(1994a\)](#), [Chella & Viñals \(1996\)](#)). This flow can be seen as a two-dimensional representation of the flow in a single screw extruder. The properties of the cavity used are shown in figure 2.1.

In the test case of the lid-driven cavity flow the Stokes approximation is valid since inertial forces can be neglected with respect to viscous contributions. The length-to-width ratio of the cavity is 1.67 in accordance with [Leong & Ottino \(1989\)](#). Flow is induced by motion of the top or bottom wall of the cavity; the side walls are fixed (figure 2.1).

To create a chaotic flow, the top wall (T) and bottom wall (B) of the cavity move alternately with equal displacement; the top wall from left to right and the bottom wall from right to left (the TB protocol). Two parameters governing the mixing performance in this cavity are the number of wall movements n and the dimensionless displacement D that is defined as:

$$D = \frac{1}{2L} \int_0^{T_p} (v_T(t) + v_B(t)) dt, \quad (2.1)$$

where $v_T(t)$ and $v_B(t)$ are the velocity of top and bottom wall, T_p is the period time and L is the half length of the cavity. For all protocols in this thesis, the displacement of the top wall is equal to the displacement of the bottom wall.

This particular flow protocol is well examined, both experimentally and numerically, by the aforementioned authors. To describe the Newtonian velocity field, an accurate semi-analytical solution ([Meleshko, 1994](#)) is used. Periodic points, which are a key item to evaluate the mixing abilities of the flow have been found ([Meleshko & Peters, 1996](#)).

First, the Poincaré method and adaptive boundary tracking will be shortly discussed, and some typical results will be shown. Then, the mapping method will be introduced and results from the techniques mentioned will be compared to results of the mapping method to validate the technique.

* This chapter is largely based on: *Analyzing Fluid Mixing in Periodic Flows by Distribution Matrices: The Mapping Method*, PETER G. M. KRUIJT, OLEKSIY S. GALAKTIONOV, PATRICK D. ANDERSON, GERRIT W. M. PETERS, and HAN E. H. MEIJER, submitted to AIChE Journal.

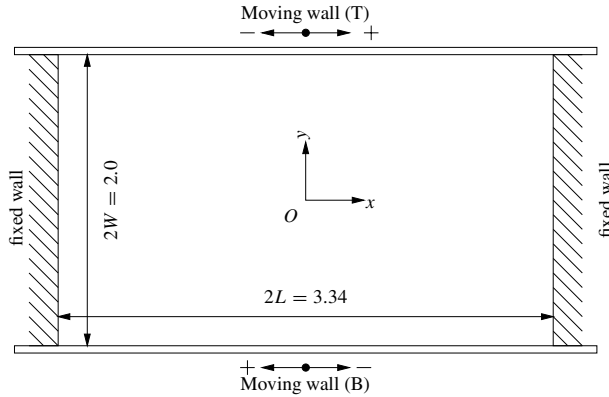


Fig. 2.1: Dimensions of the cavity and indication of positive and negative directions for wall velocities.

2.2 Poincaré methods

The Poincaré method is an easy to implement tool to investigate the long term chaotic behaviour of a periodic phenomenon or dynamical system. First, a number of random initial realizations in phase-space is chosen. They are then tracked for one period, and their new position in phase-space is recorded. This procedure is repeated for a large number of periods (typically $\gg 1000$). The realizations are then plotted as points in a phase-space diagram, which shows chaotic and regular regions.

In the case of periodic flows, the dynamical system is the flow itself, the phase-space is the flow domain, and the realizations are arbitrary locations within the flow domain. The regular areas indicate the regions (or islands) around an elliptic point. The irregular or chaotic areas indicate the regions where hyperbolic periodic points exist. The method does not indicate the number and exact location of the periodic points, it merely indicates the region in which they are located, and hence the size of their influence upon the flow. For a Newtonian fluid in a lid driven cavity flow, where the TB protocol is applied with $D = 8.0$, the Poincaré map, is depicted in figure 2.2.

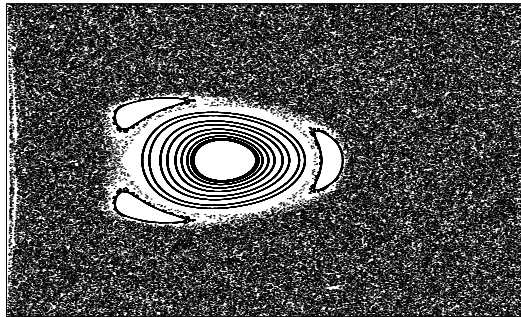


Fig. 2.2: Poincaré map for a TB protocol with $D = 8.0$ clearly showing islands in the periodic flow.

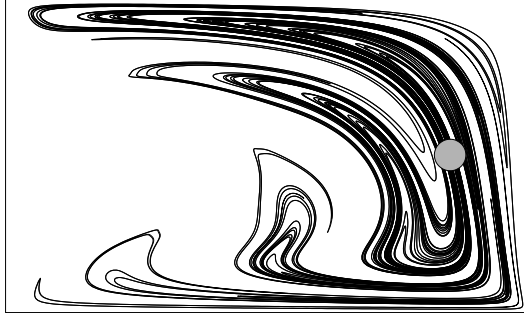


Fig. 2.3: The deformed blob after 5 periods of motion (TB protocol); the grey area around $(x, y) = (1.15, 0)$ indicates the initial blob.

Since the points in the Poincaré map do not represent a material volume or area, it is not easy to draw conclusions as to where fluid is moving. Although it is clear that fluid in the chaotic region is spread throughout the cavity, the actual concentration of e.g. a dye in the fluid is not (directly) related to the amount of realizations in that area.

2.3 Adaptive boundary tracking

To be able to predict the actual spreading of material through the cavity better, the boundary of a pre-determined region Ω with boundary Γ in the flow domain can be marked, and nodes on the circumference of this region can be tracked in time for a number of periods. This may give an indication of the stretching of the marked fluid and the concentration distribution in the flow domain. However, since time-periodic flows in general display chaotic behaviour, points initially very close together may end up on opposite parts of the flow domain. Since it may not be possible to determine beforehand which part of the boundary is extensively stretched, and which part remains almost undeformed (or is even contracted), it is not efficient to start with a large number of equidistantly spaced nodes describing the boundary of the domain.

In order to circumvent this problem, a relatively small amount of markers (nodes) describing the circumference Γ of the marked area Ω is used. During the course of tracking, nodes are inserted in between adjacent nodes where either the distance has grown beyond a certain limit (l_{1c} or l_{2c} ; see appendix B equations B.1 and B.2), or when the angle formed by three consecutive nodes is smaller than a critical α_c (equation B.4). In case of incompressible fluids, a domain Ω should be area conserving, and the error ε can be estimated by:

$$\varepsilon = \frac{\left| \int_{\Omega|_{t=t_0}} dA - \int_{\Omega|_{t=t_0+\Delta t}} dA \right|}{\int_{\Omega|_{t=t_0}} dA}. \quad (2.2)$$

If the area conservation is not within certain limits, the values for l_{1c} and l_{2c} have to be adapted.

The adaptive tracking method can be very accurate, as is shown in figure 2.3. This figure shows the advection of a blob (indicated by the grey circle) with radius $r = 0.10$ around the location $(x, y) = (1.15, 0)$, where a hyperbolic point is present. The dimensions of the

cavity are 3.34 by 2, with the location of the origin in the centre of the cavity. The initial blob is advected for five periods with a dimensionless displacement D of 6.25. The error in area conservation for this computation with 20 points initially describing the boundary, $l_{1c} = 10^{-4}$, $l_{2c} = 10^{-2}$ and $\alpha_c = \frac{2}{3}\pi$ was 0.4% (equation 2.2); the boundary is stretched approximately 1.5×10^3 times (figure 2.3).

In chaotic flows, the length of the boundary can increase exponentially (Ottino (1989), Muzzio *et al.* (1992)), and therefore the number of nodes will also increase exponentially if an accurate description of the boundary has to be maintained. Therefore, although accurate, this method is computationally expensive for analysis of even a relatively small number of periods, or flows where stretching of the boundary is extremely non-uniform, and becomes infeasible for large numbers of periods. Furthermore, if the initial location of the area to be tracked or the mixing protocol is changed, the analysis needs to be repeated.

2.4 Mapping approach

The mapping method describes the transport of a conservative quantity from one state to another by means of a so called mapping matrix. In this thesis the mapping matrix will describe the transport of fluid from one point in time to the next (closed flows), or from one cross-section to the next (open flows).

2.4.1 Basics of the mapping method

The method proposed subdivides an arbitrary domain Ω into (a large number n of) subdomains Ω_i with boundaries Γ_i . The boundaries of all subdomains are tracked from $t = t_0$ to $t = t_0 + \Delta t$. These computations are expensive, but need to be performed only *once* for every geometry and are highly parallelisable (Geist *et al.* (1994), Galaktionov *et al.* (1997)) since there is no interdependence between domain tracking computations. A distribution or

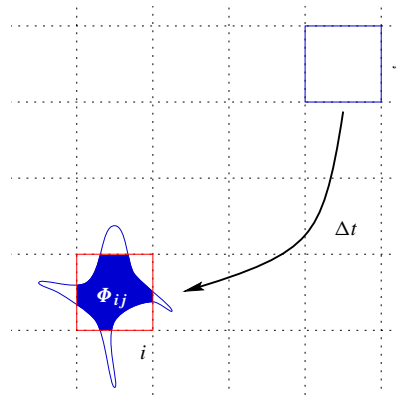


Fig. 2.4: Schematic representation of subdomain advection and determination of the coefficient Φ_{ij} ; Φ_{ij} is the part of the area of Ω_i that is advected to Ω_j

mapping matrix Φ is computed where Φ_{ij} contains the fraction of subdomain Ω_j at $t = t_0$ that is tracked to $t = t_0 + \Delta t$ and found in the domain Ω_i as it existed at $t = t_0$ (figure 2.4):

$$\Phi_{ij} = \frac{\int_{\Omega_j|_{t=t_0+\Delta t} \cap \Omega_i|_{t=t_0}} dA}{\int_{\Omega_j|_{t=t_0}} dA}. \quad (2.3)$$

The mapping matrix Φ has the following properties:

- The amount of fluid transported *from* a subdomain j equals the area A_j of the subdomain (conservation of mass). This implies:

$$\sum_{i=1}^n \Phi_{ij} = 1. \quad (2.4)$$

- The amount of fluid transported *to* a subdomain i equals the area A_i of the subdomain (again: conservation of mass). Thus:

$$\sum_{j=1}^n \Phi_{ij} A_j = A_i. \quad (2.5)$$

- Φ is sparse since, in a relatively limited time span Δt , fluid from one subdomain at the beginning or entrance of the flow, is transported to only a limited number of subdomains at the next time level (this allows for compact storage in computations).

In general, the interval Δt does not span an entire period. If optimization of a mixing protocol is required, and this includes the effect of the length of the period, then the minimum step size to compute a mapping matrix should be equal to the minimum step size that is used for varying the period time. Combination of maps with different time intervals Δt_i can be used to create the map Φ_T for some period time T :

$$\Phi_T = \prod_{i=1}^k \Phi_{\Delta t_i} \quad \text{where:} \quad \sum_{i=1}^k \Delta t_i = T. \quad (2.6)$$

However, in general Φ_T is less sparse than $\Phi_{\Delta t_i}$. When Φ is computed, a quantity that is related to the subdomains can be mapped. The chosen quantity should not influence the flow field, or its influence should at least be negligible, since otherwise the map itself would change. The method assumes a uniform distribution of the chosen quantity over an initial subdomain. This introduces a systematic error in the method: separate contributions of different subdomains at $t = t_0$ to a certain subdomain at $t = t_0 + \Delta t$ are averaged in that subdomain. Since the state after one map defines the new state for the next map, this error propagates as is schematically shown in figure 2.5. However, it will be shown that if the subdomains are small enough, the method still provides valuable results.

The most apparent quantity to be mapped is the locally averaged concentration C_i , or coarse grain density (Welander, 1955), of a marker fluid in Ω_i . Thus, for every Ω_i in Ω the initial concentration C_i is stored in a column $C^{(0)}$. Now, the concentration distribution $C^{(n_t \Delta t)}$ at $n_t \times \Delta t$ could be computed by $C^{(n_t \Delta t)} = \Phi_{\Delta t}^{n_t} C^{(0)}$, provided that the map $\Phi_{\Delta t}$ is

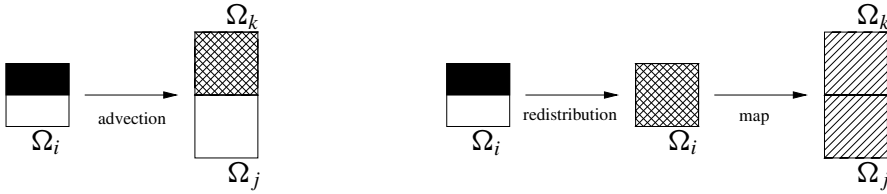


Fig. 2.5: The diffusive error made by the mapping method: suppose that the top half of domain Ω_i with concentration 1, would be advected to subdomain Ω_k and the bottom part, with concentration 0, in subdomain Ω_j as shown on the left. Using the mapping method, the concentration will be locally averaged before it is mapped to subdomains Ω_j and Ω_k as shown on the right.

the same for every consecutive Δt (repetitive mixing). [Spencer & Wiley \(1951\)](#) already suggested, in a similar approach for very simple transformations, to analyse mixing behaviour by studying the properties of Φ^n . Where Φ will generally be a sparse matrix, Φ^n will generally be dense, since fluid from an initial subdomain will finally be advected throughout the flow domain. This makes studying the properties of Φ^n both unattractive and even impossible for efficient three-dimensional exponential mixing flows. Therefore, instead of investigating Φ^n , e.g. $C^{(n)}$ could be investigated. $C^{(n)}$ is computed by the sequence for $i = 1$ to n :

$$C^{(i)} = \Phi \cdot C^{(i-1)}. \quad (2.7)$$

This procedure does not change the matrix Φ and is, therefore, much cheaper, both in number of operations as well as in the computer memory needed, than computing Φ^n . A disadvantage is, of course, the (artificial) diffusion introduced by subdomain-averaging, which occurs in every mapping step and can only be decreased by decreasing the number of mapping steps, thus increasing the time-span of the map. This essential disadvantage of a large number of subsequent mapping steps requires a balance between the length of the elementary time step Δt and the number of steps n to span the total mixing time $n\Delta t$.

An example of how the boundaries Γ_i deform for a time-periodic prototype flow like the lid-driven cavity as they are advected during a time step Δt of the flow is shown in figure 2.6. The figure shows the deformation of the subdomains due to fluid flow induced

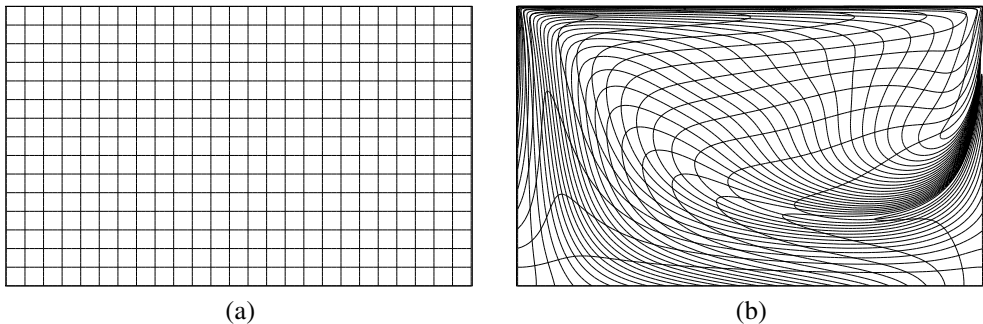


Fig. 2.6: Coarse mesh subdomain advection in a lid driven cavity flow. a) Initial subdomain distribution (25×15 grid) and b) deformed grid after a displacement of $D = 2$.

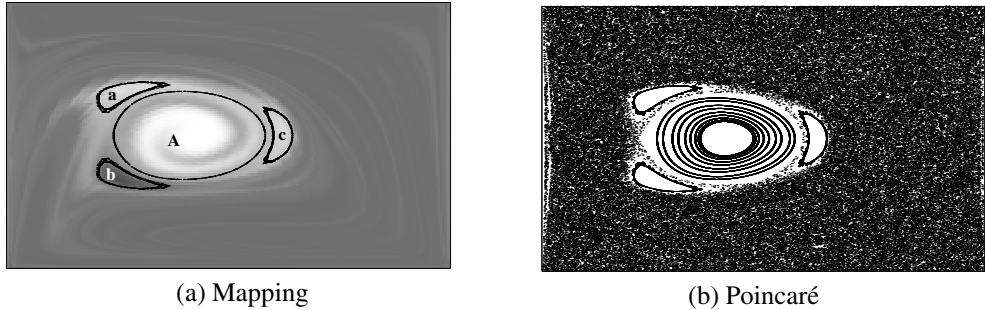


Fig. 2.7: a) Concentration distribution after 20 periods (alternatingly moving the top wall T and bottom wall B) with $D = 8$ and $n = 40$; initially the right half of the cavity was black, the left half white. The islands are marked by additional contours. b) Poincaré map to show the correspondence in the location of the island. The three third order islands are visible with both techniques.

by a displacement of the top wall of twice its length. Note that this figure serves only as an illustration. Actual analyses are computed with a two to five orders of magnitude finer grid (200×120 , 400×240 or 800×480 subdomains).

2.4.2 Comparison of mapping with traditional methods

To show the advantages of the mapping method it will be compared to the Poincaré method and the tracking method. In figure 2.7 results of the mapping method are compared to results of the Poincaré method for $D = 8$. The results of the mapping method were obtained by colouring the right half of the cavity black ($C = 1$) and mapping this concentration distribution for twenty periods. The size of the large central island is readily recognized. Also, the three smaller islands (a,b,c) around the first island (A) are found as well. In contrast to Poincaré sections, mapping allows for the determination of the order of the periodic points: island A is of order 1; islands a, b, and c are of order three and rotate counterclockwise (which can be deduced from the grey level of the islands). Notice that the structure (striations) in the concentration distribution is still distinguishable after 20 mapped periods, despite the diffusive character of this method. The influence of the grid-size on the diffusive error is shown in figure 2.8. It is clear that with increasing resolution the tracked pattern as shown in figure 2.3 is restored better. However, one should also keep in mind that the resolution need not be as high as possible, but that it should be chosen in accordance with the physical size of the flow domain and the phenomena one is interested in.

The mapping technique is, by its nature, less accurate than the adaptive contour tracking technique. This does not imply any serious limitations, as will be shown by comparing both methods for a limited number of periods (due to limitations of the contour tracking technique).

The mapping method is compared to the tracking method for three to five periods. The initial and final situations as obtained by the tracking method are shown in figure 2.3. To compare tracking and mapping, the coarse grain intensity of segregation is applied to both

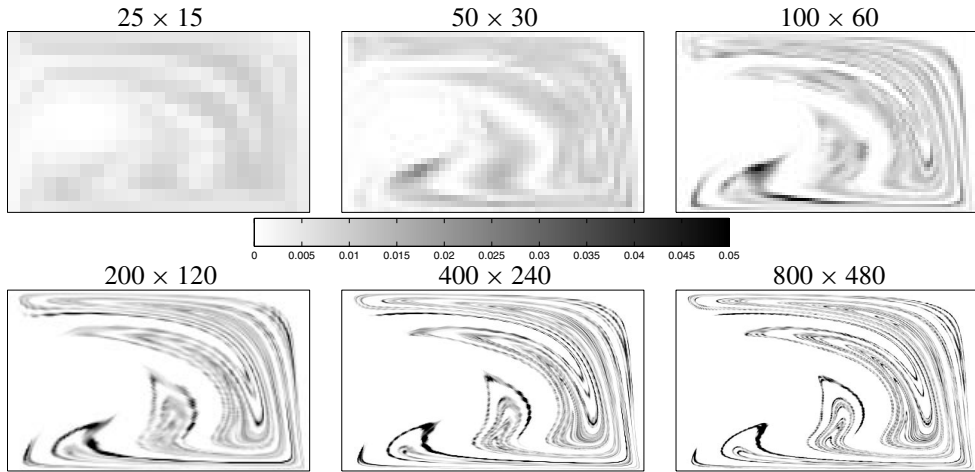


Fig. 2.8: Concentration distribution after 5 periods, obtained by mapping from 1-period distribution (computed using adaptive front tracking and discretized) with different resolutions.

techniques. The results of the tracking method are discretized on the same grid as the mapping method (see figure 2.9).

In case of the tracking method, the discrete intensity of segregation, I_d (see appendix A) is computed after five periods by discretizing the tracked boundary of the dyed area, as shown in figure 2.3, on the grid on which the corresponding mapping matrix was computed. For the mapping method, the contour of the dyed area was tracked for one period, discretized, and then mapped to five periods. As indicated in table 2.1 the accuracy is apparently only moderate, and worse for the larger domain sizes, which was to be expected given the artificially induced diffusion. Assuming that due to diffusion only the neighbouring subdomains are affected, one subdomain would affect eight neighbours (and vice versa). Since with the tracking method no neighbouring subdomains are affected, the discretization grid for the tracking method can be nine times larger than for mapping, or alternatively, mapping needs a nine times finer gridsize in order to obtain the same value for the intensity of segregation. If table 2.1 is more closely regarded, it is evident that the values for the intensity of segregation for the tracked grids at 100×60 and 200×120 are close to the values obtained by mapping on 300×180 and 600×360 grids, respectively. Their ratio equals 1.0 in both cases. A better comparison is shown in figure 2.10. The values for the intensity of segregation computed by mapping and tracking are plot as a function of the number of subdivisions along the x -axis. The ratio of the slopes of the fitted lines through the datapoints is 7.5. This indicates that in order to obtain the same values for the intensity of segregation using the mapping method, the resolution of the grid should be 2.7 times higher than for the tracking method. This value, however, will be different for a different type of flow.

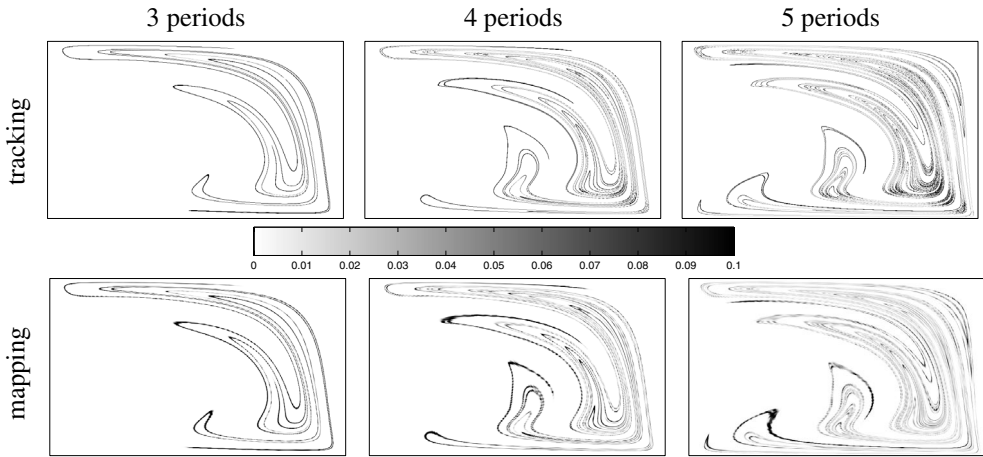


Fig. 2.9: Comparison of the discretized concentration distribution for the tracking method and the mapping method on a 800×480 grid (initial location of the blob is shown in Figure 2.3).

2.5 Long term mixing behaviour; optimization

The mapping method is a flexible tool for optimizing mixing, since it allows the incorporation of variations on an existing mixing protocol, without having to recompute the entire protocol adapted repeatedly. As an illustration, two parameters of the cavity flow are varied: the dimensionless displacement D and the number of wall movements n ; the product of which is proportional to energy input. Different protocols are compared by changing the order of consecutive mappings.

Five different protocols are investigated. In protocol A only the top wall moves, avoiding periodicity in the flow. In protocol B the top wall (T) and bottom wall (B) move alternately. Protocols C and D are variations on protocol B proposed by Ottino (1989), Franjone *et al.* (1989), Jana *et al.* (1994a), Aref & El Naschie (1995) to reduce the regularity of the protocol, thus decreasing the size of regions around elliptic points (symmetry breaking protocols). Protocol E is a variation of protocol B where a finite wall length is taken into account and the direction of the wall motion is changed.

In first instance, for all these protocols the concentration distribution is computed with only two mapping matrices: $\Phi_{D=2}$ and $\Phi_{D=4}$ (movement of the top wall only). Since the geometry is symmetric, the map for a movement of the bottom wall is the same as for the top wall, but rotated (x and y values multiplied by -1 in the coordinate system of figure 2.1). Wall movement in the opposite direction and movement of the opposite wall, can be computed by mirroring (multiplying the x and/or y -coordinate by -1 in the coordinate system of figure 2.3). This prevents that extra matrices need to be computed and stored. Results are shown in figures 2.11a and 2.11b; for all concentration distribution plots the energy input ($n \cdot D$) is constant.

Figure 2.11 clearly shows different mixing behaviour for the different protocols and different values for D and n . From figure 2.11a it could be suggested that simply increasing D at the cost of n is beneficial for the mixing performance. This is not the case, however,

Tab. 2.1: Intensity of segregation after five periods for the mapped and tracked method.

Grid size	tracked	mapped	ratio
25×15	$5.906 \cdot 10^{-3}$	$1.413 \cdot 10^{-3}$	4.18
50×30	$1.089 \cdot 10^{-2}$	$3.413 \cdot 10^{-3}$	3.19
100×60	$1.992 \cdot 10^{-2}$	$7.195 \cdot 10^{-3}$	2.77
200×120	$3.823 \cdot 10^{-2}$	$1.347 \cdot 10^{-2}$	2.84
300×180	$5.538 \cdot 10^{-2}$	$2.011 \cdot 10^{-2}$	2.75
400×240	$7.065 \cdot 10^{-2}$	$2.740 \cdot 10^{-2}$	2.58
600×360	$9.883 \cdot 10^{-2}$	$3.823 \cdot 10^{-2}$	2.59
800×480	$1.257 \cdot 10^{-1}$	$5.055 \cdot 10^{-2}$	2.49

since when the parameter D is increased further (figure 2.11b), all protocols become similar to protocol A (only the top wall moving, no periodicity) and the intensity of segregation increases. Apparently (and naturally), there is an optimum value for D and n , since both large D as well as large n yield laminar mixing.

The mixing properties for the five different protocols are now investigated in more detail, with D varied between 0.25 and 64.0, in steps of 0.25, and n between 1 and 64 using just five maps for different values of D . The first four maps (for $D = 0.25$, $D = 0.5$, $D = 1.0$ and $D = 2.0$) were computed while integrating to $D = 4.0$, thus computing the five maps in a single run. This run was computed using 50 personal computers in parallel during 16 hours. The mapping matrices were then extracted from the tracked grids (see figures 2.4 and 2.6) which took 2 hours on the same set of computers.

The resulting maps are applied to the concentration column C to determine the concentration distribution. If e.g. the concentration distribution $C^{(5.25)}$ for $D = 5.25$ is required, it is computed by:

$$C^{(5.25)} = \Phi_4(\Phi_1(\Phi_{0.25}C^{(0)})). \quad (2.8)$$

Computing the concentration distribution by matrix column multiplication requires less than a second on a single machine for each mapping operation.

A two-dimensional, stationary Stokes flow will not be chaotic. Therefore mixing will be linear, and will only depend on the amount of energy used. The efficiency plot for protocol A (see figure 2.12) shows this: the lines where intensity of segregation is constant have the same hyperbolic shape as the lines where energy input is constant. This figure also shows the influence of consecutive mappings: the lines of constant intensity of segregation are jagged with an increasing amplitude for an increasing number of mapping operations, which is explained by the fact that e.g. a D of 8.0 is reached with two mappings ($\Phi_4(\Phi_4C^{(0)})$), whereas a D of 7.75 is computed with five mappings ($\Phi_4(\Phi_2(\Phi_1(\Phi_{0.5}(\Phi_{0.25}C^{(0)}))))$). Since every mapping step introduces diffusion into the system, the calculated intensity of segregation decreases if more mappings are needed.

Figure 2.13 shows plots of the intensity of segregation (equation A.2, appendix A) as a function of D and n for protocols B through E. Black indicates a bad mixture (i.e. $I_d = 1$), white indicates a good mixture (i.e. $I_d = 0$). All plots clearly show values for D where

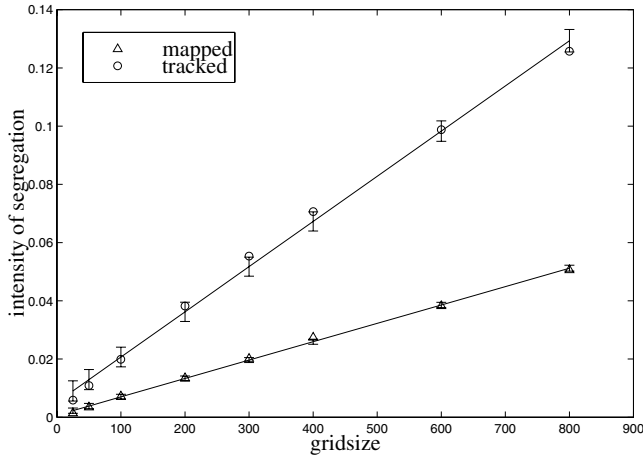


Fig. 2.10: Intensity of segregation after five periods for the mapped and the tracked method as a function of the gridsize.

the intensity of segregation of the mixture only slowly changes with changing n (the grey streaks), while for other values of D just a slight change in its value results in a stepwise improved mixture, often with less energy input (the white areas). The plots also indicate where a slight variation in process parameters can have a large effect on the resulting quality of the mixture. The spacing of the streaks in the direction of D is nearly equidistant. This is explained by the presence of elliptic periodic points. Some of the elliptic points that occur for a certain value of D , will also occur for multiples of D . If the region of influence (island) of such an elliptic periodic point is large, the intensity of segregation will be large.

The mapping method is the only method known so far that can straightforwardly be used to show the dependence of mixing quality on process parameters. Computation of the efficiency plots as shown in figures 2.12 and 2.13 requires approximately 150.000 mappings and takes about 3 hours on a personal computer.

The different protocols can also be compared mutually and the more sophisticated protocols implement that symmetry breaking (like protocols C and D) yield more efficient mixing. Protocol B in particular shows the worst overall mixing efficiency of all periodic flows: a relatively high value for D (larger than 15) is needed in order to reach a good mixture quality. Remarkable is that the horizontal ‘spikes’ in the diagrams that indicate bad mixing are located at the same values for D and that only their width and length are influenced by the protocol.

For the scale of segregation (equation A.10, appendix A) similar diagrams can be constructed (figure 2.14). These plots appear similar to the plots of I_d as a function of n and D . However, there are some noticeable differences. From the wider (in the direction of the D axis) and longer (in the direction of the n axis) dark streaks in this figure it follows that the periodicity in the concentration distribution of the mixtures exists for a longer time span (the number of wall movements) and is less sensitive to the displacement D . This also indicates that the mapping method is able to preserve the structure (striations) of the mixture.

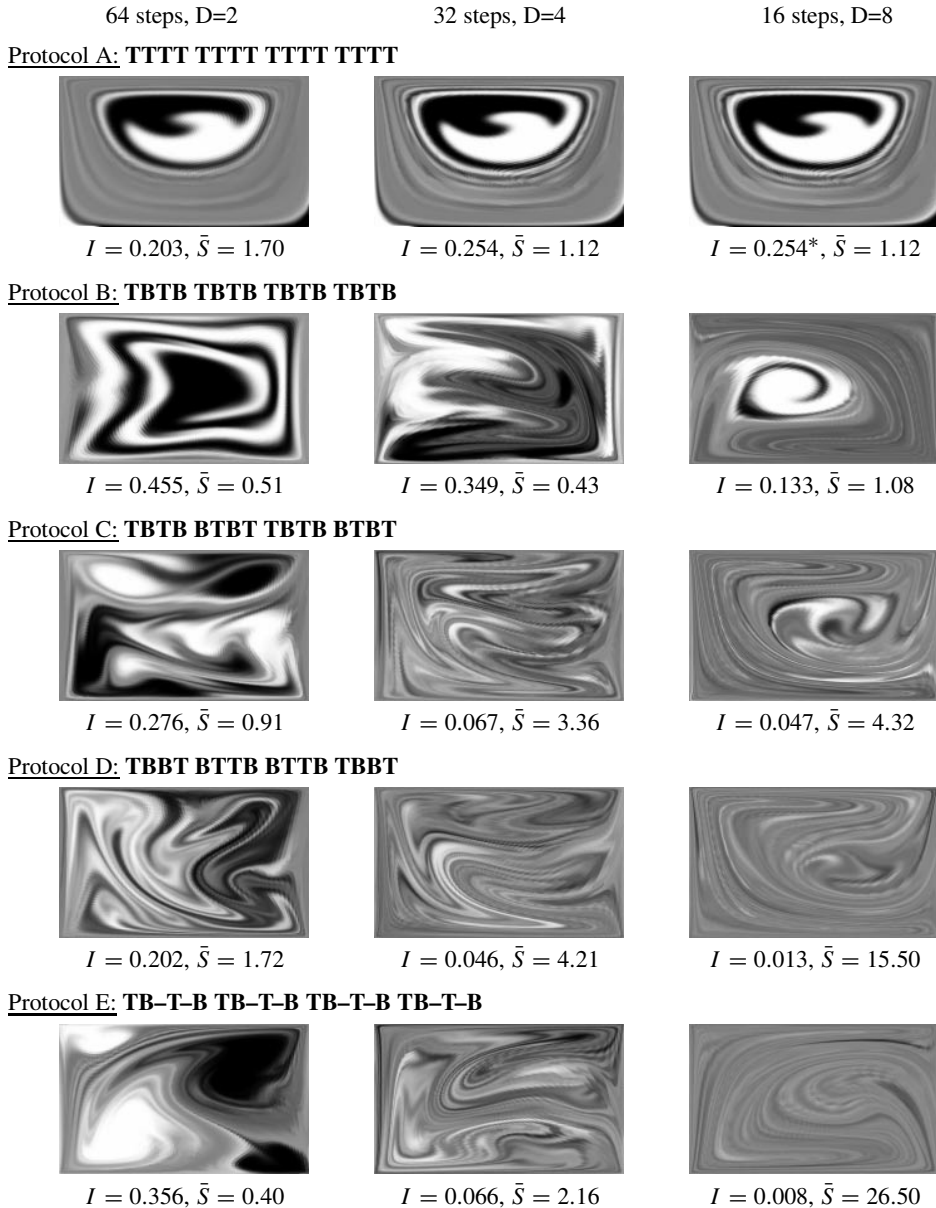


Fig. 2.11: (a) Results of dye advection using different protocols with the same energy input. All computations were done using pre-computed mappings for $D = 2$ and $D = 4$. Initially dyed fluid completely fills the right half of the cavity. The computed intensity of segregation is stated under each image. *) As for $D = 4$, the mappings with $D = 8$, $D = 16$, $D = 32$ and $D = 64$ were performed as a number of consecutive mappings with $D = 4$. ($\bar{S} = S \cdot 10^4$).

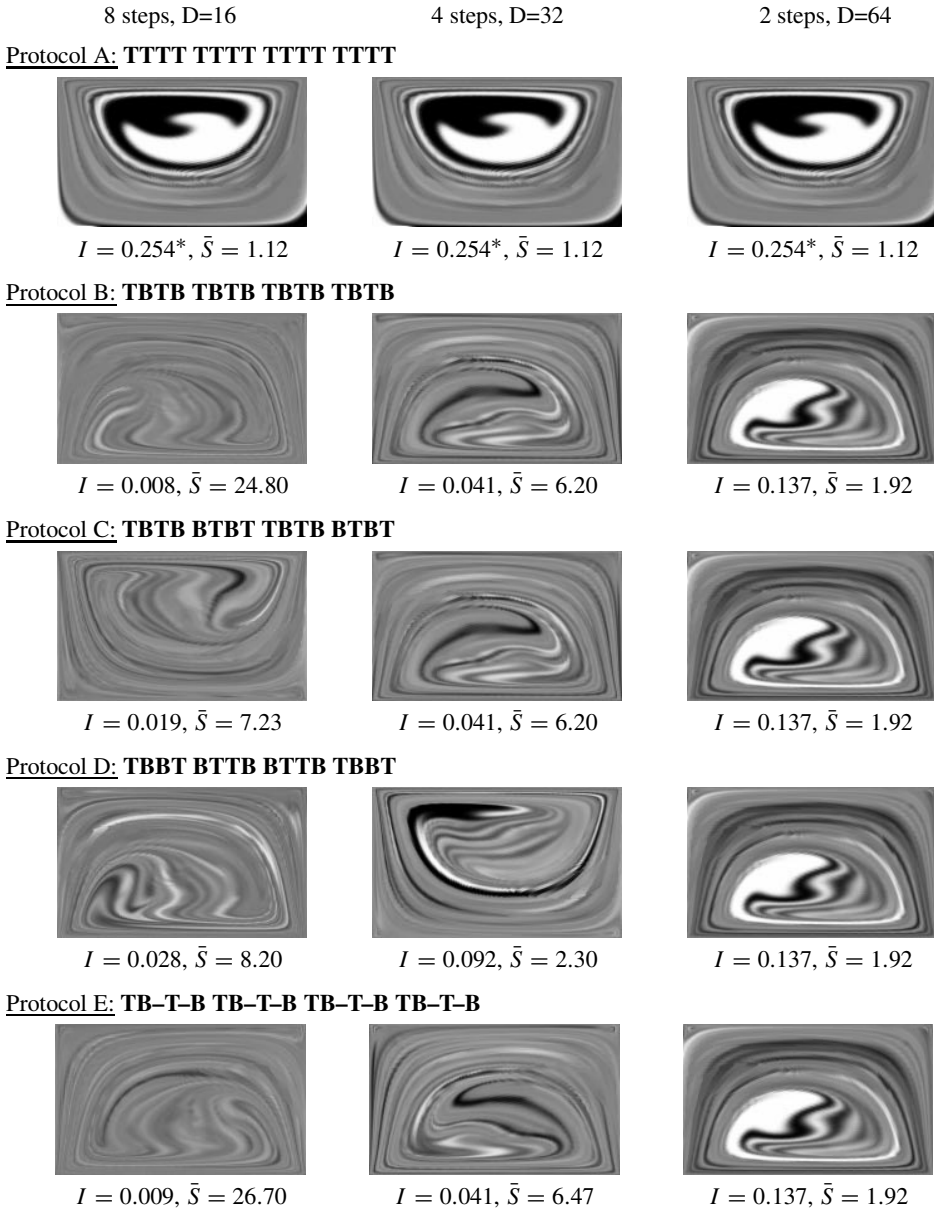


Fig. 2.11: (b) Figure 2.11a continued.

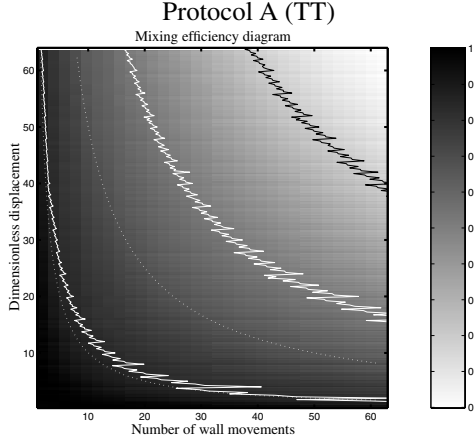


Fig. 2.12: Intensity of segregation I_d as a function of number of wall movements n and dimensionless displacement D . Protocol A shows the error due to numerical diffusion of the mapping method. The only independent parameter is the product $n \cdot D$ (energy). The iso-energy lines (\cdots) should therefore have the same hyperbolic shape as the iso-intensity of segregation lines ($-$).

2.6 Mapping of morphology

The accuracy of the mapping method is determined by the resolution of the spatial discretization of the mapping grid. However, morphology development mostly takes place on a finer level. In order to incorporate morphology into the mapping method, a quantity needs to be derived that describes properties of the morphology and can also be mapped. The area tensor is such a quantity (Wetzel & Tucker (1997), Wetzel & Tucker (1999a), Wetzel & Tucker (1999b), Galaktionov *et al.* (2000a)). The area tensor is defined as:

$$\mathbf{A} = \frac{1}{V} \int_{\Gamma} \mathbf{n} \mathbf{n} d\Gamma \quad (2.9)$$

with \mathbf{n} a unit normal vector on the interface between two components Γ . The components of \mathbf{A} have units of interfacial area per volume in three dimensions and units of interfacial length per area in two dimensions. The trace of the area tensor ($\text{tr}\mathbf{A}$) is equal to the total interfacial area in the averaging volume, the eigenvalues and eigenvectors are measures for the orientation and type of microstructure. Some typical examples, further details on the area tensor and its implementation are given in appendices C and D. The area tensor is not just mapped, but also transformed (taking into account the deformation of a subdomain during one mapping step).

In a simple shear flow, the interfacial area will increase linearly in time. Therefore, also the trace of the area tensor will increase linearly. For chaotic flows, the interfacial areas in some parts of the domain increase exponentially in time, therefore, also the trace of the area tensor increases exponentially. It is beyond the scope of this thesis to give a full treatment and analysis of the area tensor, and therefore only an example is given to

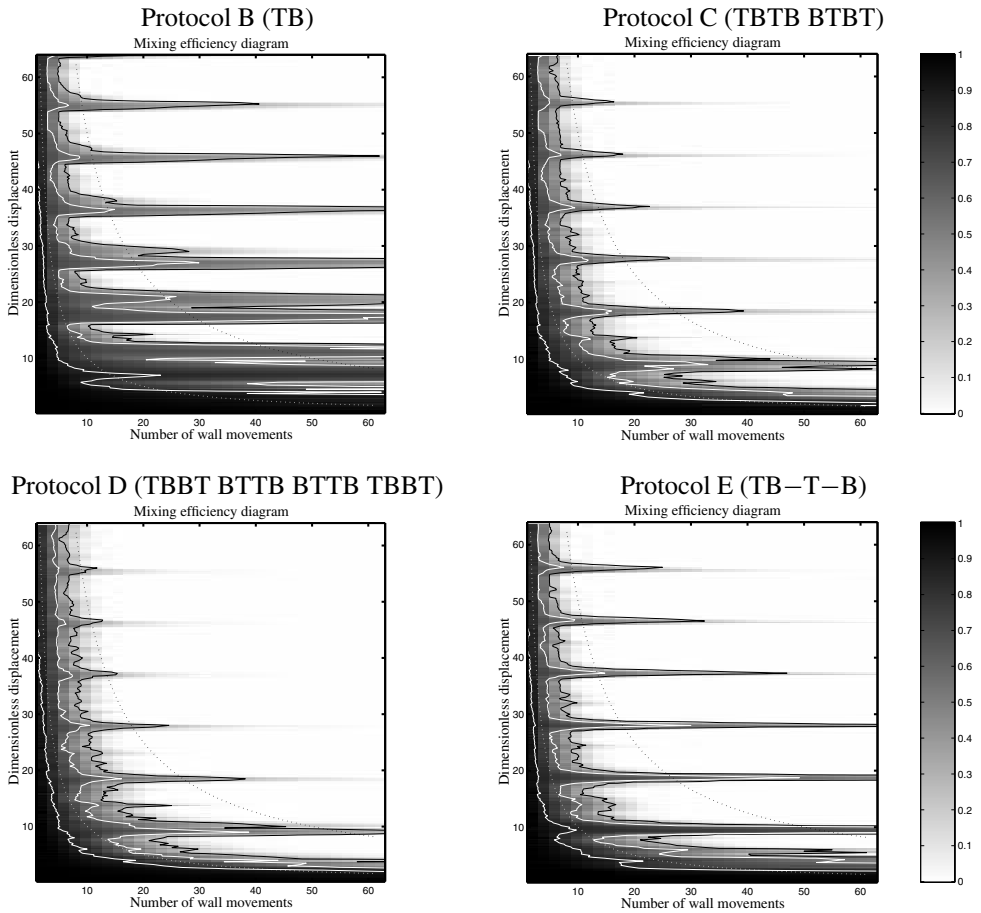


Fig. 2.13: Intensity of segregation plots for four different protocols. The dotted lines ($\cdot \cdot \cdot$) indicate lines of constant energy, the drawn lines ($—$) indicate lines of constant intensity of segregation.

demonstrate the strength of the method. Figure 2.15 shows the results of mapping the area tensor on a domain of 200×120 subdomains comparing them to maps of concentration.

The figure clearly shows that information about interface is clearly preserved when the concentration distribution has almost evened out. Also, the self similar nature of the plots of $\text{tr}A$ is shown in this figure. The plot in figure 2.15b closely resembles those of figure 2.15d and f. The major difference is in the greyscale of the figures. It clearly indicates that the growth of interfacial area is exponential with the number of periods.

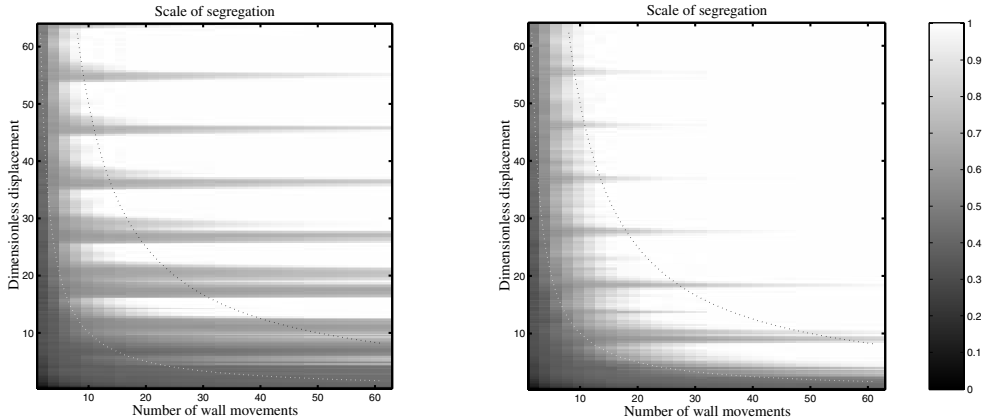


Fig. 2.14: Plot of the scale of segregation as function of D and n for protocol B (left) and protocol D (right).

2.7 Conclusions and discussion

The mapping method is an efficient method to analyse mixing protocols and geometries. Most computation time is consumed by tracking the boundaries of the subdomains and is mainly determined by the coarseness of the grid chosen, the accuracy of the description of the boundaries of the subdomains required and the time for which these boundaries have to be tracked. However, once these mapping matrices are determined, analysis of arbitrary mixing protocols that can be constructed from these matrices can be computed within seconds.

The efficiency of the mapping method lies in the feature that parameter variations can be made and investigated easily. It thus leads to a better understanding of the mixing properties of a flow and the influence of variation of its mixing parameters. Most of the results of other methods (Poincaré sections, manifold analysis, periodic point location and classification) can also be obtained using the mapping method. The decrease in accuracy caused by diffusive errors in the mapping method is clearly compensated for by its flexibility: on one hand the mapping method keeps track of information concerning the actual distribution of dyed fluid, in contrast to e.g. the Poincaré method in which points have no physical size. On the other hand, in contrast to application of boundary tracking methods the investigation of higher numbers of periods (> 10) and different initial dye shapes and position is possible by applying the mapping method. Further, as clearly demonstrated, once a set of distribution matrices is computed, they can be used to compute a range of different protocols with different parameters, allowing for an optimization of the mixing protocol. Finally, once a mixing protocol is chosen, the mapping method can be used to compute efficiency plots that indicate for which set of process parameters mixing is good and insensitive to disturbances of those process parameters.

Most results presented in this chapter refer to mapping concentration. However, other measures can also be mapped. As an example, results for mapping the area tensor, representing interfacial area, are also given. Another example of a quantity that can be mapped is residence time. This is only useful in mixing flows with open domains and thus will be dealt with in chapters 4 and 5.

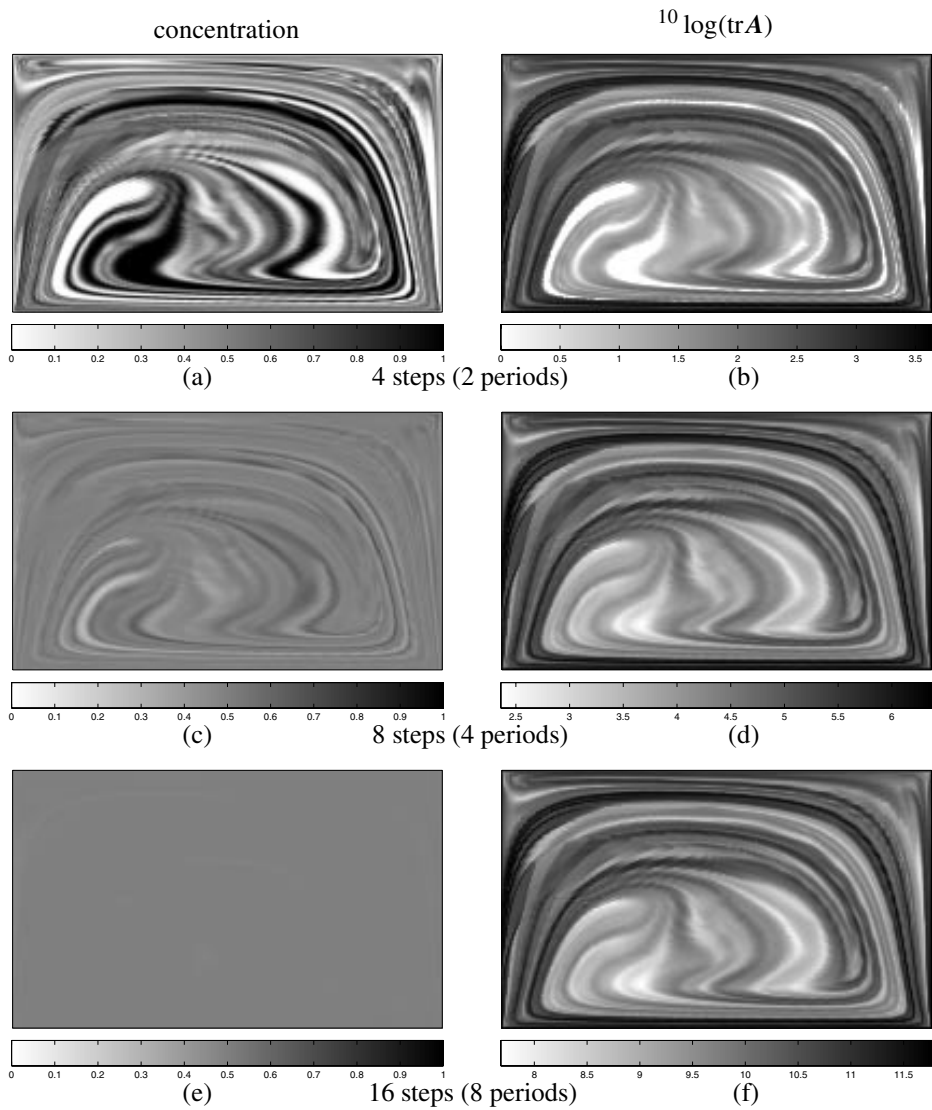


Fig. 2.15: Evolution of concentration (left) and trace of the area tensor (right) distributions in the flow described by protocol TB with dimensionless displacement $D = 16$. Marker fluid initially fills the left half of the cavity. The results are shown after 2, 4, and 8 periods of the flow on a 200×120 grid.

Chapter 3

*Three-dimensional time-periodic prototype flows**

3.1 Introduction

Mixing analysis of three-dimensional flows introduces a number of complications. The Poincaré method e.g. would need to be adapted in a way to show the distribution of points in slices of the domain considered. Also, once done, as indicated in chapter 2, the Poincaré method does not give information on the actual distribution of fluid in a layer and will always give an asymptotical situation. On the other hand, volume tracking is more complicated compared to the two-dimensional case, since points to be tracked are multiply-connected instead of singly-connected, as was the case in two-dimensional boundary tracking. This poses problems for the description of the volume surface, but even more so for the adaptive refinement of the surface. Front capturing techniques or volume of fluids methods may be more readily available or easier to implement, however, like boundary tracking they need to be repeated for every change in mixing protocol.

Therefore, the mapping method introduced in chapter 2 will be extended to three dimensions. The problems of volume description and refinement, consequently, need to be tackled (see appendix B). The three-dimensional mapping approach will be tested on a second prototype mixing flow which is closely related to the two-dimensional cavity flow discussed in chapter 2: a cubic domain (box) with four stationary walls and two oppositely placed sliding walls (see figure 3.1). It will be shown that by adapting the intensity of segregation to three dimensions (see appendix A), the mapping method can also be used to compare the efficiency of protocols in 3D.

3.2 Computational method and boundary conditions

In order to investigate three-dimensional mapping, the prototype mixing flow in two dimensions, the lid-driven cavity, is extended to three dimensions (Galaktionov *et al.* (1997), Anderson *et al.* (1999)). The domain is defined as $-1 \leq x, y, z \leq 1$ in dimensionless coordinates. The resulting lid-driven cubic cavity has two opposing walls (front, $y = -1$, and back, $y = 1$) that can move freely in their xz -plane. All other walls are fixed. Figure 3.1 shows the possible movements of the front and back wall as well as the notations used to define them and the same notation is used to define the corresponding mappings. Motion of the front and back wall are indicated by ‘ F ’ and ‘ B ’, respectively; the subscripts l, r, u and d

* This chapter is largely based on: *A mapping approach for 3D distributive mixing analysis*, O.S. GALAKTIONOV, P.D. ANDERSON, P.G.M. KRUIJT, G.W.M. PETERS, and H.E.H. MEIJER, accepted by *Computers and Fluids*, 2000.

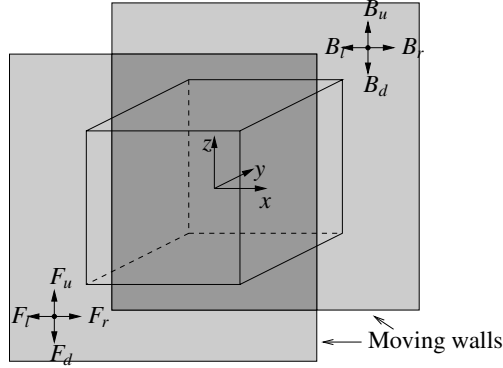


Fig. 3.1: Prototype mixing flow in a cubic cavity with moving front and back walls.

indicate the direction of the movement (to the left and right, up or down, respectively). This relatively simple geometry allows for accurate numerical solutions and forms a convenient model for testing the techniques designed to study three-dimensional laminar time-periodic distributive mixing in general.

The flow in the cavity is described by the Stokes equations:

$$\begin{cases} -\eta\Delta\mathbf{u} + \nabla p = 0 \\ \nabla \cdot \mathbf{u} = 0 \end{cases} \quad (3.1)$$

where $\mathbf{u} = (u, v, w)^T$ is the velocity, p the pressure and η the dynamic viscosity of the fluid. For all walls homogeneous Dirichlet boundary conditions are imposed, except for the front wall where the condition $u = 1, v = 0, w = 0$ is prescribed (thus the velocity field for F_r is obtained). The numerical solution of (3.1) is performed by a projection method that decouples the pressure p and velocity \mathbf{u} (Timmermans *et al.*, 1996). A spectral element approximation (Maday & Patera (1989), Anderson (1999)) is used for the spatial discretization and gives an accurate approximation of the velocity field. The cavity is subdivided into $15 \times 15 \times 15$ sixth order spectral elements, leading to totally 753,571 nodal points and a system with 2,868,477 degrees of freedom. The resulting system of equations is solved using a conjugate gradient solver with a finite element preconditioner (Anderson, 1999).

Since Stokes flow is considered and the flow domain is symmetric, the velocity field needs to be computed for only one type of wall motion (in this case F_r is chosen). The velocity fields for all other wall motions indicated in figure 3.1 can be obtained by simple coordinate transformations.

3.3 Three-dimensional mapping approach

Although the flow in a cubic cavity is well-defined, due to singularities in the boundary conditions on the edges of the moving walls high gradients in the velocity field exist locally. In order to reduce the computational cost of tracking, not the entire domain is divided into subdomains to be tracked for mapping. Instead this domain was reduced by considering only

Tab. 3.1: Size and sparsity of the mapping matrices computed for two different spatial resolutions and different dimensional displacements.

resolution displacement	50 × 50 × 50			100 × 100 × 100
	$D = 1$	$D = 2$	$D = 4$	$D = 2$
# subdomains	125,000 + 1			1,000,000 + 1
# matrix elements	$\approx 1.56 \times 10^{10}$			$\approx 10^{12}$
# non-zero elements	1,186,037	1,293,581	1,587,199	10,468,501
matrix density	0.0076%	0.0083%	0.0102%	0.0011%

the inner part $-0.95 \leq x, y, z \leq 0.95$, of the cavity and was subdivided into a regular array of cubic subdomains. The remaining part of the cavity is accounted for as one single subdomain.

Mapping matrices are computed on two different spatial resolutions: $50 \times 50 \times 50$ and $100 \times 100 \times 100$. As mapping in essence comes down to tracking the boundary of a large number of subdomains, the computation of the individual entries in the mapping matrices was performed in parallel using PVM based algorithms (Geist *et al.*, 1994). Since the number of nodes needed to describe all deformed boundaries is too large to store into computer memory, the deformation of a particular subdomain is computed entirely by one slave process. This slave process also determines the volumes of intersections with the initial subdomains and returns the non-zero elements of the mapping matrix to the master program that assembles the mapping matrix. This individual tracking of boxes increases the processor-time for the total computation since almost all lines are tracked twice. However, the approach allows the computation of the mapping matrix with good accuracy, without running into memory problems.

As Stokes flow is assumed, the deformation of the subdomain boundaries is completely defined by the dimensionless displacement of the wall D , defined here as the wall displacement divided by half the cavity edge length. For the low spatial resolution ($50 \times 50 \times 50$) the mapping matrices were computed for three different wall displacements $D = 1$, $D = 2$ and $D = 4$; for the finer resolution ($100 \times 100 \times 100$) only the matrix for $D = 2$ was computed due to the higher computational costs. In all cases only the boundaries of the subdomains in the lower half ($z < 0$) of the cavity were tracked, and symmetry of the flow around $z = 0$ plane was used to obtain the deformation of the subdomains from the upper part.

Only the mapping matrices corresponding to the movement F_r are computed. Mappings for all other motions are obtained by using the symmetry of the velocity field and flow domain. For example the mapping F_l can be presented as $S_x F_l S_x$, where S_x is the symmetry operator $S_x(x, y, z) = (-x, y, z)$. Similar transformations yield all other types of wall motion considered here.

The data on the computed mapping matrices are summarized in table 3.1 from which it is obvious that the mapping matrices are very sparse. Since the full matrix for the higher resolution grid would already contain 10^{12} elements, of which less than 0.0011% are non-zero, it is clear that a compact storage algorithm has to be used.

Although computation of the mapping matrix in three dimensions is computationally expensive due to tracking of a large amount of nodal points needed for an accurate boundary description of the deformed subdomains, it has to be computed only once. The matrix-vector

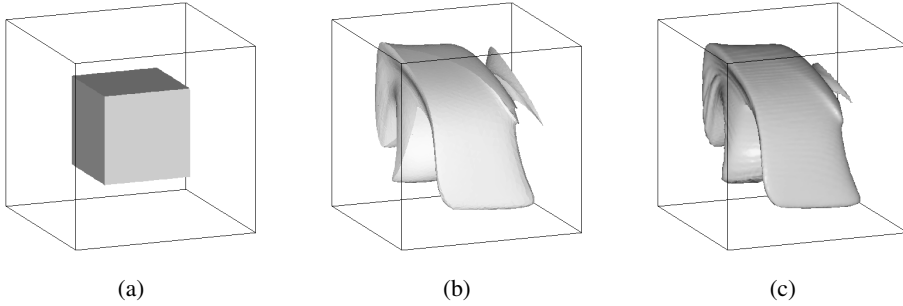


Fig. 3.2: Comparison of front tracking and mapping results after one cycle of the $F_r B_u F_l B_d$ protocol with dimensionless displacement $D = 4$: a) initial test volume; b) results of adaptive front tracking; c) interface shape recovered from the mapping results ($100 \times 100 \times 100$ resolution).

multiplications used to determine concentration distributions, on the other hand, are computed within a second computing time, and need to be repeated many times in order to evaluate the mixing efficiency in time and for various protocols.

3.4 Verification

Validation of the mapping technique in three dimensions is done by comparing the results of the mapping technique with those of front-tracking. Due to limitations of the front tracking technique, the volume is tracked for a limited number of steps.

A cubic-shaped volume of marker fluid is positioned in the centre of the cavity (see figure 3.2a). Inside this volume the concentration is set to 1, outside to 0.

This pattern was advected for one period in a four-step protocol described by $F_r B_u F_l B_d$ and $D = 4$ for every step. The result of adaptive front tracking is presented in figure 3.2b. The result from the mapping technique was obtained on the higher resolution grid with a total of eight mapping operations (since only a mapping matrix for $D = 2$ is available). The resulting concentration distribution is regarded as *voxel* data, i.e. the local concentration value was attributed to a cube with the size of a subdomain. The boundary of the marker fluid in figure 3.2c is visualized by plotting the iso-concentration surface at a level of $c = 0.5$. This explains why the tip of fluid in the upper right corner of figure 3.2b is larger than in figure 3.2c. The layer of fluid is so thin that less than 50% of the domain is filled.

The surface shape recovered from the mapping results is in good agreement with the results of adaptive front tracking. Minor differences, as e.g. loss of sharpness of the edges can be observed. It should be noted that the reconstruction of the interface shape from the concentration distribution (obtained via mapping) is directly related to front capturing techniques. Interface reconstruction for stronger deformations is an involving problem (Qu & Li (1996), Rudman (1997)).

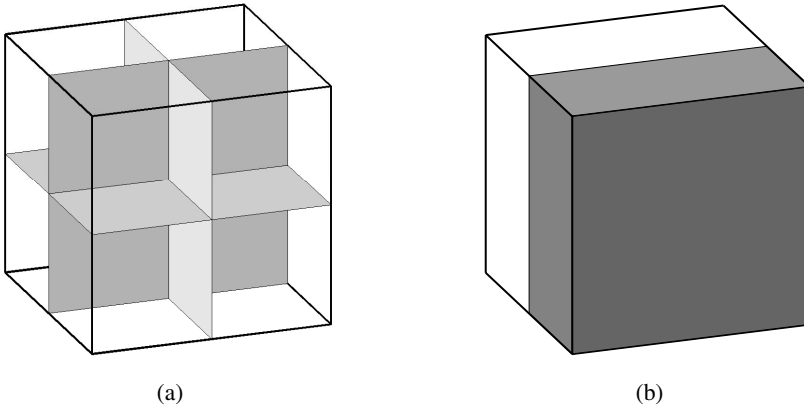


Fig. 3.3: a) Cross-sections on which concentration distribution is displayed; b) initial concentration distribution.

3.5 Results

The mixing patterns are presented by displaying the concentration distribution on selected planes in the cavity as shown in figure 3.3a. The initial concentration distribution is shown in figure 3.3b, and can be characterized as:

$$\begin{cases} c = 1 & \text{for } y \leq 0 \\ c = 0 & \text{for } y > 0 \end{cases} \quad (3.2)$$

3.5.1 Influence of spatial discretization

The influence of spatial resolution on concentration distribution is shown in figure 3.4. In both cases an eight step protocol ($F_r B_l F_l B_r F_d B_u F_u B_d$ with $D = 8$) is applied to the initial distribution shown in figure 3.3b. For the lower spatial resolution this resulted in 16 mapping operations with $D = 4$, for the higher resolution 32 mapping operations with $D = 2$ were used since only one mapping matrix (for $D = 2$) was available. Although twice more mapping operations were needed for the high resolution results, the image shows more detail. Since the region near the cavity walls is taken into account as one large subdomain, these subdomains show up as having a uniform grey colour in the plots since all contributions to this subdomain are averaged too. As this subdomain also contributes to other subdomains in the cavity, the subdomains that get a large contribution from the outer subdomain tend to get an average concentration rapidly. This effect is apparent in the left bottom part of the cavity.

The quality of the mixture is characterized by the intensity of segregation I . The value of I is influenced by two mechanisms: the actual mixing process (striation thickness) and errors due to averaging over subdomains (see figure 2.5). Finer spatial resolutions reduce the numerical errors (see figure 3.4). Notice that if the subdomain size decreases due to the higher resolution, the value of I increases since the averaging volume decreases and less diffusion occurs. Therefore, the magnitude of I by itself is not a reliable quantitative value to describe

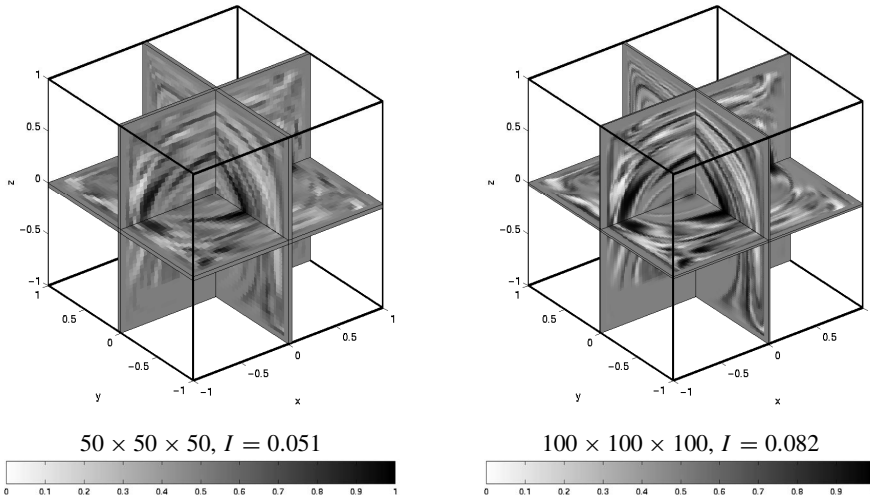


Fig. 3.4: Dependence of the computed mixing pattern on spatial resolution after eight steps of the protocol $F_r B_l F_l B_r F_d B_u F_u B_d$ with $D = 8$. For low resolution (left picture) 16 mappings with $D = 4$ were performed; for high resolution (right) – 32 mappings with $D = 2$.

the quality of the mixture (see also table 2.1). It is, however, useful to qualitatively compare mixtures obtained by different protocols on the same spatial discretization.

Intensity of segregation as a function of the number of steps for three different mixing protocols and for two different spatial resolutions is shown in figure 3.5. The figure clearly shows that mapping with different resolutions produces different values of I , as the numerical diffusion is stronger for the mappings with the lower spatial resolution as averaging is performed on larger volumes. More important, however, is that the results obtained on both discretizations show the same trend and lead to the same conclusions concerning the relative efficiency of different mixing protocols. For better comparison, the intensity of segregation for the results computed using high resolution mappings were also evaluated using the low resolution grid, thus reducing the effect averaging on smaller volumes has on I . Due to extra averaging (in groups of $2 \times 2 \times 2$ neighbouring subdomains), the resulting intensity of segregation (indicated by dashed lines) is lowered. Because this extra averaging is only performed once (after the last mapping) instead of after every mapping operation, the result is better than for the low resolution mapping.

Another result apparent in figure 3.5 is that the computed intensity of segregation reaches a certain minimal level (observed here for the 8-step protocol) and then oscillates around that level. These oscillations may result from concentration fluctuations caused by errors in the values of the mapping matrix coefficients and impose the limit to which mapping simulations are useful. For a finer resolution a lower level of I can be achieved. Therefore, for all subsequent analyses the resolution $100 \times 100 \times 100$ is used.

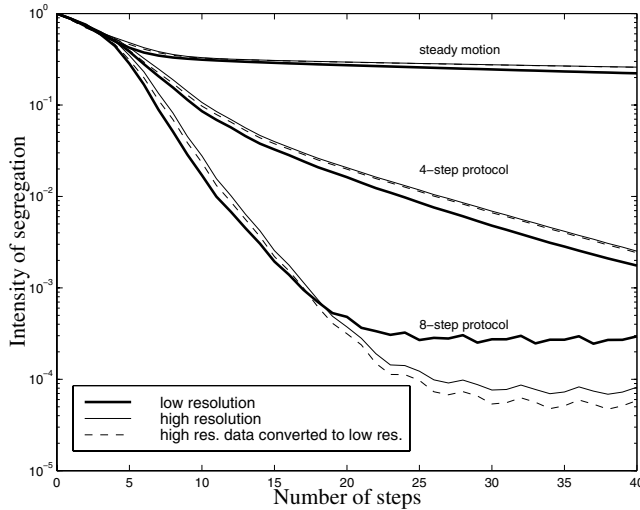


Fig. 3.5: Intensity of segregation for different mixing protocols with $D = 8$. The upper group of lines correspond to constant movement of the front wall to the right ($F_r F_r \dots$), 4-step protocol is $F_r B_u F_l B_d$, 8-step protocol is $F_r B_l F_l B_r F_d B_u F_u B_d$. Dashed lines indicate results computed using high resolution mapping but with intensity of segregation estimated on the low resolution grid.

3.5.2 Comparison of mixing protocols

Combining the mapping technique with the use of a quantitative criterion (here the intensity of segregation I) gives a possibility to compare the mixing efficiency of different protocols. For protocols with the same energy input (in this case proportional to the sum of the wall displacements), the rate of the decrease of the intensity of segregation with the number of steps serves as a measure of the mixing efficiency. In figure 3.5 the evolution of the intensity of segregation is compared for three different protocols. The steady motion of a single wall does not produce efficient mixing, as spreading of material in this case is linear in time (no periodicity and hence no chaos). Therefore, the decrease in I is slowest in this case (see figure 3.5). The two time-periodic protocols, shown in the same plot demonstrate a better efficiency.

Figure 3.6 shows cross-sections (as defined in figure 3.3a) through the mixing patterns obtained by different time-periodic protocols with the same dimensionless displacement ($D = 8$). In all cases, eight steps of the protocol are performed ($n = 8$), thus the energy input is the same for all protocols. The two-step protocol $F_r B_d$ (figure 3.6a), in which the walls move in just one direction, is one of the simplest, three-dimensional mixing protocols in the cavity under consideration.

In the following analysis, protocols are restricted such that the total displacement of the individual front and back wall are zero after one period. These protocols are of interest because of their easier experimental feasibility: moving walls can be made of rigid transparent plates instead of closed belts, providing better optical access from different viewpoints. One of the simplest protocols adhering to this extra condition is the four-step protocol $F_r B_u F_l B_d$,

shown in figure 3.6b; each moving wall slides only along one axis, but the direction of its motion is altered every step. This protocol, however, is less efficient than the two-step protocol $F_r B_d$ (see figure 3.6a, $I = 0.098$). After eight steps the intensity of segregation is still almost twice as large ($I = 0.189$). Note that the intensity of segregation is computed over the entire flow domain, not only at the cross-sections shown in the pictures.

To improve the mixing efficiency, symmetry breaking techniques can be used (Franjione *et al.*, 1989). The protocol $F_r B_u F_l B_d F_d B_l F_u B_r$ (figure 3.6c) is such a symmetry breaking protocol and is obtained by first performing one cycle of the four-step protocol and then repeating a similar sequence of wall motions rotated by 90° . This indeed improves the mixing performance a bit (I has somewhat decreased — see figure 3.6c, $I = 0.169$), but still does not bring it to the level of the simple two-step protocol. Using the experience obtained from studying two-dimensional mixing in a rectangular cavity, more efficient protocols can be constructed. In the eight-step protocol $F_r B_l F_l B_r F_d B_u F_u B_d$ (figure 3.6d) the first four steps are similar to protocol E for the two-dimensional cavity (see section 2.5), which was found to be efficient in that case. Next, a similar sequence of wall motions is performed in z direction. The resulting protocol is slightly more efficient than the two-step protocol: the intensity of segregation has decreased (see figure 3.6d, $I = 0.082$).

The mapping technique is an efficient tool to optimize the parameters of the chosen protocol. The mixing efficiency of the protocols in the three-dimensional system under study strongly depends on the dimensionless displacement. If the energy input for a particular mixing protocol is fixed (i.e. $n \times D$ is constant), an optimal dimensionless displacement will produce a more uniform mixture. To illustrate this, figure 3.7 shows the results of a mixture obtained by the protocol $F_r B_l F_l B_r F_d B_u F_u B_d$ for four different cases with $D = 2, 4, 8, 16$ and number of steps $n = 64, 32, 16, 8$, respectively. In addition to the intensity of segregation, the minimal and maximal concentration in the flow domain are given. A non-linear greyscale is used to increase the image contrast and to reveal the striation patterns.

As expected from the two-dimensional case, the flow with the $D = 2$ does not produce a good mixture: the intensity of segregation is still rather high after 64 steps. Large non-mixed zones are clearly visible and their presence is also indicated by the extreme minimal and maximal values of concentration. When the same mixing protocol is used with a two times larger displacement ($D = 4$), the intensity of segregation decreases and the range of concentration values narrows. The quality of the mixture further increases for $D = 8$: the intensity of segregation is over 58 times smaller than in the case of $D = 2$. For higher displacements the mixture quality decreases again (cf. section 2.5). It is noteworthy that even for the well mixed patterns the lamellar structure is still clearly visible.

Figure 3.8 shows the evolution of the intensity of segregation for the flows presented in figure 3.7 (where only final results are shown). The intensity of segregation is plotted versus total wall displacement, which serves as a measure of the work done on mixing. It is clearly seen that an optimum can be found and the intensity of segregation decreases fastest for the flow with dimensionless displacement $D = 8$. This tendency already becomes clear after one complete cycle of this protocol is performed (total wall displacement equals 64).

Each of the mapping simulations, results of which are presented in figure 3.7, took approximately 4 minutes (on average about 3 seconds per mapping operation). Thus, the mapping approach offers a computationally inexpensive tool for mixing simulations, once the mapping matrix is constructed.

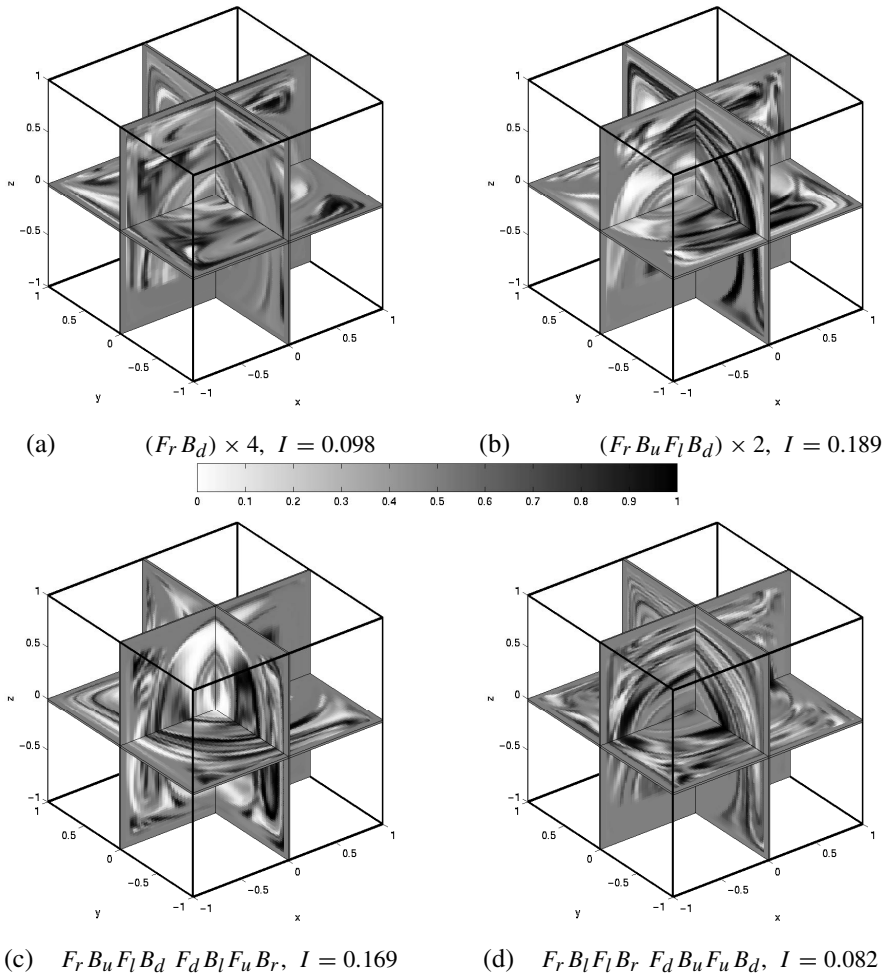


Fig. 3.6: Comparison of different protocols with equal energy input. In all cases eight steps (wall movements) with dimensionless displacement $D = 8$ were performed. The protocol and resulting discrete intensity of segregation I are stated under each image.

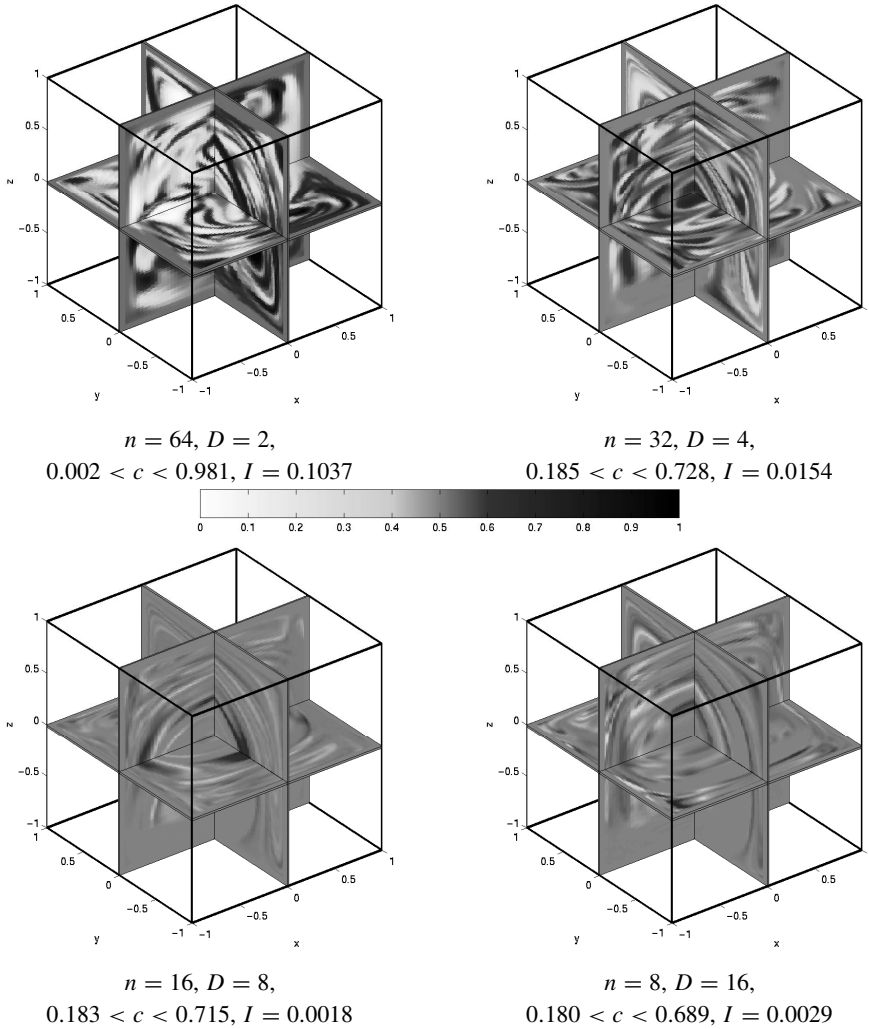


Fig. 3.7: Dependence of the mixing efficiency of the protocol $F_r B_l F_l B_r F_d B_u F_u B_d$ on the dimensionless displacement. The energy input in all cases is the same. Number of steps n , dimensionless displacement D , range of the concentration c and intensity of segregation I are stated under each image.

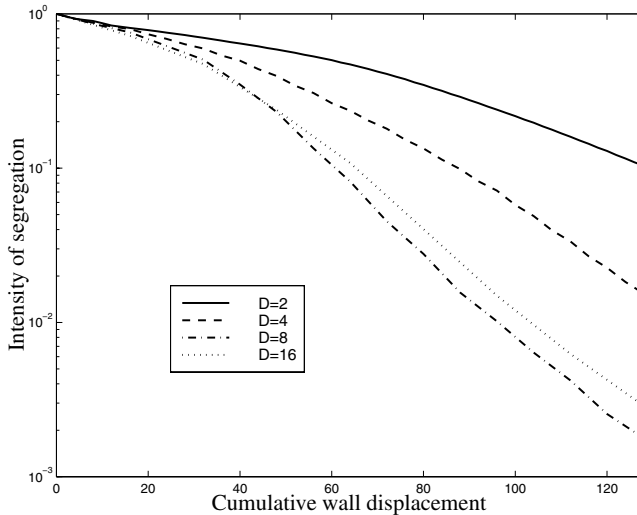


Fig. 3.8: Intensity of segregation vs cumulative wall displacement for protocol $F_r B_l F_l B_r F_d B_u F_u B_d$ with different dimensionless displacement D . The same four cases as in figure 3.7 are considered.

3.6 Conclusions and discussion

A mapping approach for analysing three-dimensional laminar distributive mixing has been developed. This method is an extension of the two-dimensional technique. It offers a fast and efficient way to predict long-term mixing and to compare different mixing protocols. The method requires extensive computations to create the mapping matrices that describe the mappings, but such computations are only performed *once* and strongly benefit from parallelization. Once the mapping matrices are computed, they can easily be used to construct different mixing protocols, which is not computationally expensive.

A relatively simple prototype mixing flow in a cubic domain is used to test the mapping approach for three-dimensional mixing simulations. The reliability of the technique was confirmed by comparison with the results of adaptive front tracking for a small number of cycles. The interface shape recovered from the mapping results closely matches the surface of the same initial volume of marker fluid that was explicitly tracked in the flow. Comparison of the results obtained using mappings with different spatial resolution shows that a finer spatial discretization is more important than larger time steps that reduce total number of mappings. It is demonstrated that the mapping technique can be used to compare the mixing efficiency of different protocols. Intensity of segregation is used to characterize the overall degree of mixing. Although this parameter depends on the spatial resolution, the comparative results and revealed trends are similar for different resolutions. Thus, this mixing measure is reliable to use for comparison of mixing protocols. The mapping method can also be used to adjust the parameters of the selected flow protocol to achieve optimal mixing with the same energy input. Moreover, the mapping technique is general and can be applied for studying fluid mixing in systems with more complex geometries, which will be demonstrated in the next chapters.

Chapter 4

Three-dimensional space-periodic flows in static devices

4.1 Introduction; the multiflux static mixer

The multiflux static mixer, described by [Sluijters \(1965\)](#), is an example of a three-dimensional space-periodic flow. This mixer is a static mixing device commonly used in industry that closely mimics the bakers transformation, as schematically shown in figure 1.1, chapter 1. An element of the multiflux mixer (see figure 4.1) comprises two flow channels that first narrow in one direction and then expand in the other direction. The next element is placed in such a way that the fluid flow is first cut before it is contracted again (the orientation of the compressive part of all elements is always the same). In order to prevent a preferential channel for the fluid, the elements are alternatingly stacked in a clockwise/counterclockwise orientation of the channels. If only clockwise or counterclockwise elements would be used (figure 4.1c), the fluid would essentially flow through two square pipes.

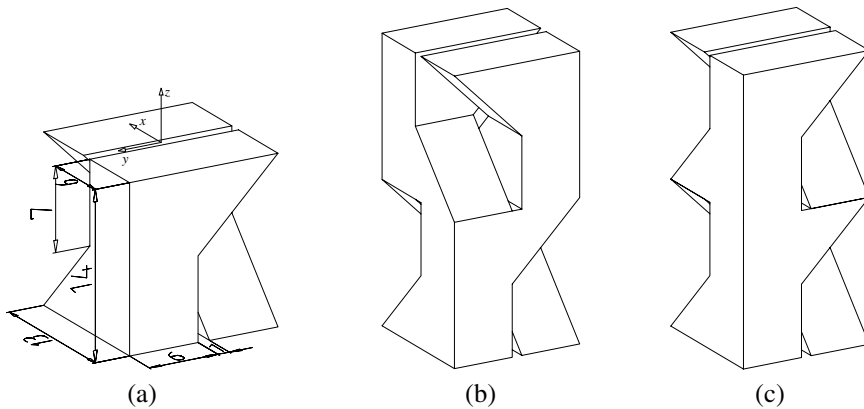


Fig. 4.1: a) Dimensions of a single multiflux mixer element; two multiflux static mixer configurations: b) alternatingly stacked elements; c) identically stacked elements; the preferential channel is clearly visible.

The multiflux mixer is ideal for mixing two fluids that have a similar rheological behaviour. In each element the number of layers is doubled, and, as the device has no moving parts, it is not sensitive to wear and can be incorporated into existing piping. Due to the non-uniform velocity profile, however, the formed layers are not of equal thickness. Also, the

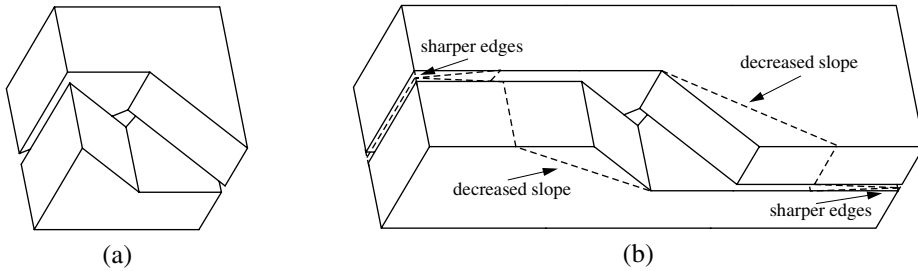


Fig. 4.2: a) Conventional multiflux element; b) improved versions of the multiflux element, the dashed lines indicate the geometry of the second improved geometry.

influence of the velocity field on residence time distribution is of importance when degrading or reacting polymers are regarded. By using the mapping method the layer thickness and residence time distribution are investigated for three configurations: the original configuration as reported by [Sluijters \(1965\)](#) (see figure 4.2a), an improved configuration as proposed by [van der Hoeven et al. \(2000\)](#) (see figure 4.2b), and a second, further, improved model, that has sharper leading and trailing edges on the flow dividers and has a decreased slope towards the contraction (the dashed lines in figure 4.2b). The general dimensions of the conventional mixer element are shown in figure 4.1a. Width and depth of the improved geometries are equal to those of the conventional geometry; the height has been increased by a factor three. The improved mixer elements should perform better in terms of layer thickness distribution and edge distortions, although at the cost of a higher pressure drop over an element due to their increased length.

According to [Moffatt \(1964\)](#), the critical angle for the formation of corner eddies (or effectively stagnation zones) is approximately 146° . Therefore, for the third geometry investigated the angle of the mixing element is increased from 135° to 153° ($153^\circ \approx \arctan 2 + 90^\circ$: the tapered side has been made twice longer). This change, along with the sharpened divider edges should reduce the inhomogeneities in the layer thickness, but it is obvious that it also further increases the pressure drop over the element since the hydraulic resistance increases.

4.2 Computational method and boundary conditions

The velocity field in the multiflux static mixers has been analysed using a spectral element method ([Maday & Patera \(1989\)](#), [Timmermans et al. \(1996\)](#), [Anderson \(1999\)](#)). The particular implementation used decouples the three velocity components and the pressure. The system is solved by an iterative solution algorithm that applies a low order, finite element, preconditioner. This is of particular interest for the types of geometry under investigation since the total number of degrees of freedom is too high to use explicit solver algorithms like LU or Choleski decomposition (see table 4.1 for details). The iterative solver does not require that the full spectral element system matrix has to be stored, since only matrix vector multiplications on element level are required.

On all walls homogeneous Dirichlet boundary conditions were imposed. At the exit the pressure $p = 0$ was prescribed. At the entrance, a fully developed flow for a rectangular duct

Tab. 4.1: Properties of the multiflux spectral element problem.

	conventional	improved 1	improved 2
# spectral elements	742	952	640
order	10	10	10
# finite elements	742,000	952,000	640,000
# nodes	792,974	1,003,158	678,880
# velocity unknowns	2,080,920	2,710,028	1,809,248
# pressure unknowns	786,132	998,496	675,478
# unknowns (total)	2,867,052	3,708,524	2,484,726

was enforced. The velocity in z -direction, u_z , for a rectangular section of dimension $2b \times 2a$ with $-a \leq x \leq a$ and $-b \leq y \leq b$ is given by [Ward-Smith \(1980\)](#):

$$u_z(x, y) = -\frac{1}{2\mu} \frac{d\hat{p}}{dx} \left[b^2 - y^2 - \frac{4}{b} \sum_{n=0}^{\infty} \frac{(-1)^n \cosh N_n x}{N_n^3 \cosh N_n a} \cos N_n y \right]. \quad (4.1)$$

The volumetric flow rate Q is given by:

$$Q = 4abU = -\frac{1}{\mu} \frac{d\hat{p}}{dx} \left[\frac{4}{3} ab^3 - \frac{8}{b} \sum_{n=0}^{\infty} \frac{\tanh N_n a}{N_n^5} \right], \quad (4.2)$$

with

$$N_n = \frac{(2n+1)\pi}{2b}. \quad (4.3)$$

The average inflow velocity U was set to 1.0. Of equations 4.1 and 4.2 ten terms were computed. The break-off error is of order 10^{-3} .

4.3 Determination of the mapping matrix

Since the multiflux static mixer consists of two identical channels, only one channel needs to be computed to determine the mapping matrix. The mixer clearly is a space-periodic mixer, therefore mapping is computed from one cross-section to the next, so subdomains are defined on the cross-section at the entrance of an element. Since it is unknown beforehand at what time t_e a particle crosses a cross-section at $z = z_e$, it is advantageous to integrate over z instead of t , since z_e is determined by the length of a channel. This is realized by applying the following substitution:

$$\int_{t=t_0}^{t_e} \mathbf{u} dt = \int_{t=t_0}^{t_e} \mathbf{u} \frac{u_z}{u_z} dt = \int_{t=t_0}^{t_e} \frac{\mathbf{u}}{u_z} \frac{dz}{dt} dt = \int_{z=z_0}^{z_e} \frac{\mathbf{u}}{u_z} dz. \quad (4.4)$$

Similarly, the residence (or travel) time for a tracer from one cross-section to the next, can be determined by:

$$\int_{t=t_0}^{t_e} dt = \int_{t=t_0}^{t_e} \frac{1}{u_z} \frac{dz}{dt} dt = \int_{z=z_0}^{z_e} \frac{1}{u_z} dz. \quad (4.5)$$

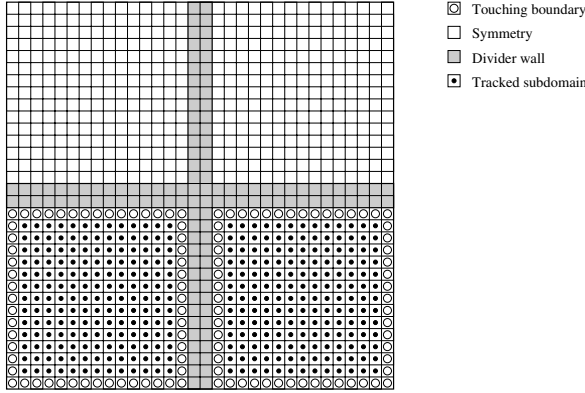


Fig. 4.3: Schematic representation of the subdomains in a cross section of the multiflux mixer. The grey subdomains are not tracked (on the divider walls), the unmarked subdomains are not tracked but symmetry conditions are used. The subdomains indicated with \circ are extrapolated from the tracked subdomains indicated with \bullet .

These substitutions are allowed as long as $u_z \geq 0$. Since on the boundaries $u_z = 0$, subdomains with edges on these boundaries were not tracked. Also, since u_z reaches 0 near the divider walls (the walls that ‘cut’ the flow), the subdomains were tracked to a height 0.05 upstream of the actual divider wall (at most 0.4% of the element height).

The residence time of tracer particles is computed using equation 4.5. This results in one residence time per node on the tracked boundary of a subdomain. The number of nodes on the boundary of a subdomain depends on the deformation of the subdomain. Since only a fixed number of properties per subdomain can be mapped, the different residence times of the tracers on the boundary need to be averaged. A subdomain is described by a closed boundary with N_t tracers with coordinates \mathbf{x}_i and residence times T_i . Tracer $N_t + 1$ is identical to tracer 1. The total length L of the boundary of the subdomain is:

$$L = \sum_{i=1}^N \|\mathbf{x}_{i+1} - \mathbf{x}_i\|. \quad (4.6)$$

The average residence time \bar{T}_k of subdomain k is now defined as:

$$\bar{T}_k = \frac{1}{2L} \sum_{i=1}^N (\|\mathbf{x}_{i+1} - \mathbf{x}_i\|) (T_i + T_{i+1}). \quad (4.7)$$

The average residence times for the subdomains are stored in a residence time column $\bar{T}^{(0)}$. Since time is an additive property of the flow, the mapping operation becomes:

$$\bar{T}^{i+1} = \Phi \cdot (\bar{T}^{(i)} + \bar{T}^{(0)}). \quad (4.8)$$

The cross-section has been subdivided in a grid of 130×130 subdomains. Not all of these subdomains are tracked (see the schematic representation in figure 4.3; the subdomains shown

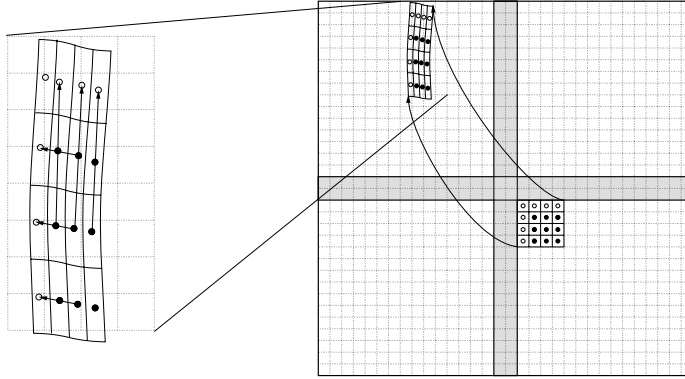


Fig. 4.4: Extrapolation of untracked subdomains. The centre of gravity of the domains indicated with \bullet is determined by means of equation 4.9. These points are used to extrapolate the position of the centre of gravity from the subdomains on the boundary (indicated with \circ).

here are just an indication, the actual grid is finer). The subdomains that lie on the divider wall (grey in the figure), are marked not to be tracked, as are the subdomains that have a common boundary with these divider walls or the outer walls (\circ in the figure). Further, due to the aforementioned pointwise symmetry with respect to the centre of the element, only one half of the remaining subdomains is tracked (the subdomains marked by \bullet). The contributions of the unmarked subdomains to the mapping matrix can be found using this symmetry.

The subdomains that were not tracked can be handled in two different ways: they can all be regarded as one large reservoir with an average concentration or their contribution can be estimated from the deficit of subdomains in their neighbourhood. The first method leads to a large grey area near the walls of the multiflux mixer, that tends to grow every mapping. The second method gives an estimation for the contributions to the mapping matrix of the subdomains near the wall. Although still not very accurate, the prescribed concentrations are expected to be more accurate than the average concentration prescribed in the first approach and, therefore, the second method will influence the concentration distribution less.

In order to determine the approximate mapping coefficients Φ_{ij} of the subdomains near the boundary, the centre of gravity of all tracked subdomains is determined (see figure 4.4). Since the boundary description of the subdomains is not retained, the centre of gravity \bar{x}_i^* of tracked subdomain i is estimated using the mapping matrix Φ by:

$$\bar{x}_i^* = \sum_{j=1}^N \Phi_{ij} \bar{x}_j, \quad (4.9)$$

that is, for every subdomain j that subdomain i has donated fluid to, the centre of gravity of \bar{x}_j of that subdomain is weighted with the fraction of fluid in that subdomain that originated from domain i . Then, for every subdomain that is in the flow domain but has not been tracked (indicated with \circ in figure 4.3), its centre of gravity is extrapolated linearly from its adjacent domains (see figure 4.4). Of the subdomains that received a contribution less than 80% from donor subdomains, the nearest centre of gravity of an extrapolated subdomain is

determined (extrapolated by means of equation 4.9). The deficit of the acceptor domain is accredited to the donor domain the extrapolated centre of gravity belongs to. In first instance, extrapolation is performed using tracked subdomains only. For any untracked subdomains left, the extrapolated subdomains are used. This approach is used to compute the results presented in the next section.

4.4 Results

For each of the three mixer geometries, a different mapping matrix was needed, since the changes in geometry substantially changed the velocity field in the mixer channels and hence the coefficients in the mapping matrices. Still, only one mapping matrix per geometry is needed to determine the influence on the layer thickness distribution and residence time distribution after a number of elements. The accuracy of the striation thickness that can be visualized by the mapping method is determined by the resolution of the subdomain grid, and is independent of the size and order of the spectral elements used for the velocity computations, provided that the velocity approximation is accurate enough.

In figure 4.5 the concentration distribution for the three different geometries is shown after the first through the fifth element. Initially the left part of the mixer was filled with black fluid and the right part with white fluid. The mixer channels first contract in the x -direction and then expand in the y -direction.

The top row of figure 4.5 already clearly shows the difference between the conventional and the improved geometries. In case of the conventional geometry, the flow is not split into two equal parts, but is roughly divided 64%/36% (averaged over the channel width). This is in agreement with the experimental results presented by [van der Hoeven et al. \(2000\)](#). The first adapted geometry has a black/white ratio of approximately 53%/47%, the second of 52%/48%.. The top left figure also shows that the cut is not optimal: on the horizontal walls the fluids start to ‘curl’. This already happens at an early stage, and since the effect is cumulative, the layers get a rather irregular shape. After five elements of the conventional multiflux mixer it is evident that the layer thickness distribution is far from ideal with respect to the homogeneity of the layers. A large amount of fluid is still located near the outer walls.

Also, the first improved mixer suffers from the edge curling, but it starts at the second mixing element and is less pronounced, although after the fourth element the white fluid nearly touches the left wall in the lower left channel. The second improved geometry suffers less from edge curling, especially near the divider walls. This result is expected since the divider walls do not form as big a barrier as in the conventional and first improved mixer. However, as the contribution to the subdomains near the walls is extrapolated, the curling of the layers can only be regarded as an indication of what might occur. In both improved geometries, the layers grow thicker more gradually from the centre of the channel to the walls and the layer thickness distribution in the mixer is more homogeneous. Since the outflux determines the actual layer thickness distribution, the gradual increase of layer thickness inside the mixer element is not unwanted: the flux in regions near the walls is lower and therefore the layers need to be thicker in order to realize a comparable total ‘flux per layer’.

Residence time, or more specific, residence time distribution, is of importance when degradation or chemical reactions between the two components occur. In figure 4.6 the logarithm of the residence time is shown. The residence time is averaged over $-6.5 < y < 0.5$. In

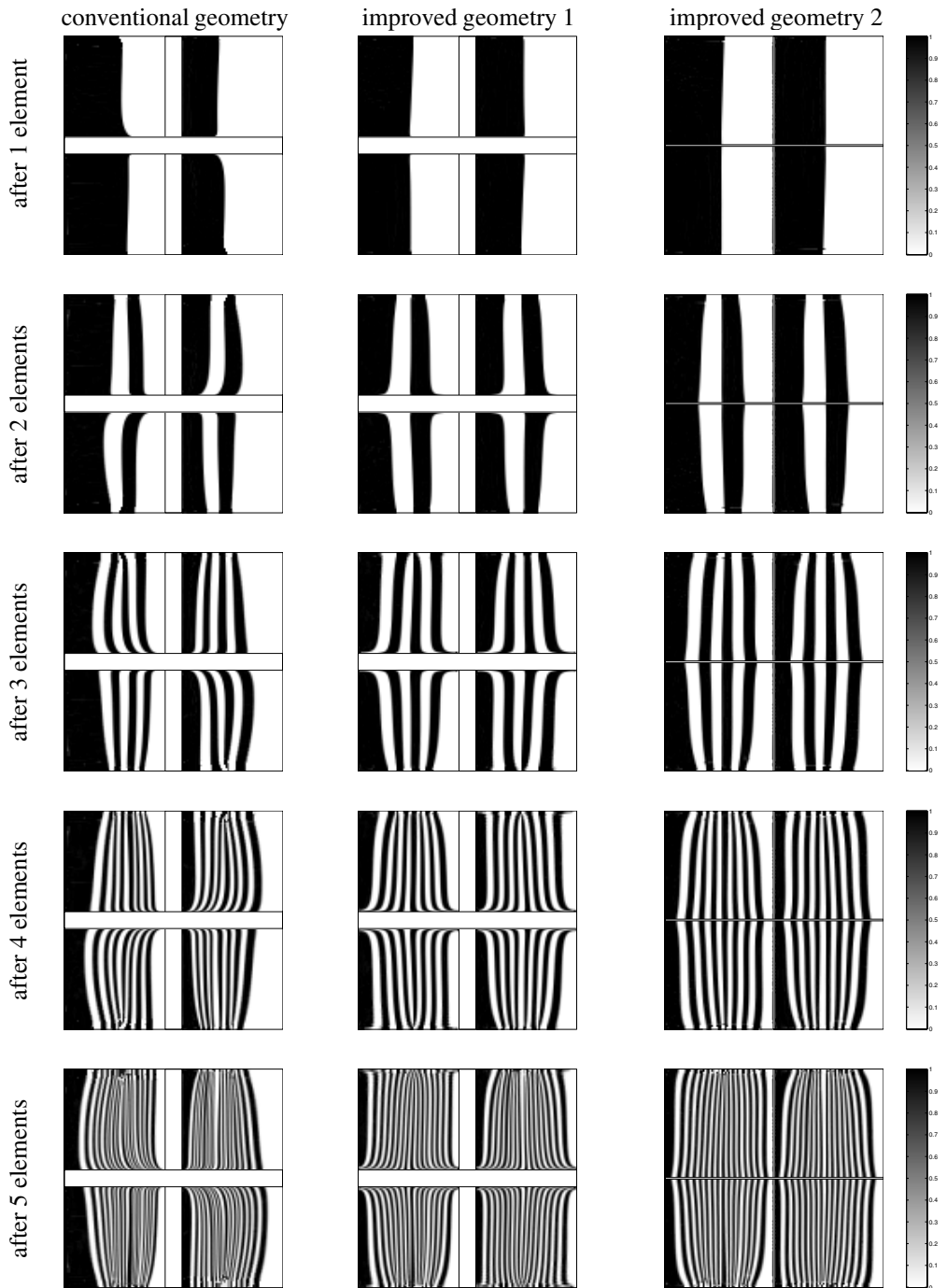


Fig. 4.5: Concentration distributions on cross-sections in the different multijet mixers.

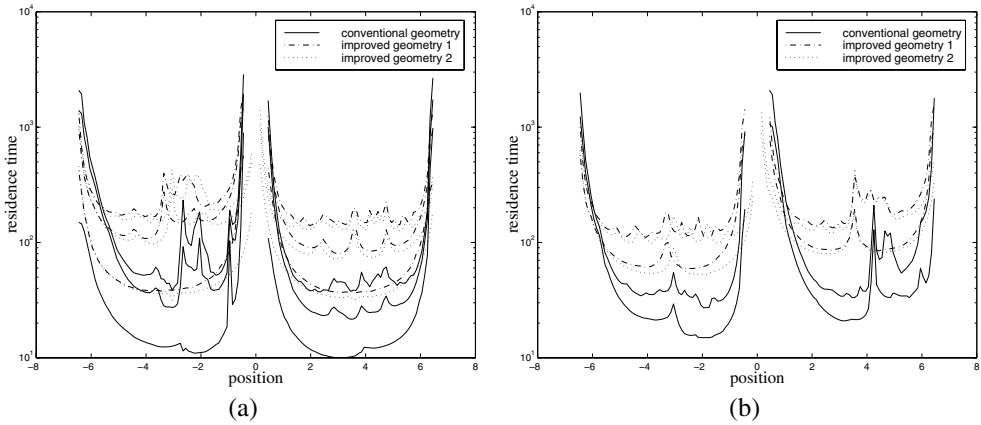


Fig. 4.6: Residence time distribution in the three different multiflux geometries. Mean residence times are plotted after: a) the first, third and fifth element b) the second and fourth element (from bottom to top). The average is taken over $-6.5 < y < 0.5$.

x -direction the residence time is as would be expected from a laminar flow through a channel: high near the walls and decreasing towards the centre of the flow. Obviously, the smallest residence times are realized by the conventional mixer. However, the highest residence times in the conventional mixer are in the same range as those of the three times longer and improved elements. Although the actual highest residence time is infinite due to the no-slip conditions on the wall, this means that the fluid flow near the walls stagnates more in the conventional geometry. This also explains why the fluid flow is not cut into two layers of more or less equal thickness. This can also be observed by regarding the residence time distributions after one conventional element (bottom solid lines in figure 4.6): the residence times in the fluid closest to the outer walls are higher than those of the fluid near the inner (divider) wall.

4.5 Conclusions and discussion

In this chapter the application of the mapping method on three-dimensional space-periodic flows is discussed. It has been shown that by using a space-periodic approach, concentration and residence time distributions can be easily obtained. The main advantage is that the mapping matrix only needs to be computed for one element in order to determine the concentration or residence time distribution after a number of elements. It is demonstrated that the mapping method can be used to improve the design of a static mixer element in terms of final layer distribution. Using explicit boundary tracking or volume of fluids methods five elements would need to be modelled and computed for the results shown in this chapter, which, at the moment, is prohibitively expensive in terms of computer resources. In the case of volume of fluids methods, the obtainable layer thickness is determined by the order of the elements and the spatial discretization of the fluid domain, which is identical to the discretization for computation of the velocity field. Further, these methods require long simulated tracking times in order to reach a state where the boundaries of the tracked layers (nearly) touch. This

problem is solved by the mapping method. If the layer thickness distribution needs to be computed beyond the resolution of the mapping grid, the mapping method may be extended with mapping of the area tensor (see chapter 2 and appendices C and D). The area tensor will indicate the interfacial area in a subdomain, and since the size of the subdomain is known, it will be a measure for the number of layers inside the subdomain.

The mapping method benefitted from the possibility to track particles in the z domain instead of the t domain. It reduced the efforts to track from one z -level to the next, without additional checking whether particles had crossed the end level (the minimum level needed to compute the mapping matrix for one element). Explicit boundary tracking methods can also benefit from this transformation in order to investigate layer thickness distribution at a particular level.

To determine the effects near the wall, the coefficients of the mapping matrix that were linked to subdomains near the wall, had to be extrapolated. This extrapolation has been performed by extrapolating the centres of gravity from subdomains near the untracked subdomain. Since at the time of computing those centres, the boundaries of the individual subdomains were not available anymore, the centre of gravity of a subdomain was estimated by taking a weighted average over the centres of gravity of the (initial) subdomains it effected. The accuracy of the extrapolation can be improved by determining the centre of gravity of tracked subdomains at the time where the boundary of that subdomain is still known, i.e. in the slave routine of the tracking program.

The mapping method for this type of mixer is restricted to the case where the two fluids have a similar rheological behaviour. If the flow of two rheologically different fluids needs to be simulated, the mapping method will not be a proper choice, since the velocity field will change from one mixer element to another. In that case, explicit boundary tracking and volume of fluids methods will possibly be better choices, although at the moment not feasible for the number of mixing elements considered here.

Chapter 5

Three-dimensional periodic flows in dynamic devices

5.1 Introduction; co-rotating twin screw extruders

The most commonly used mixing device in polymer processing is the closely intermeshing, co-rotating twin screw extruder. Although in essence simply a polymer melting and transport device, its screws are constructed in a modular way in order to create different screw geometries to increase mixing performance. Some common elements are shown in figure 5.1. In general, a screw consists of a long transport part followed by a kneading section, where the polymer granulate is molten. Subsequently, alternating transport and kneading sections are created where additives are mixed in, blending takes place and, finally, the polymer melt is degassed (vented). Since co-rotating twin screw extruders are starved-fed (less polymer granulate is metered into the extruder than theoretically could be transported) the kneading screw sections will only be partially filled, which has a negative effect on the efficiency. To keep the subsequent sections filled, neutral and counter-conveying (negative) kneading sections are applied, as well as the more effective, and thus generally shorter, counter-conveying elements. The typical combination of transport, kneading, and counter-conveying elements is repeated along the screw axis when additives are fed and mixed into the melt (by e.g. a sidefeeder) and when composition and temperature-homogeneity is being improved.



Fig. 5.1: Basic types of twin screw extruder elements. From left to right: conveying element, counter conveying element, conveying kneading section, neutral kneading section and counter conveying kneading section.

In this chapter, as a further development of the mapping method and an example of the analysis of real mixing devices, the mixing performance of the transport elements of a closely intermeshing, thus self-wiping, co-rotating twin screw extruder will be studied. An adapted form of the mapping method is used, where a mapping matrix works sequentially on only a part of e.g. the concentration distribution column for the entire extruder.

To analyse mixing behaviour in more complex, dynamic mixers, up to now, mixing studies in dynamic devices are based on relatively straightforward analyses of the flow field ((Szydowski & White, 1988), Yang & Manas-Zloczower (1992)) studying the complex ve-

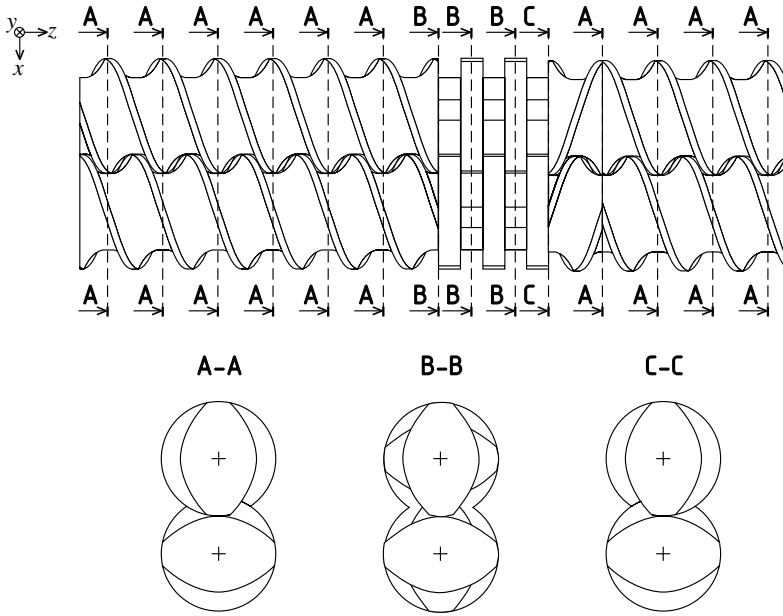


Fig. 5.2: Space-periodicity in a twin screw extruder, the cross-sections A–A, B–B and C–C are all similar.

locity and pressure gradients in detail. More elaborate mixing analysis of dynamic mixers used the evolution of the distance between two initially close particles (Wong & Manas-Zloczower, 1994), the correlation between particles and concentration of particles initially gathered as clusters (Yang & Manas-Zloczower (1994), Funatsu *et al.* (1999)), or particle position history or mixing index (Hutchinson *et al.*, 1999). These methods, however, constitute the same drawbacks as discussed in previous chapters: tracked particles are infinitesimal, they do not represent a volume and, since mixing in well-designed mixers typically is of a chaotic nature, therefore are of limited use to investigate concentration distributions.

5.2 Time- and space-periodicity

The elements of a twin screw extruder can be regarded as space as well as time-periodic. It is space-periodic in the sense that cross-sections perpendicular to the screw axes repeat after some distance (determining the spatial period) along the axis (i.e. the orientation of the screws is identical compared to a previous cross-section, see figure 5.2). For transport or counter-conveying elements, this distance is determined by the pitch angle of the screw. The extruder is time-periodic in the sense that after each revolution, the screw is back in its initial position. In figure 5.3 the time-periodicity is illustrated; after one rotation ($\frac{t}{T_P} = 1$; T_P is the time needed for one full rotation of the screws), the screw is back in its original position. For a screw element with two lobes, an identical orientation is also reached after a half rotation

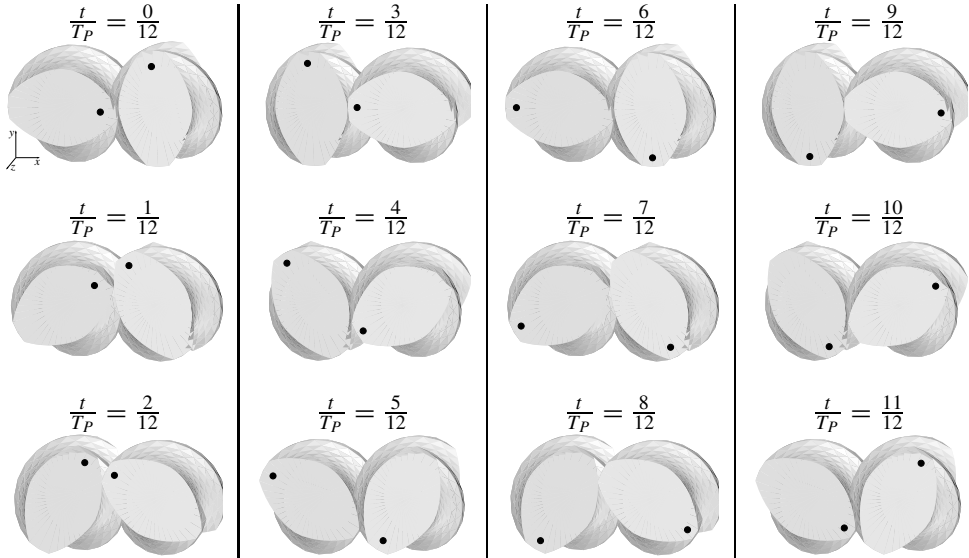


Fig. 5.3: Time-periodicity of a twin screw extruder.

($\frac{t}{T_P} = \frac{1}{2}$), however, an entire screw may also contain single and three lobe elements that have an equal cross-section after a full and a third rotation, respectively.

The manner in which the screw is regarded determines how the mapping matrix needs to be computed and what data can be retrieved. When regarded from a time-periodic point of view, data are available along the entire screw. This makes it possible to study the mixing quality along the screw as well as the progression of fluid through the extruder in time. However, this is only possible for some discrete orientations of the screw. In this case, the number of screw orientations constitutes the computing effort. The space is divided in a grid of cells with a certain volume. The coefficients of the mapping matrix are determined by intersections of the deformed cells with the initial cells. In this case, the time Δt spanned by the mapping matrix, is the time needed for a screw rotation and of no further physical meaning. The time-periodic approach describes the concentration distribution of the *entire* screw in one concentration column.

From a space-periodic point of view, only data at certain cross-sections can be obtained (see chapter 4), and, since the screws are rotating, these data are a function of the orientation of the screw. The intersections that determine the coefficients in the mapping matrix need to be determined in a space spanned by the x - and y -coordinate of the tracer particles as well as the orientation of the screw at the time the particle reached the cross-section. In this case the distance between two cross-sections Δz is constant per mapping matrix, and it is possible to determine the average, minimum and maximum residence time of fluid passing through the cross-section. The mixing quality can also be determined at these cross-sections. The number of cross-sections per element constitutes the computing effort. In the space-periodic approach concentration (or any other quantity that can be mapped) is mapped from one cross-section to

the next. It therefore does not describe the concentration distribution along the entire screw. Instead it gives the concentration distribution at a cross-section for all possible orientations of the screws in that cross-section.

Space-periodic mapping is more expensive in terms of computing time than time-periodic mapping. In time-periodic mapping, volumes are deformed during a fixed amount of time. In space-periodic mapping, tracers are followed from one cross-section to the next, for a number of different screw orientations. The time tracers need to travel that distance is not known beforehand. Since backflow occurs near the edges of the screws, variable substitution as used in chapter 4.3 is not possible. This means that tracers have to be tracked in time. Tracers near the barrel wall or near the screws travel slowly with respect to tracers near the centres of the channel. The deformations of the mapping grid will, therefore, be larger than in the time-periodic approach. Consequently, more tracers need to be tracked, increasing the computational cost. Furthermore, determination of intersections from the tracked grid with the initial grid will also become more computationally expensive. As a consequence, the time-periodic approach is followed.

5.3 Geometry of the screw

A number of different descriptions for the screw geometry of co-rotating twin screw extruders exist ((Booy, 1978), Booy (1980), Chen & White (1994), Potente *et al.* (1994)). Here, a slightly adapted version of the description for a self-wiping profile provided by Chen & White (1994) is used:

$$l(\theta) = \begin{cases} R_S(\rho_c - 1) & 0 \leq \theta \leq \frac{\alpha}{2} \\ R_S \left[\sqrt{\rho_c^2 - \sin^2(\theta - \frac{\alpha}{2})} - \cos(\theta - \frac{\alpha}{2}) \right] & \frac{\alpha}{2} \leq \theta \leq \frac{\alpha}{2} + 2\psi \\ R_S & \frac{\alpha}{2} + 2\psi \leq \theta \leq \frac{\pi}{N_T} \end{cases} \quad (5.1)$$

where $l(\theta)$ is the distance from the centre to the edge of the screw (see table 5.1 and figure 5.4 for other properties and values of the parameters). The geometrical relations of the parameters are:

$$\rho_c = \frac{C_L}{R_S}, \quad (5.2)$$

$$\psi = \arccos(\rho_c/2), \quad (5.3)$$

$$\alpha = \frac{\pi}{N_T} - 2\psi. \quad (5.4)$$

For all basic screw types, shown in figure 5.1, the cross-section is identical and only the pitch is varied. The transport screw analysed in this chapter was modelled after the screws of a Werner & Pfeleiderer (W&P ZSK-25) laboratory extruder.

5.4 Computational method and boundary conditions

Several techniques exist to determine the flow field in complex geometries numerically. An elegant method that reduces the difficulty of creating complex volume meshes is the fictitious domain method (Glowinski *et al.* (1994a), Glowinski *et al.* (1994b), Bertrand *et al.* (1997),

Tab. 5.1: Screw geometry parameters.

	parameter	value
Screw radius	R_S	12.50 [mm]
Screw centre distance	C_L	20.85 [mm]
Clearance	δ_0	0.20 [mm]
Number of lobes	N_T	2 [-]
Pitch	p	24.00 [mm]

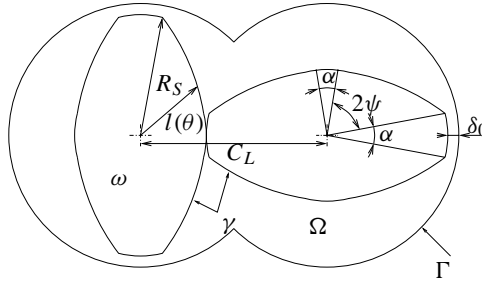


Fig. 5.4: Profile of a self-wiping screw pair.

van Rens (1999)). The spatially discretized computational domain consists of a flow domain Ω with boundary Γ . Inside this domain is a fictitious domain ω with boundary γ (see figure 5.4). The flow is considered to be isothermal, laminar and inertia effects are neglected. It is described by the Stokes and continuity equations:

$$\eta \Delta \mathbf{u} - \nabla p = \mathbf{0} \quad \text{in } \Omega \setminus \bar{\omega}, \quad (5.5)$$

$$\nabla \cdot \mathbf{u} = 0 \quad \text{in } \Omega \setminus \bar{\omega}, \quad (5.6)$$

where $\bar{\omega}$ is the closure of ω ($\omega \cup \gamma$). The main mesh describes the full internal ('eight-shaped') domain Ω of the extruder with boundary Γ . A description of the screw ω with boundary γ is then provided and Dirichlet boundary conditions are imposed on the surfaces. The boundary conditions on γ are incorporated in the finite element analysis via Lagrange multipliers. The finite element discretization and surface description of the screw are shown separately in figure 5.5. The flow domain is subdivided in eighty layers of approximately 9000 first order $P_1^+ P_1$ MINI elements (van Rens, 1999) per level. Three extruder transport element pairs were modelled of which the middle pair is used to compute the mapping matrix in order to exclude effects due to in- and outflow (see figure 5.5c).

Only fully filled screw parts are considered (no air or second fluid phase is present). The flux is chosen such that the extruder is starved (such that pressure is built-up and a pressure flow is generated). In order to determine a realistic flux, the coefficient of fill is chosen to be 40%, a practical value that guarantees sensible drag and pressure flows in the fully filled sections of the screw. An angular velocity of the screws of π [rad/s] (30 rpm) is imposed on

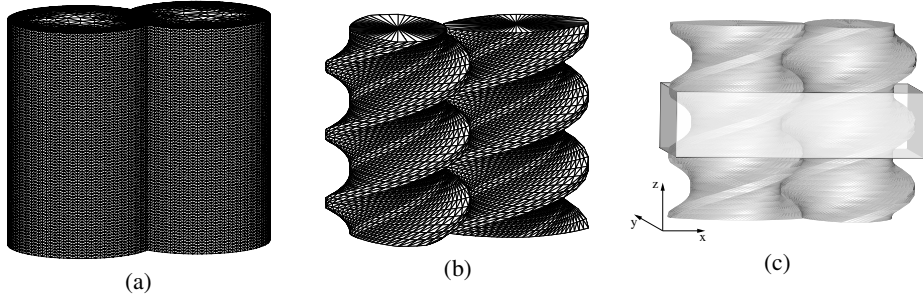


Fig. 5.5: a) Finite element discretization of the flow domain Ω with boundary Γ and b) surface description γ of the screw c) schematic representation of the mapping domain, the box around the middle element is subdivided into 184×100 subdomains.

the screws (γ). This velocity may seem rather low, however, since a stationary Newtonian Stokes flow is regarded, the velocity field of the fluid scales proportionally with the velocity of the screws. A free exit flow and a plug entrance flow is enforced.

Since the tracking computations are performed in the second screw element, the plug flow assumption will not influence the results of the tracking computations. With these assumptions and values of the quantities given in the previous section and table 5.1, and by using the results of Meijer & Elemans (1988), Meijer & Elemans (1990), Elemans & Meijer (1990), an entrance velocity u_z of 0.3 [mm/s] is derived.

5.5 Determination of the mapping matrix

The two-lobe screw elements and the extruder domain considered are clearly symmetric, thus only a 90° rotation of the screws needs to be computed for mapping. Furthermore, since Stokes flow is assumed and inertia effects are neglected, the velocity field will be quasi-static. This simplification is used to take the rotation of the screws into account. The rotation $\phi_t(t)$ of the screws is equal to $\omega_s t$ (ω_s is the angular velocity of the screws). The screw flight has a pitch p , thus the screw profile rotates 180° around the screw axis in $\frac{p}{N_T}$. The orientation of the screw profile $\phi_s(z)$ is then equal to $\frac{N_T \pi z}{p}$. Setting $\phi_t = \phi_s$ gives the relation between t and z for the transport screw element. Thus, a velocity field needs to be computed for only one screw orientation, from which the velocity fields at all other screw orientations can be easily derived.

The grid used to compute the mapping matrix consists of $184 \times 100 \times 48$ subdomains. From the 48 layers in height, only 24 have actually been computed; by making further use of rotational symmetry around the z -axis, the entries in the mapping matrix for the top 24 layers were filled using the results of the computations for the bottom 24 layers. The properties of the matrix are shown in table 5.2.

The subdomains that fall entirely outside the flow domain (barrel) or inside one of the two screws are ignored for the computations. The nodes of subdomains that are partly outside or on the boundary of the flow domain are translated slightly into the flow (0.05 mm), since the boundaries of the flow domain are first order approximations of the actual curved boundaries,

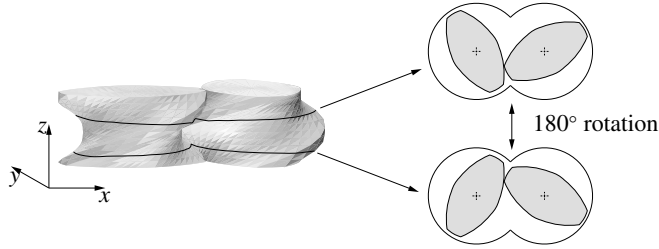


Fig. 5.6: Symmetry in a transport element. The bottom cross-section is similar to the top cross-section rotated over 180° .

Tab. 5.2: Properties of the transport screw mapping matrix.

property	value
$n_x \times n_y \times n_z$	$184 \times 100 \times 48$
# subdomains	883,200
Full matrix size	$1,766,400 \times 883,200$ ($\approx 1.56 \times 10^{12}$)
non-zero elements	13,011,100
matrix density	8.34×10^{-6}

and otherwise it is not guaranteed that the points are actually located inside the discretized flow domain. Since the velocity field was approximated by linear elements, and due to errors in tracking, the volume conservation error ε_V , defined as

$$\varepsilon_V = \frac{|V_0 - V_{tracked}|}{V_{box}} \quad (5.7)$$

where V_{box} is the volume of an uncollapsed subdomain, V_0 is the volume of the collapsed subdomain, and $V_{tracked}$ is the volume of the tracked subdomain, has been large: in one particular case $\varepsilon_V = 100$. These large deviations mainly occurred with collapsed, and thus very small, subdomains near the barrel wall or the screw surface. Especially subdomains that were on one of the screw surfaces and were scraped off during motion by the other screw suffered from very poor volume conservation. This effect is amplified because a small extra velocity was prescribed to tracers that during integration got located outside the barrel wall or inside one of the screws. This extra velocity was in the direction of the flow domain, but it violates mass conservation: the velocity field is no longer divergence free. However, as shown in figure 5.7a, the number of subdomains with a large error is small. Of all tracked subdomains, 4.2% have an error larger than 100%, responsible for 4.6% of the total fluid volume (see figure 5.7b). In total the volume of the tracked elements was 4% larger than the volume of the initial grid.

In an extruder transport takes place from one screw element to another, i.e. the flow is open. This means that in order to determine the mapping matrix for a screw element, also transport from that element to other elements needs to be described. Assuming that no net

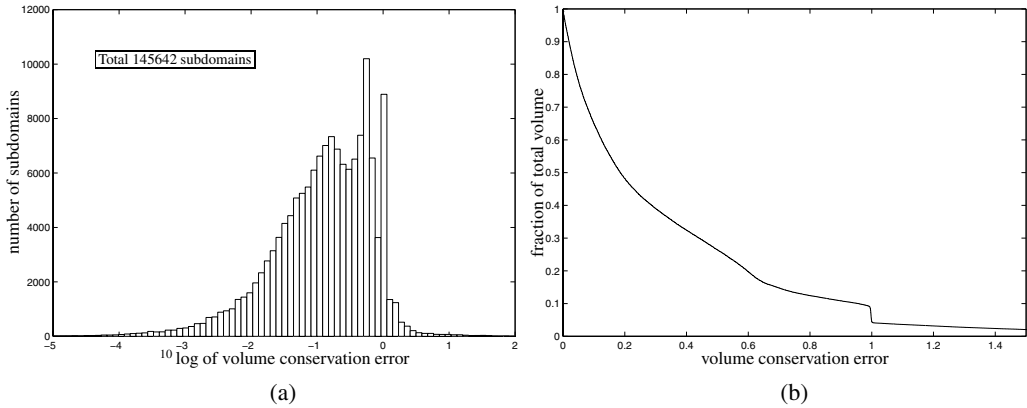


Fig. 5.7: a) Volume concentration error, the logarithm of the error is plotted. b) Fraction of total volume occupied by boxes with indicated error or larger.

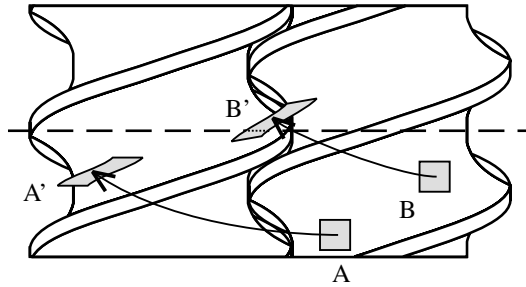


Fig. 5.8: Schematic representation of contribution to Φ_s and Φ_n .

backflow is present during the period for which the mapping matrix is computed and only transport of fluid to the element itself or to the next one occurs, the mapping matrix Φ for a screw element discretized by $n_s (= n_x \cdot n_y \cdot n_z)$ subdomains is of size $2n_s \times n_s$. In this case Φ can be split into two parts: Φ_s that describes the transport of fluid from the element regarded to itself, and Φ_n that describes the transport of fluid from the element regarded to the next element. This is demonstrated in figure 5.8. The initial subdomain indicated by A is advected to A' after one revolution. The advected subdomain A' is still located in the same extruder element as it was initially located in. Therefore, A' will only contribute to matrix Φ_s . Subdomain B on the other hand, is also partly advected to the next extruder element. The contribution of B will therefore be to both Φ_s and Φ_n . If a net backflow is present, or transport of tracers spans more than two elements, submatrices will also need to be computed to take these parts into account, and the mapping matrix Φ will look like $[\Phi_b, \Phi_s, \Phi_n, \Phi_{n+1}]^T$ instead of $[\Phi_s, \Phi_n]^T$ where Φ_b is the part that describes the backflow from an element to the previous element, and Φ_{n+1} describes the transport from an element to the element after the next element.

In the cases presented here, Φ is computed for a quarter rotation. By reordering the concentration column C using the symmetry of the screws and flow domain, the mapping for

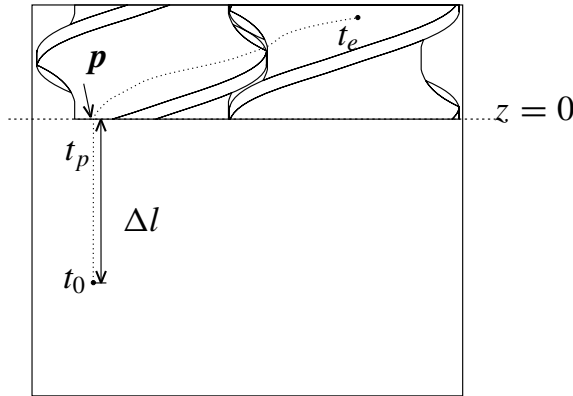


Fig. 5.9: Determination of point of entry and residence time in the extruder for a particle that is transported from one element to the next.

the next quarter rotation can be applied. For the two-lobe profile considered, the screws are in an identical position with respect to their initial position after half a rotation (see figure 5.3).

Since a mapping operation describes the transport of fluid during a certain finite rotation, special care has to be taken to prescribe inflow of fluid. For most of the results presented in this chapter, it is assumed that two differently coloured materials are fed into the extruder; one colour is fed into the left part of the extruder, the other through the right part. We therefore need to know through which half of the extruder the contributions to the matrix Φ_n entered. This is computed by placing a cube of $10 \times 10 \times 10$ equidistantly spaced tracers into a subdomain that received a contribution from the previous element. These tracers are tracked back in time until they pass the boundary $z = 0$ at position p and time t_p (see figure 5.9). From that point p , a constant u_z (the velocity along the extruder axis) is prescribed and both u_x and u_y are set to zero. After tracking the tracers back for a quarter period (the period for which the mapping matrix is computed), it is known which tracer passed through which

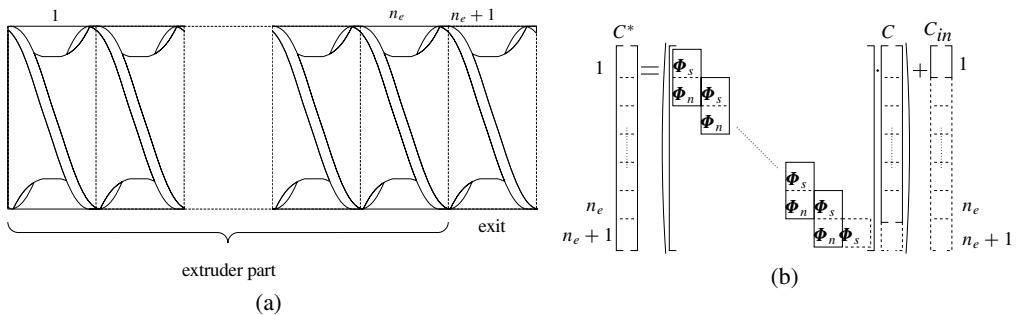


Fig. 5.10: a) Computed part of a screw and b) the resulting matrix-vector multiplication schematically shown.

half of the extruder entrance (since the x and y components of point p have not changed), as

well as the time at which it passed (which is derived from its position in front of the entrance: $t_p = \Delta l / u_z$). Two ‘inflow concentration’ columns C_{in} are created, one for contributions to the screw element that originated from the left half of the entrance, and one for contributions that originated from the right half. The value of the concentration contributions is set proportional to the relative amount of tracers that travelled through the corresponding half of the entrance.

The concentration distribution in any part of the screw is now computed as follows: two concentration columns C and C^* are created with length $(n_e + 1) \cdot (n_x \cdot n_y \cdot n_z)$ where n_e is the number of screw elements that need to be analysed. Then mapping is applied as schematically indicated in figure 5.10*b*. Before performing mapping on column C , the part of it corresponding to the exit element ($n_e + 1$) is set to zero. This offers the possibility to study the outflow in time (the residence time distribution curves discussed later). That part of column C in figure 5.10*b* that is indicated by a dashed line is related to the exit element and therefore need not be part of the matrix-vector multiplications. Computationally it may be more efficient to regard C^* and C as one column, especially if the number of screw elements grows large. In that case, mapping is applied starting from the last element and working towards the entry element, since a mapping operation on screw element i influences element i as well as $i + 1$. After all matrix-vector multiplications are performed, the inflow (C_{in}) is added to the entry element (see figure 5.10).

5.6 Results

Using the geometry and boundary conditions as described in the previous sections, a mapping matrix Φ is computed for a 90° rotation of the screws and extended to a full 360° rotation via application of the symmetry properties as previously discussed. The extruder is entirely filled with white fluid. At $t = 0$ the left channel is fed with blue fluid, the right channel with yellow fluid (configuration and legend are shown in figure 5.11). Four elements are mapped (plus an exit element). In figure 5.13 cross-sections along the z -axis are shown for 0.5–6.0 rotations. This figure shows how the white fluid is being forced out and how blue and yellow fluid fill the channels in time. For more complex geometries, this method is able to detect ‘dead zones’, i.e. regions in the geometry that are not emptied.

Figure 5.12 shows the concentration distribution in four cross-sections (as indicated in figure 5.11 by red lines) at different times, but with identical orientation. It is clear that a stationary distribution is obtained within a few rotations for the first slice, but that changes still occur for the top two slices (for $\frac{z}{D} = 1\frac{3}{8}$ after 4 rotations and for $\frac{z}{D} = 1\frac{7}{8}$ after 5.5 rotations). This indicates that the residence time distribution may not be optimal and should be looked into more closely. This will be discussed later.

Since the function of an extruder is not just to melt and transport polymer, but also to homogenize and mix it, a mixing measure is needed to investigate the mixing properties. Therefore, the intensity of segregation of each slice (a single layer of initial subdomains in the x - y -plane) is computed after 50 screw rotations, thus enforcing a steady state with respect to the concentration distribution. The result is shown in figure 5.14. It is clear that the intensity of segregation decreases with increasing z . After six elements the intensity of segregation starts to oscillate. This is partly caused by the limited resolution of the mapping matrix, used in these preliminary computations. However, the oscillations may also indicate a repeating pattern in the concentration distribution due to the periodicity of the screw. The

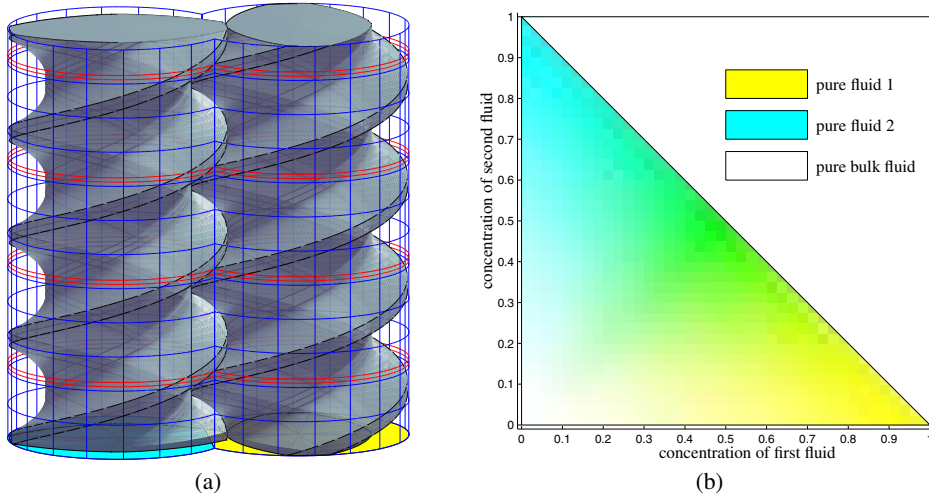


Fig. 5.11: a) Part of twin screw extruder screw that is analysed. The red lines indicate the levels where the cross-sections are shown in later figures. b) Legend of concentration distributions.

plot also indicates that intensity of segregation determined as an average on a screw element (thick line) still decreases after the sixth element, albeit more slowly. This decrease, however, may be a result of the inaccuracies (the ‘numerical diffusion’) of the mapping method.

To further investigate the oscillating behaviour of the intensity of segregation as well as the influence of the initial concentration distribution, an infinitely long extruder is modelled. This infinitely long extruder is created by regarding only a single transport element and prescribing the outflow it generates back to its entrance ($C^* = \Phi_s \cdot C + \Phi_n \cdot C$). The different initial distributions considered are alternating clusters of subdomains on the mapping grid with concentration set to 1 or 0 (three-dimensional checkerboard patterns with maximal intensity of segregation, see figure 5.15). The size of the clusters is varied. Since the domain is discretized on a $184 \times 100 \times 48$ grid, a checkerboard size of 100 means that the domain is divided into four regions of $92 \times 50 \times 48$ that have an alternating concentration (initially the concentration does not vary along the extruder axis in this case). Results are shown in figure 5.16a and b.

The oscillating behaviour of the intensity of segregation is nearly independent of the initial concentration distribution. The mean level for the coarse pattern is slightly higher than for the fine pattern, but this can be explained by the fact that the fine pattern constitutes an ideally premixed concentration distribution. The lines for the other checkerboard patterns investigated were positioned between the top two lines shown in figure 5.16a. It is also obvious that the pattern repeats after 24 slices. This is due to the symmetry conditions used, where the entries in the mapping matrix for the top 24 levels were taken from the bottom 24 levels. The dashed line in figure 5.16 results from 200 mapping steps where an ideal initial concentration distribution is used ($C = \frac{1}{2}$ for all subdomains). The fact that this line resembles the other two lines indicates that the oscillating behaviour is caused by the mapping matrix; ideally, the intensity of segregation for the ideal initial concentration distribution

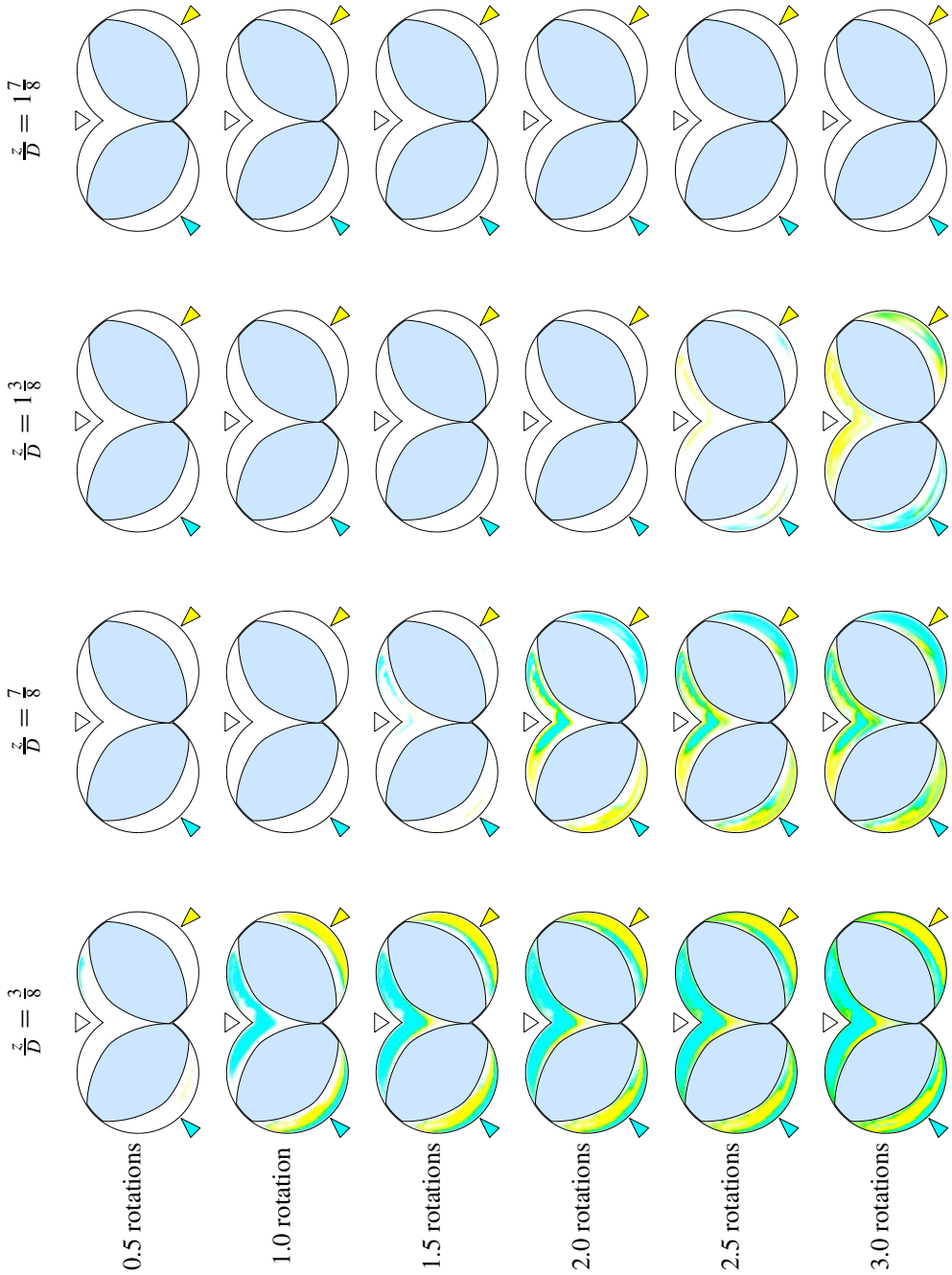


Fig. 5.12: (a) Concentration distribution at various cross-sections along the extruder.

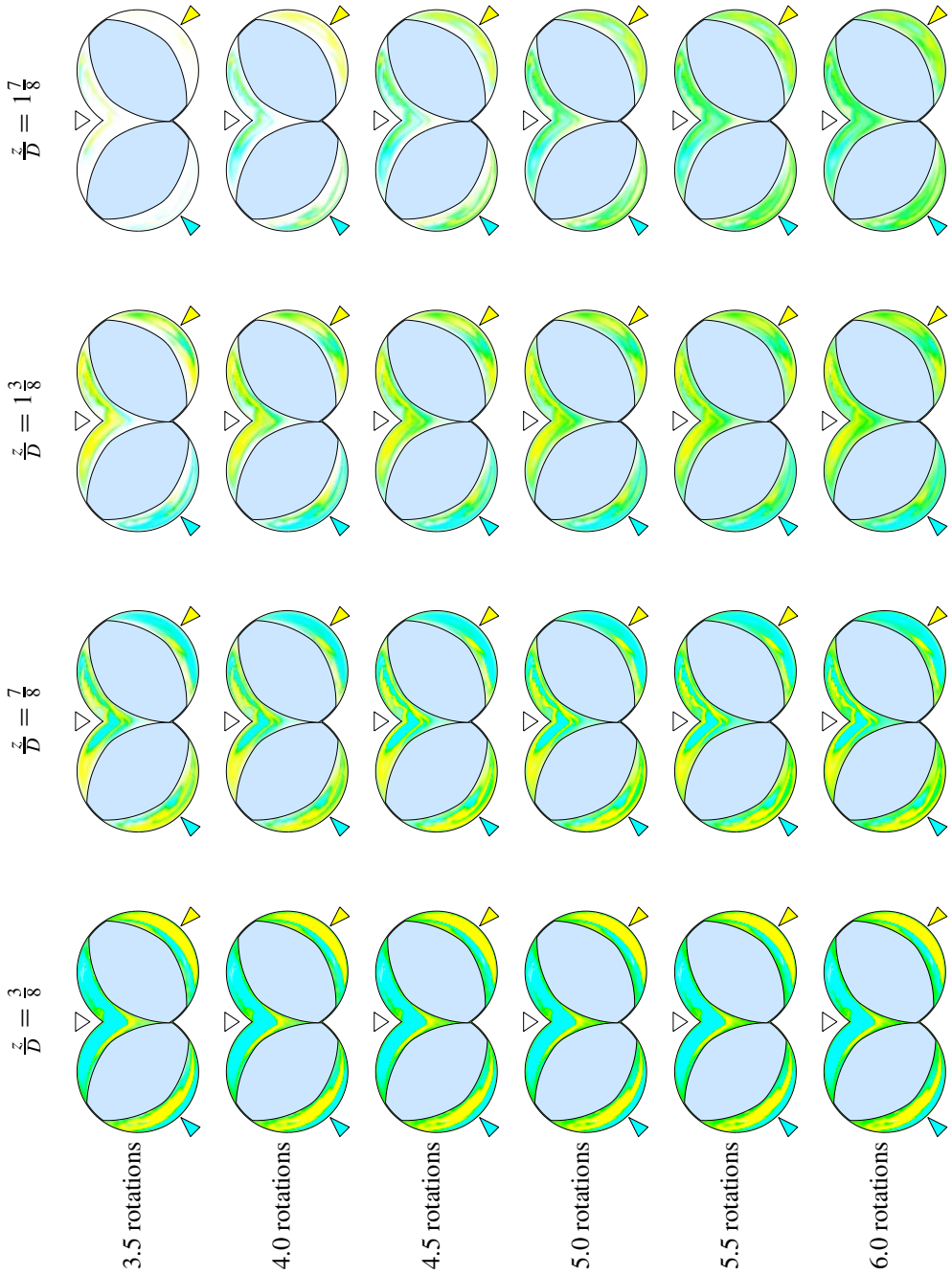


Fig. 5.12: (b) Figure 5.12a continued.

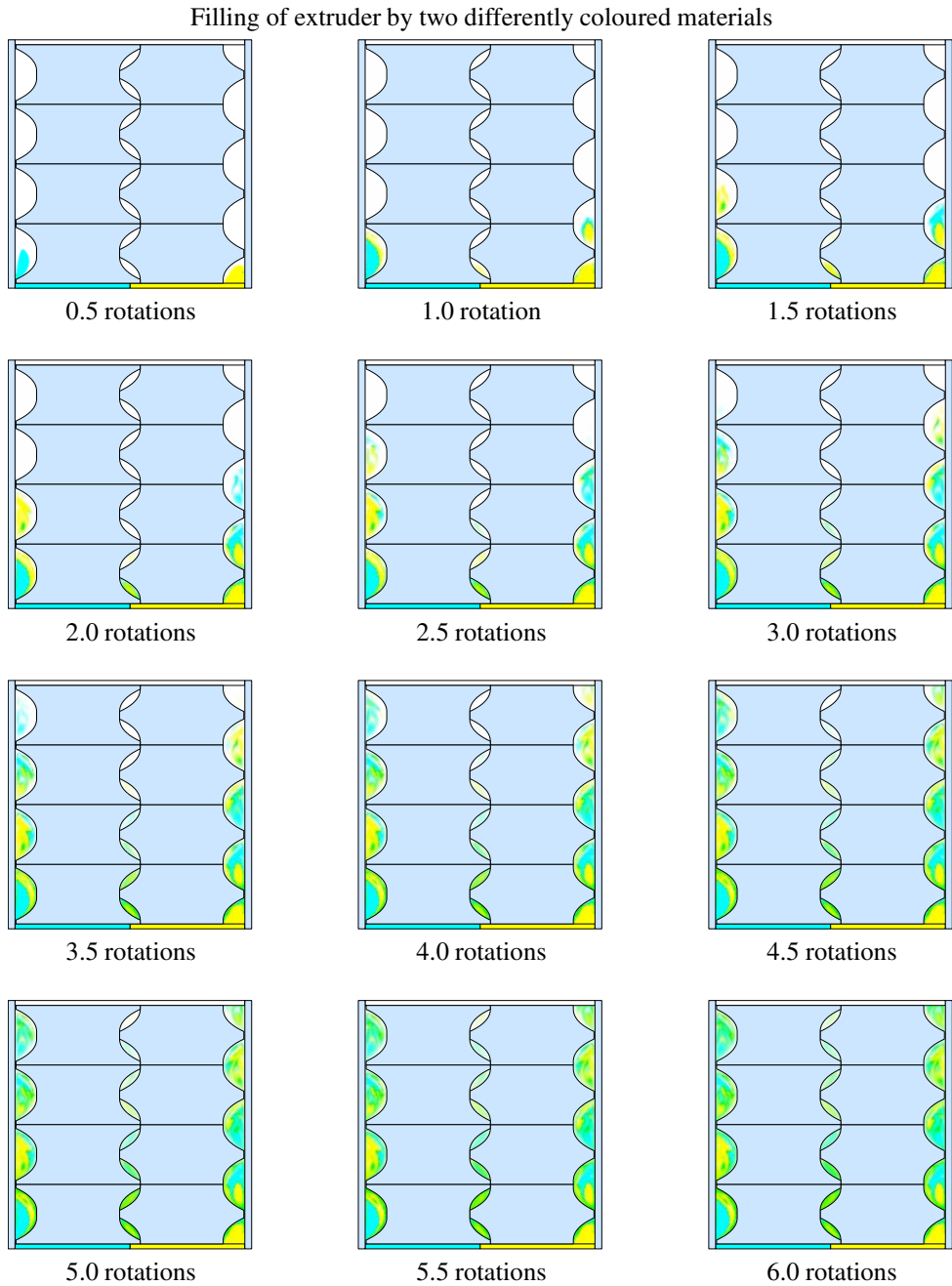


Fig. 5.13: Concentration distribution in the transport section of a twin screw extruder. The figures illustrate the ‘filling’ of the extruder.

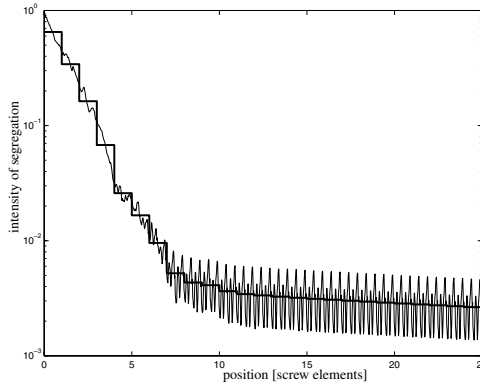


Fig. 5.14: Intensity of segregation along the extruder. The thin line indicates the intensity of segregation per layer of subdomains; the thick line indicates the intensity of segregation per screw element.

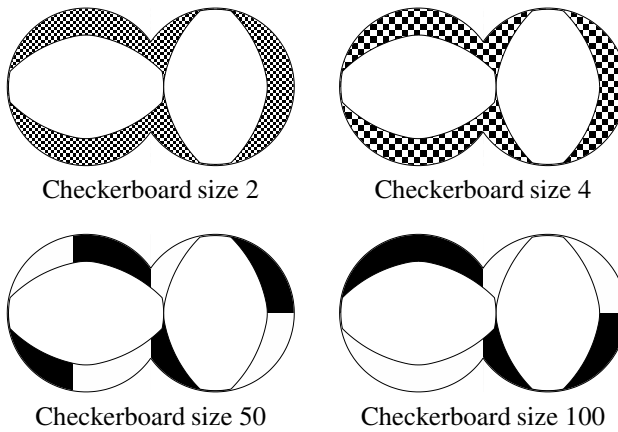


Fig. 5.15: Different checkerboard sizes used for dependence of mixing quality on initial concentration distribution.

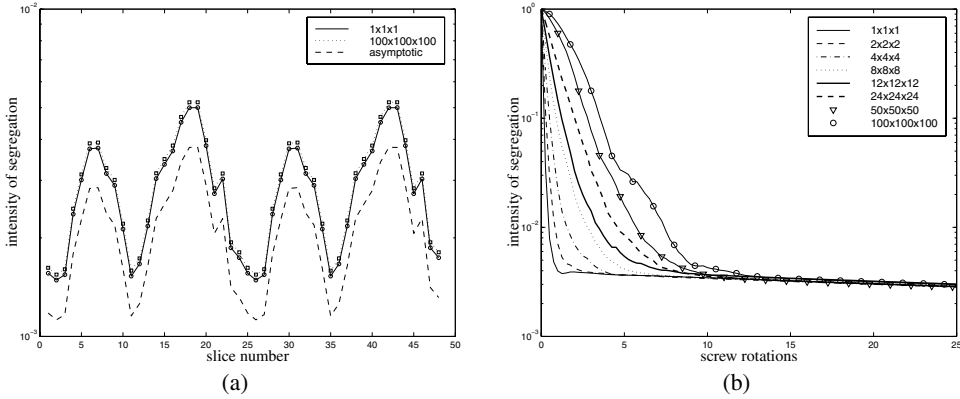


Fig. 5.16: a) Intensity of segregation per slice of an extruder element for two different checkerboard sizes after 25 screw rotations, the dashed line (asymptotic) results from 200 mapping steps with an ideal initial concentration distribution ($C = \frac{1}{2}$ for all subdomains); b) Evolution of the intensity of segregation for differently sized initial checkerboard clusters.

should stay equal to zero. However, due to errors in the coefficients of the mapping matrix caused by volume conservation errors, fluid gets ‘demixed’ and the average concentration in a subdomain starts to differ from the initial average concentration. These errors result in under- or overfilled subdomains, hence the deviation from the average initial concentration. These deviations influence the local concentration and, therefore, the intensity of segregation.

Figure 5.16b shows the evolution of the intensity of segregation, determined over the entire element, for a number of initial concentration distributions. The intensity of segregation decreases fastest for the initial checkerboard pattern with cluster size 1. The rate of decrease diminishes with increasing initial cluster size. This behaviour is expected. The size 1 checkerboard pattern represents an almost ideally premixed mixture. After only a few rotations, the mixture will be ideally mixed with regard to the subdomain size considered. For increasing cluster size, the system will be increasingly worse premixed. It therefore will take increasingly more screw rotations to reach the near horizontal plateau in figure 5.16b.

As already indicated, another important issue when dealing with extruders is the residence time distribution over a cross-section or at the exit, especially when reactive systems are considered or when degradation of the transported fluid is an issue. The residence time distribution is also computed using the mapping matrix. First the domains in element 1 are identified that have passed the entrance of the element. From these subdomains the average residence time \bar{t} is computed and stored in an average residence time column. Now the average residence time for subdomain i can be computed by:

$$\bar{t}_i = \sum_j \Phi_{ij} (\bar{t}_j + \Delta t) \quad (5.8)$$

where Δt is the elapsed (physical) time per mapping operation and Φ_{ij} the mapping coefficient describing the volume contribution from subdomain j to subdomain i . The residence time t is made dimensionless by scaling with the time needed for one full revolution of the screws: $t' = t/(2\pi\omega)$.

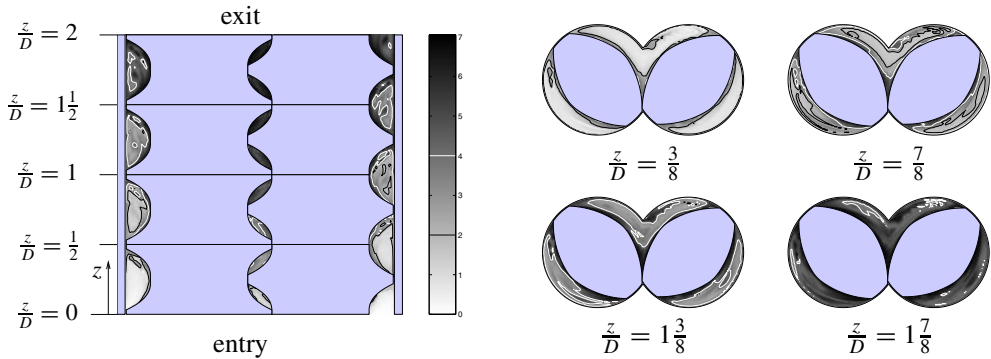


Fig. 5.17: Dimensionless residence time (screw rotations) in the transport part of a twin screw extruder. The drawn white and black lines correspond with a dimensionless residence time of 2 and 4, respectively.

For the transport elements the average (dimensionless) time distribution is shown in figure 5.17. It is obvious that large differences occur in a cross-section. Although the screws are supposed to be self-wiping, the largest residence times are on the screws. This is caused by the fact that screws are ‘wiped’ only once each rotation by a point contact while, with a two-lobe screw, the walls are wiped twice per rotation by a line contact.

A conventional way to measure residence time distribution is to add tracers (of e.g. TiO_2) during a short period to the extruder, a so-called *pulse-feed*. At the exit samples of polymer are collected and the amount of TiO_2 is measured. Using the mapping method, a similar simulation is performed with the four screw element. Tracer material is injected into the screw during one rotation. Each mapping step, the amount of tracer material found in the exit element (element 5) is summed and plotted. The result is shown in figure 5.18a. The cumulative output is shown in figure 5.18b. Due to computational errors (both in the computation of the velocity field as well as errors in determination of the coefficients for the mapping matrix), 5% of the fluid was ‘lost’. The results in figure 5.18 are scaled on the amount of fluid in the screw plus the total amount of fluid that has already exited. The first tracer material exits the extruder after four rotations (as may be expected since four elements are regarded). A large amount (66%) has already left the extruder after 6.5 rotations. However, 13 screw revolutions are needed to get 95% output and 19 screw revolutions to get 99.5% output.

5.7 Conclusions and discussion

It is shown that the mapping method is a suitable method for the analysis of dynamic, periodic devices. It is capable of determining concentration distributions and corresponding mixing measures (like the intensity of segregation) as well as average residence time. Moreover, it has been shown how residence time distributions can be mapped and give expected results. Although only transport elements have been regarded up to now, it should be obvious that the method is not limited to the analysis of only one type of element: combinations of elements can be analysed as soon as mapping matrices for these elements are available. In that case not only the mapping matrix for that particular element needs to be computed, but also one for

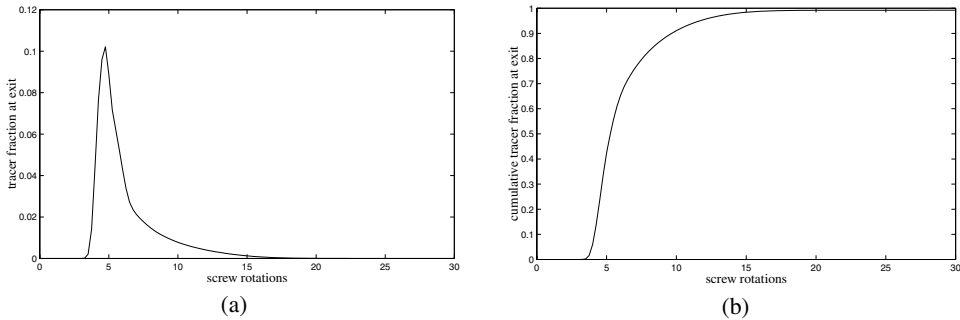


Fig. 5.18: a) Output and b) cumulative output (or residence time distribution) for a four element screw part.

a transition element (e.g. from transport to kneading) since in general the influence of these transitions on the velocity field will not be negligible.

Further, it has been shown that with the computation of a mapping matrix for only one transport element, a screw built of a number of those elements can be analysed. This shows that once a ‘building box’ of mapping matrices for various screw elements is computed, different screw arrangements can easily be analysed on overall mixing performance and residence time distribution. The mapping method allows one to analyse any order of screw elements. This implies that extra care has to be taken that the resulting screw arrangement is feasible (i.e. the pressure along the screw should not be negative). Therefore the mapping method has to be combined with an overall analysis like those shown by Meijer & Elemans (1988), Meijer & Elemans (1990), Elemans & Meijer (1990).

The oscillations that occur in the intensity of segregation plot (figure 5.14) result from volume conservation errors in the mapping matrix. In order to decrease these errors, the computation of the mapping matrix needs to be improved. Since the velocity field was computed using first order elements, improvement can be made by using higher order methods. This will also have a positive effect on the discretization of the curved boundaries Γ and γ .

Another improvement that can be made is to make the grid used to compute the mapping matrix more conforming to the geometry. In that case better subdivision is created since there will be less distorted elements. The determination of the intersection between tracked and initial subdomains will become more involving since boundaries of both domains can be curved.

The time-periodic approach followed in this chapter gives an indication of concentration and residence time distribution along the entire part of the screw section modelled. However, it does this only for fixed orientations of the screws, and does not give a time average of concentration or residence time distribution in a cross-section of the screw. As noted earlier, this is not a source of grave errors if one considers that the residence time distribution per slice will not differ greatly. For the time periodic approach the entire screw needs to be modelled. As a result concentration and residence time distribution are known for the entire screw. The space-periodic approach would map cross-section to cross-section, thereby reducing the mapping operation by the simpler matrix-vector multiplication used in the previous chapters instead of the one shown in figure 5.10. The space-periodic approach will also give a better

average of concentration and residence time distribution in cross-sections of the extruder. A further advantage is that the space-periodic approach resembles the actual assembly of a pair of extruder screws; as a screw is assembled from metering zone to exit, so can the mapping order be assembled and the influence of a particular element or combination of elements on properties of the mixture can be evaluated instantaneously.

An obvious disadvantage of the space-periodic approach is that the deforming subdomains are not volume conserving, which complicates error estimation. Another drawback of the space-periodic approach is that mapping other quantities, as e.g. morphology by using the area tensor (see [Wetzel & Tucker \(1997\)](#); this thesis chapter 2.6), becomes more complicated due to differences in ‘tracked’ time.

Chapter 6

Conclusions and Recommendations

6.1 *Conclusions*

The mapping method presented in this thesis has proven to be a useful tool to analyse mixing behaviour in different geometries. It is based on subdividing the flow domain in a large number of subdomains. The boundaries of these subdomains are tracked for a period of time or space. The tracked subdomains are compared with the initial subdomains, and a mapping or transport matrix is compiled that indicates how much fluid from one subdomain is advected to another subdomain. The evolution of, for example, concentration distribution now has been simplified to straightforward matrix-vector multiplications. During tracking also other quantities relevant for mixing can be computed as for example residence time, exerted shear and elongation. This facilitates tracking structure development via for instance the use of the area tensor.

The computation of the mapping matrix (or a set of matrices) is relatively expensive. However, once a mapping matrix is compiled it can be used to investigate the flow under consideration with added flexibility: changes in mixing protocol do not require new computation of the mapping matrix but simply change the number and sequence of mapping operations and manipulation of the elements in the column.

Using a set of mapping matrices it has been shown that concentration distributions for a number of geometries can easily be obtained. Applying mixing measures to these concentration distributions, the quality of the mixture can be quantified. This quantification allows for automated comparison between different concentration distributions, and, therefore, can be used to optimize mixing protocols. The mapping method is essential in this case, because the computation of concentration distribution is fast. Conventional methods as for example the Poincaré method would need a more extensive recalculation.

With respect to conventional methods, the mapping method has the advantage that it describes the transport of actual amounts of fluid, whereas some of the conventional methods describe the transport of particles. These particles have no physical size and therefore can give only an indication of how fluid spreads through a domain. Especially in the case where chaotic advection is involved, the results of these methods with respect to the actual presence of fluid are open for discussion.

Mapping can only be applied to mixing flows where the mixing itself does not influence the rheology of the flow, since changes in rheology will change the velocity and therefore the mapping matrix. However, mapping is not restricted to Newtonian fluids. Also more complex, non-Newtonian, fluids can be analysed. In this case a mapping matrix needs to be computed that describes the transition from inflow to fully developed flow, much like in the

case of different twin screw extruder elements, where a mapping matrix needs to be computed for each transition from one type of element to another type of element.

The accuracy of the mapping matrix is determined by the accuracy of the computed velocity field, the accuracy of the tracking routines, as well as the accuracy of the boundary description of the tracked subdomain. The accuracy of the mapping operations are further determined by the size of the subdomains and the number of mapping operations performed. It therefore may be advantageous to compute a set of mapping matrices that describe the same type of motion, but span different intervals (in time or space). This will reduce the diffusion by mapping for a particular examined interval, since less mapping operations need to be made.

Although in this thesis primarily concentration and residence time are mapped, it should be repeated that these are not the only quantities that can be mapped. Other quantities, as e.g. the area tensor, which is related to interfacial area, can be mapped as shown in chapter 2.

The flexibility of the mapping method and the speed of the mapping operations make it a useful tool to investigate the efficiency of mixing flows. The mapping method can be used to create efficiency diagrams that indicate for what set of parameters mixing will be inefficient and for what set it will be efficient. These plots also indicate what the effect of small changes in process parameters will be on the mixture.

6.2 Recommendations

In order to make effective use of the mapping method, the result of a set of mapping operations should ideally be one number that indicates the property of interest of the resulting mixture. In this thesis the intensity of segregation has been chosen as mixture quality indicator. However, the quality of a mixture can depend on different properties of the mixture. In case of intensity of segregation, the deviation of the mean concentration of all subdomains in the flow domain is regarded. However, one might not only be interested in this deviation, but also in the number and size of islands that have a deviation larger than a certain maximum. In this case other mixing measures need to be applied, such as scale of segregation. It will be useful when mixing measures are further studied if, at the same time, it can be indicated what property of the mixture they describe. It is impossible to derive a single mixing measure that describes a mixture in a sense that all important properties are designated. Depending on the particular application, one or more mixing measures need to be chosen and evaluated. These mixing measures should be charted and implemented into the mapping method.

As mentioned in the previous section, it is possible to map other quantities than concentration and average residence time. Especially morphology is an interesting property. Morphology can be mapped using the area tensor, as has been shown by Galaktionov *et al.* (2000a). Since the area tensor in principle can describe morphology in three dimensions, it can (and should) also be used when industrial mixers are regarded.

The most expensive part of the mapping method is the determination of the mapping matrix. This is mainly caused by the extensive boundary tracking involved to determine the coefficients in the mapping matrix. This part is easily parallelized, and, since all tracking computations are independent of each other, parallel computation scales extremely well with the number of processors. Nevertheless, computations in complex geometries still use huge amounts of computer time. This may be improved by using more efficient tracking and

interpolation algorithms.

The origin of the oscillations in the intensity of segregation for the twin screw extruder transport element are caused by errors in the velocity field computed by a first order fictitious domain method. Therefore the accuracy of the velocity field needs to be improved. This can be done by increasing the order of the finite elements used, or by using high order spectral elements. Spectral elements are preferred, however, fictitious domain methods combined with spectral elements have not been reported yet. Other methods, like the pseudo concentration method, may need to be applied. Most ideal from a computational point of view would be to only mesh the actual fluid domain, however, creating the meshes needed in this case is far from trivial (see e.g. [van Rens, 1999](#)).

Also, the subdomain division for the determination of the mapping matrix may be improved. Currently, the subdomain division is rectangular. In case of curved geometries, an adapted subdomain boundary, more conforming to the shape of the mixer, may be used to create a better subdivision: less distorted elements or subdomains with a very small volume relative to other subdomains. However, the determination of the intersection of tracked and initial subdomains becomes more expensive since the intersection with curved surfaces needs to be computed.

Since a number of industrial mixers can be regarded in a time-periodic as well as a space-periodic manner, it should be investigated in more detail what the advantages and disadvantages of both manners are. The time-periodic approach for the twin screw extruder imposes that the entire fluid domain needs to be subdivided into subdomains. A space-periodic approach would in this case map from cross-section to cross-section, reducing the total number of subdomains that need to be mapped. The space-periodic approach also is more flexible, since the screw geometry can be adapted from one map to the next, whereas with a time-periodic approach, first an entire screw needs to be assembled. Disadvantages of a space-periodic approach are that interpretation of data becomes less trivial since not all subdomains will cross a cross-section at the same time, and, since the domain is constantly changing, the shape of the tracked subdomains will be difficult to interpret. Mapping of quantities other than concentration and residence time, may also become more involved.

Appendix A

Mixing measures

To quantitatively compare mixing protocols, mixing measures need to be defined. Relevant mixing measures are usually functions of moments of the concentration distribution. Here, the intensity of segregation I and the scale of segregation S are chosen.

Intensity of Segregation

The intensity of segregation is a second moment statistic (variance) of the concentration distribution. It can be calculated as follows: first define the averaging operator $\langle f(\mathbf{x}) \rangle_{\Omega}$ over the domain Ω as:

$$\langle f(\mathbf{x}) \rangle_{\Omega} = \frac{\int_{\Omega} f(\mathbf{x}) dA}{\int_{\Omega} dA}. \quad (\text{A.1})$$

Intensity of segregation is a measure of the deviation of the local concentration from the ideal situation (i.e. when the mixture is homogeneous). The intensity of segregation is defined as, [Danckwerts \(1952\)](#):

$$I = \frac{\sigma_c^2}{\bar{c}(1 - \bar{c})} \quad \text{with} \quad \bar{c} = \langle c(\mathbf{x}) \rangle_{\Omega}, \quad (\text{A.2})$$

where σ_c^2 is the variance in concentration over the entire domain Ω :

$$\sigma_c^2 = \langle (c(\mathbf{x}) - \bar{c})^2 \rangle_{\Omega}, \quad (\text{A.3})$$

and $c(\mathbf{x})$ is the concentration in a point \mathbf{x} in the domain.

When no diffusion is assumed, $c(\mathbf{x})$ will either be 1 or 0. Therefore I will always be equal to 1, independent of the distribution. To avoid this situation, the *coarse grain density* C_i ([Welander, 1955](#)) on a finite subdomain Ω_i is defined:

$$C_i = \langle c(\mathbf{x}) \rangle_{\Omega_i}. \quad (\text{A.4})$$

Coarse grain density can take values between, and including, 0 and 1. The domains Ω_i are chosen identical to the domains in the discretization for the mapping method. Equation (A.2) can be rewritten in a discrete form using equation (A.4) as:

$$I_d = \frac{1}{A_{\Omega}} \sum_{i=1}^N \frac{(C_i - \bar{C})^2}{\bar{C}(1 - \bar{C})} A_{\Omega_i} \quad \text{with} \quad \bar{C} = \bar{c}, \quad (\text{A.5})$$

in which A_{Ω} and A_{Ω_i} represent the area of the flow domain and a subdomain, respectively, and N is the number of subdomains. Using this definition, the intensity of segregation (or

sample variance) changes when a mixing protocol is applied. The top limiting value (worst case) for I_d is 1 when all Ω_i have a coarse grain density of either one of two discrete values (the boundary of the dyed area is coinciding with the boundaries of the subdomains). In the ideal case $I_d = 0$ since $C_i = \bar{c}$ in all Ω_i . Note that I_d depends on the size of the domains Ω_i . This means that the subdomain size should be chosen according to the level of interest; if striations in the mixture of a certain size are critical for the mixture and thus must be visualized, the subdomain size should be chosen accordingly.

For three-dimensional analysis, the definition for the discrete intensity of segregation I_d is adapted to:

$$I_d = \frac{1}{\bar{c}(1-\bar{c})} \frac{1}{V} \sum_{i=1}^N (c_i - \bar{c})^2 v_i, \quad (\text{A.6})$$

and the average concentration \bar{c} is:

$$\bar{c} = \frac{1}{V} \sum_{i=1}^N c_i v_i, \quad (\text{A.7})$$

where c_i is the concentration of marker fluid in subdomain i and v_i is the volume of that subdomain. The volume V is:

$$V = \sum_{i=1}^N v_i. \quad (\text{A.8})$$

If all subdomains have the same volume v_i this simplifies to:

$$I_d = \frac{1}{\bar{c}(1-\bar{c})} \frac{1}{N} \sum_{i=1}^N (c_i - \bar{c})^2, \quad \text{with} \quad \bar{c} = \frac{1}{N} \sum_{i=1}^N c_i. \quad (\text{A.9})$$

Scale of Segregation

The scale of segregation is another second moment statistic of the concentration distribution. This measure indicates whether large unmixed regions in the mixture are present and whether a periodicity in the concentration distribution exists. The scale of segregation was defined by [Danckwerts \(1952\)](#) as a functional of the correlation function:

$$S = \int_0^\infty \int_0^\infty \rho(\mathbf{r}) d\mathbf{r}, \quad (\text{A.10})$$

with the correlation function $\rho(\mathbf{r})$:

$$\rho(\mathbf{r}) = \frac{\langle (c(\mathbf{x}) - \bar{c})(c(\mathbf{x} + \mathbf{r}) - \bar{c}) \rangle_\Omega}{\sigma_c^2} \quad \text{with:} \quad \mathbf{r} = \Delta \mathbf{x}. \quad (\text{A.11})$$

This indicates that $\rho(\mathbf{0}) = 1$ since numerator and denominator then are equal. The correlation function can be regarded as the auto-convolution of $(c(\mathbf{x}) - \bar{c})$. The correlation function $\rho(\mathbf{r})$ can have any value from 0 to 1, unless some form of long-range segregation

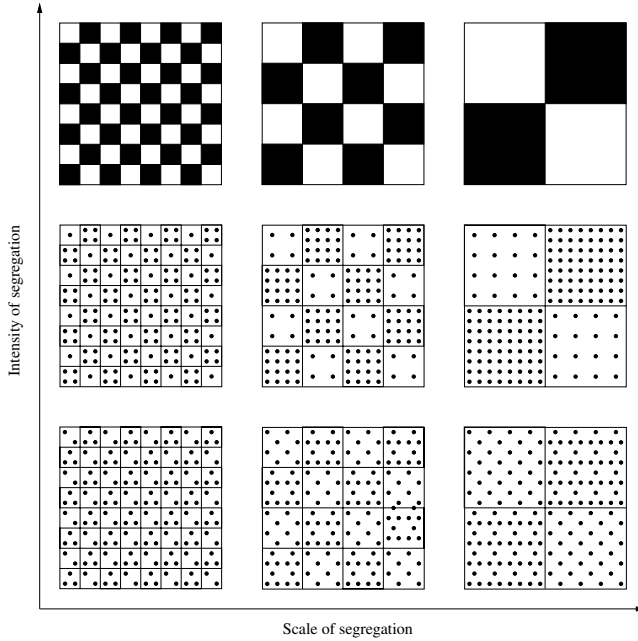


Fig. A.1: Difference between scale of segregation S and intensity of segregation I (cf. [Mohr et al., 1957](#)).

(periodicity) in the mixture is present. In that case $\rho(\mathbf{r})$ can range from -1 to 1 . This indicates that S according to (A.10) can be small, although the mixture is bad. In the paper of [Danckwerts \(1952\)](#), it was assumed that this long range periodicity is not present. When diffusive mixtures ($0 \leq c \leq 1$) are studied, the ideal situation is reached when $C(\mathbf{x}) = \bar{C} \forall \mathbf{x} \in \Omega$. Then the correlation function will be equal to 0 in its entire domain. Consequently, the best possible diffuse mixture in the sense of scale of segregation occurs when $S = 1 \wedge I = 0$.

When the concentration distribution is discretized similar as for the determination of the discrete intensity of segregation, the correlation function is easiest computed via a two-dimensional fast Fourier transform ([Tucker, 1991](#)).

The difference between scale and intensity of segregation is shown schematically in figure A.1. Scale of segregation gives an indication of large scale structures in the mixture. The size of the variations (in concentration) is not influencing the value for S , just the fact that there are variations. For the intensity of segregation the opposite is true; it does not matter how fluid is distributed, only the deviation of the average concentration influences the value of I .

Appendix B

Boundary and surface tracking

B.1 Adaptive boundary tracking in two dimensions

Since in chaotic flows the deformation of a boundary is not homogeneous a huge number of equidistant points would be needed to describe a chaotically stretched boundary reasonably. Still then, points would eventually be very closely spaced in one part of the boundary, and large gaps would fall between points on another part of the boundary. In order to circumvent this problem, a relatively small amount of markers (nodes) describing the circumference Γ of the marked area Ω is started with. During the course of tracking, nodes are inserted in between nodes where either the distance has grown beyond a certain limit, or when the angle formed by three consecutive nodes is smaller than a critical one, according to the following criteria (Galaktionov *et al.*, 2000b):

$$l < l_{1c} \quad , \quad A \tag{B.1}$$

$$l < l_{2c} \quad \text{if} \quad \alpha_i < \alpha_c \vee \alpha_{i-1} < \alpha_c \quad (l_{2c} < l_{1c}), \tag{B.2}$$

with:

$$l = \|\mathbf{x}_{i-1} - \mathbf{x}_i\|, \tag{B.3}$$

$$\alpha_i = \arccos \left(\frac{(\mathbf{x}_{i-1} - \mathbf{x}_i) \cdot (\mathbf{x}_{i+1} - \mathbf{x}_i)}{\|\mathbf{x}_{i-1} - \mathbf{x}_i\| \|\mathbf{x}_{i+1} - \mathbf{x}_i\|} \right), \tag{B.4}$$

where l is the distance between two adjacent nodes, α and α_c the angle and minimum angle between two adjacent edges and l_{1c} and l_{2c} the preset maximum lengths in straight and curved regions of the boundary, respectively. If conditions (B.1) and (B.2) are not satisfied, the edge between \mathbf{x}_{i-1} and \mathbf{x}_i is split into two parts and a new node is inserted. Nodes are inserted at an earlier configuration since, in particular in the neighbourhood of hyperbolic points, results can be drastically influenced by interpolation errors. The procedure is repeated for the newly created edges.

B.2 Adaptive boundary tracking in three dimensions

To accurately track the boundary (surface) of an arbitrary three-dimensional volume an adaptive scheme is required since the volume boundaries will become very distorted in efficient mixers. The internal representation of the surface description should therefore allow for easy addition of nodes, edges and triangles, as well as topological changes. Furthermore, the internal structure should be such that intersections with (arbitrary) planes or volumes can be obtained without reshuffling of data.

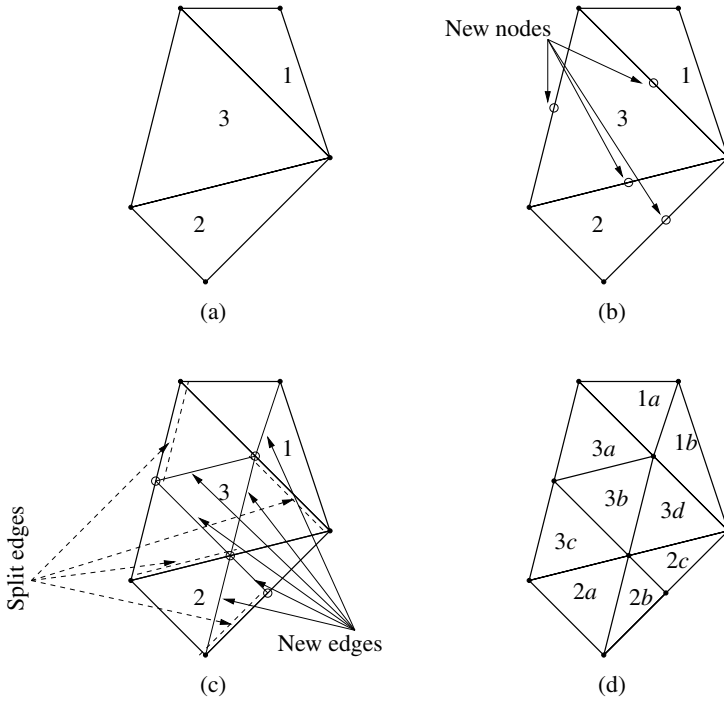


Fig. B.1: Three ways used to refine triangles (indicated by triangle 1, 2 and 3). (a) unrefined state; (b) new nodes are added in the centres of edges that are too long; (c) existing edges are split and new edges are created; (d) the refined mesh.

The surface description is created by triangulation. The internal bookkeeping is much like the AVS UCD (Unstructured Cell Data) structure (Advanced Visual Systems Inc., 1992): a list of points with their x , y and z coordinates, a list of edges connecting two points, and a list of triangles determined by edge numbers. This structure makes arbitrary refinement of the surface possible. Consider the three triangles in figure B.1a. First the length of all edges is computed and compared to a preset maximum length. If the length of an edge exceeds this maximum length, the edge is marked for splitting and a new point is added to list of coordinates (see figure B.1b). Then, the tagged edges are split into two pieces. A new edge (dashed lines) is added to the list of edges, and the original edge is updated. To refine the triangles, the number of edges marked for refinement on the triangles are regarded. In case of one marked edge, the triangle is refined by adding an edge from the new point to the opposite angle. In case of two marked edges, an edge is added between the two new nodes and one of the new nodes and its opposing angle. In case of three tagged edges, edges will only be added between the new nodes (see figure B.1c). Figure B.1d shows the refined results. When the deformation of the triangle is large, this process might need to be repeated a number of times. In highly curved regions, triangles are refined further. Curvature of the boundary is detected by computing the normals on two adjacent triangles. If the angle between the two normals is

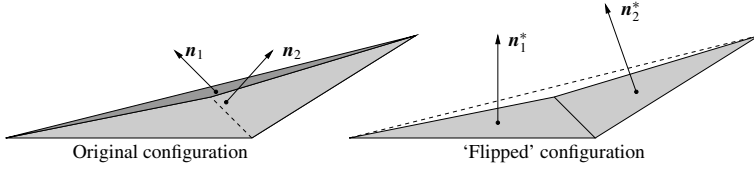


Fig. B.2: Improving triangle quality and reducing edge length by ‘flipping’ the common edge

larger than a maximum angle α_{max} , the maximum length of an edge of the regarded triangles is decreased.

Especially in shearing regions, triangles can get very extended and triangle quality deteriorates. Triangle quality Q_{Δ} is here defined as:

$$Q_{\Delta} = \frac{A_{\Delta} \cdot (S_{\Delta})^{-2}}{A_{\Delta, \text{perfect}} \cdot (S_{\Delta, \text{perfect}})^{-2}}, \quad (\text{B.5})$$

where A_{Δ} and S_{Δ} are the area and circumference of the triangle, respectively. The denominator represents the ratio of area over circumference for a perfect triangle ($\frac{1}{36}\sqrt{2}$) and is used to normalize the triangle quality. As long as two triangles with a common edge are (nearly) in the same plane, the quality of the triangle may be improved by ‘flipping’ (see figure B.2). The common edge is removed and is replaced by an edge that connects the two most blunt angles. Flipping is not just performed to acquire a ‘better shaped triangle’; the longest common edge of two triangles will be replaced by a shorter one, thus saving on tracking additional nodes that would otherwise have been introduced by refinement of the long edge. Although the flipping procedure improves the quality of the triangles and reduces the number of nodes to be tracked, it is obvious that it violates volume conservation of the entire structure, since locally the surface changes from convex to concave or vice versa. Therefore, flipping can only be applied when the normals n_1 and n_2 of the two triangles have (nearly) the same direction.

B.3 Determination of intersecting areas and volumes

For the mapping method it is crucial to determine the intersection of an arbitrary tracked volume with an (arbitrary) reference volume. In this work, however, only intersections of arbitrary volumes with volumes bounded by planes with constant x , y or z coordinates are computed. Figure B.3 shows the procedure of determining the intersecting area in two dimensions. Given the boundaries Γ_1 and Γ_2 of an undeformed and deformed subdomain boundary, first the intersections of the edges of Γ_1 with Γ_2 are determined. These extra nodes (indicated with \circ) are added to the description of Γ_2 . Then the nodes outside the domain enclosed by Γ_1 are projected onto it, and care is taken that no extra intersections are generated: if an edge crosses the extensions of the undeformed subdomain (indicated by the dash-dotted lines), it is projected to the nearest corner on the subdomain.

The area of the surface is then calculated by computing:

$$A = \frac{1}{2} \sum_{n=1}^N \sum_{i,j=1}^2 \varepsilon_{ij} x_i^{(n)} y_j^{(n)}. \quad (\text{B.6})$$

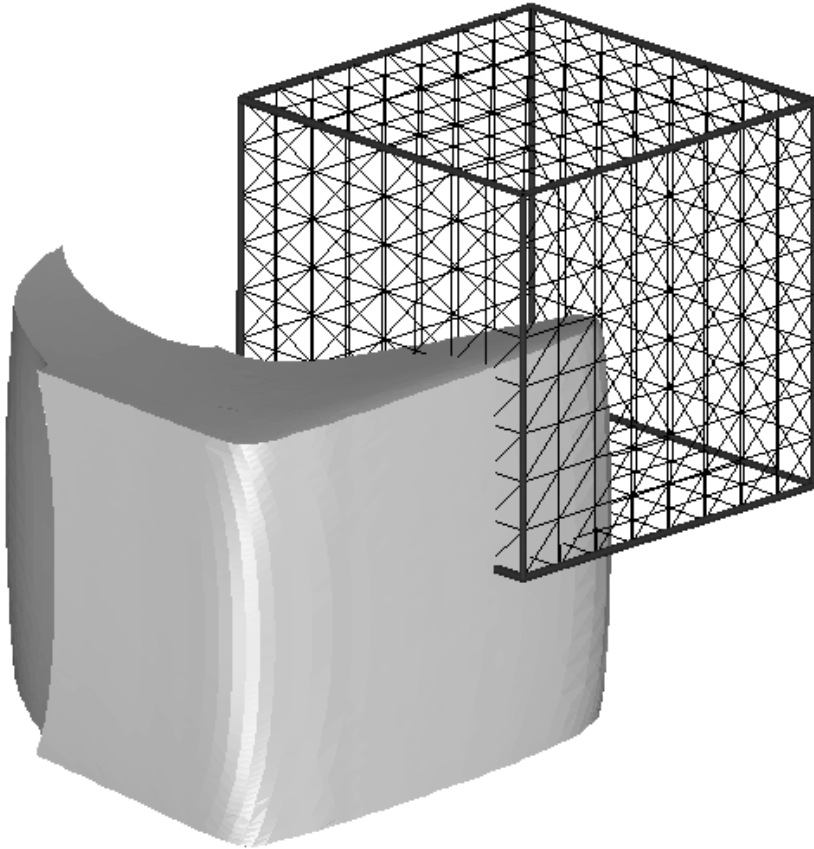


Fig. B.3: Determination of the area of intersection between an undeformed subdomain Γ_1 and a deformed subdomain Γ_2 . a) Domains Γ_1 and Γ_2 ; b) extra nodes added to Γ_2 indicated by \circ ; c) resulting domain Γ'_2 after projection of nodes outside the domain enclosed by Γ_1 .

where the first sum is the sum over all edges and the second sum is over the vertices of the corresponding edge. The components of ε_{ij} are defined as:

$$\varepsilon_{ij} = \begin{cases} 0 & \text{if } i = j \\ +1 & \text{if } i = 1 \wedge j = 2 \\ -1 & \text{if } i = 2 \wedge j = 1 \end{cases} . \quad (\text{B.7})$$

The procedure in three dimensions is similar to that in two dimensions. The surface grid is refined according to the extra nodes inserted; extra triangles are created in order to maintain integrity of the surface description. The surface that results is identical in shape, however, individual triangles do not cross the boundaries of the undeformed subdomain anymore. The nodes outside the undeformed subdomain are again projected onto it. The volume remaining is the intersection between the deformed and undeformed subdomain. For clockwise numbering (looking from the side of the outer normal), the volume enclosed by the surface that consists of triangles can be computed using simple formula:

$$V = -\frac{1}{6} \sum_{n=1}^N \sum_{i,j,k=1}^3 \varepsilon_{ijk} x_i^{(n)} y_j^{(n)} z_k^{(n)} . \quad (\text{B.8})$$

The first sum is over all N triangular elements of the surface, where $x_i^{(n)}$, $y_j^{(n)}$ and $z_k^{(n)}$ are the coordinates of the vertices numbered respectively i , j and k in subdomain number n . This formula assumes that the nodal points in each triangle are numbered clockwise, looking from the side of the outer normal to the surface. In equation (B.8) ε_{ijk} are the components of the Levi-Civita tensor defined as:

$$\varepsilon_{ijk} = \begin{cases} 0 & \text{if } i = j \vee j = k \vee i = k \\ +1 & \text{if } (i, j, k) \text{ is an even permutation of } (1, 2, 3) \\ -1 & \text{if } (i, j, k) \text{ is an odd permutation of } (1, 2, 3). \end{cases} \quad (\text{B.9})$$

Formula (B.8) is exact for a volume enclosed by a surface composed of triangles.

For more complex shape of the undeformed subdomains (other than brick-shaped) more complicated technique must be used (based on subdivision of the undeformed subdomain into set of tetrahedra and computing the intersection with each of them). For the rectangular subdomains, however, the described above technique is rather fast and reliable.

Before using the algorithm outlined above, the list of undeformed subdomains with possible intersections is formed (using coordinates of the nodal points of the deformed surface). This reduces the processor time necessary to compute the elements of the mapping matrix by a few orders of magnitude, since in the given example the average deformed subdomain intersects with less than 12 initial subdomains (out of 10^6 boxes used to discretize the flow domains in chapters 3 and 5 for mapping).

Appendix C

Area tensor

Laminar mixing of two liquids is generally performed to homogenize the mixture. Since a good mixing flows creates these desired very small droplets or striations, it is not possible to track these individual details. The area tensor (Wetzel & Tucker, 1997) describes the local morphology of a mixture in terms of size, shape and orientation of one fluid in another. It tracks the amount and orientation of the interface between the two liquids.

If a small averaging volume V with interfacial area Γ is considered, the (second order) area tensor is defined as:

$$\mathbf{A} = \frac{1}{V} \int_{\Gamma} \mathbf{n} \mathbf{n} d\Gamma \quad (\text{C.1})$$

with \mathbf{n} a unit normal vector on the interface Γ . The components of \mathbf{A} have units of interfacial area per volume in three dimensions and units of interfacial length per area in two dimensions. The trace of the area tensor ($\text{tr}\mathbf{A}$) is equal to the total interfacial area S_V in the averaging volume.

For passive mixing, $d\Gamma$ deforms affinely with the material. The evolution of \mathbf{A} can then be written as:

$$\dot{\mathbf{A}} = -\mathbf{L}^T \cdot \mathbf{A} - \mathbf{A} \cdot \mathbf{L} + \mathbf{L} : \mathcal{A} \quad (\text{C.2})$$

where the dot represents a material derivative, \mathbf{L} the velocity gradient tensor and \mathcal{A} is the fourth order area tensor, which is defined as:

$$\mathcal{A} = \frac{1}{V} \int_{\Gamma} \mathbf{n} \mathbf{n} \mathbf{n} \mathbf{n} d\Gamma. \quad (\text{C.3})$$

This fourth order area tensor is not calculated explicitly, but is approximated by a closure approximation. Two such closures are given by Wetzel & Tucker (1999a).

In mapping, time steps are generally large. Thus, the differential equation C.2 is not suitable. The deformation between the initial subdomain Ω_i^0 and the deformed subdomain Ω_i can be described by the deformation gradient tensor:

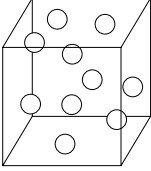
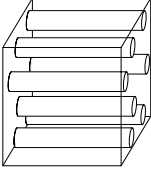
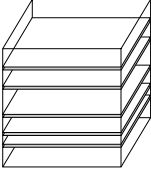
$$\mathbf{F} = \frac{\partial \mathbf{x}}{\partial \mathbf{x}^0}, \quad (\text{C.4})$$

where \mathbf{x}^0 are material coordinates associated with the spatial coordinates \mathbf{x} in the reference configuration. It is assumed that \mathbf{F} is uniform over Ω_i^0 .

If \mathbf{n}^0 is the unit normal vector to the interface $d\Gamma^0$ in the reference condition, then the transformations of \mathbf{n}^0 and $d\Gamma^0$ can be described as (Wetzel & Tucker (1999a), Wetzel & Tucker (1999b)):

$$\frac{d\Gamma}{d\Gamma^0} = \det \mathbf{F} \sqrt{(\mathbf{F}^T \cdot \mathbf{F})^{-1} : \mathbf{n}^0 \mathbf{n}^0}, \quad (\text{C.5})$$

Tab. C.1: Three microstructures and corresponding area tensors

	Geometry	\mathbf{A}
Spherical		$S_V \begin{bmatrix} \frac{1}{3} & 0 & 0 \\ 0 & \frac{1}{3} & 0 \\ 0 & 0 & \frac{1}{3} \end{bmatrix}$
Cylindrical		$S_V \begin{bmatrix} \frac{1}{2} & 0 & 0 \\ 0 & \frac{1}{2} & 0 \\ 0 & 0 & 0 \end{bmatrix}$
Lamellar		$S_V \begin{bmatrix} 1 & 0 & 0 \\ 0 & 0 & 0 \\ 0 & 0 & 0 \end{bmatrix}$

$$\mathbf{n} = \frac{(\mathbf{F}^{-1})^T \cdot \mathbf{n}^0}{\sqrt{(\mathbf{F}^T \cdot \mathbf{F})^{-1} : \mathbf{n}^0 \mathbf{n}^0}}. \quad (\text{C.6})$$

Substituting these into equation (C.1) gives

$$\mathbf{A} = (\det \mathbf{F}) (\mathbf{F}^{-1})^T \cdot \left(\frac{1}{V} \int_{\Gamma} \frac{\mathbf{n}^0 \mathbf{n}^0}{\sqrt{(\mathbf{F}^T \cdot \mathbf{F})^{-1} : \mathbf{n}^0 \mathbf{n}^0}} d\Gamma^0 \right) \cdot \mathbf{F}^{-1}. \quad (\text{C.7})$$

The right-hand side of this equation cannot be manipulated to contain only \mathbf{F} and the area tensor in the reference state \mathbf{A}^0 , hence there is no universal relationship of the type we seek. Instead, some approximation is essential.

The approximation used is based on the same idea as the rational ellipsoidal closure (Wetzel & Tucker, 1999a): to any area tensor \mathbf{A} and second-phase volume fraction ϕ , there corresponds a unique set of identical ellipsoidal droplets. The size, shape and orientation of the droplets can be characterized by a droplet shape tensor \mathbf{G} (Wetzel & Tucker, 1999b). This is defined such that, if the centre of the droplet is at the origin, points on the droplet surface satisfy the equation

$$\mathbf{x} \cdot \mathbf{G} \cdot \mathbf{x} = 1. \quad (\text{C.8})$$

To obtain the transformation law for \mathbf{G} under finite strain we first note that in the reference

configuration the points on the droplet surface satisfy

$$\mathbf{x}^0 \cdot \mathbf{G}^0 \cdot \mathbf{x}^0 = 1. \quad (\text{C.9})$$

Using equation (C.4) to replace \mathbf{x}^0 by \mathbf{x} , we have, in the deformed configuration,

$$\mathbf{x} \cdot \left((\mathbf{F}^{-1})^T \cdot \mathbf{G}^0 \cdot \mathbf{F}^{-1} \right) \cdot \mathbf{x} = 1. \quad (\text{C.10})$$

Comparing this to equation (C.8) we see that the term in parentheses equals \mathbf{G} , so the finite-strain transformation rule is simply

$$\mathbf{G} = (\mathbf{F}^{-1})^T \cdot \mathbf{G}^0 \cdot \mathbf{F}^{-1}. \quad (\text{C.11})$$

Our route for transforming the area tensor under finite strain is to convert the initial area tensor \mathbf{A}^0 to an equivalent droplet shape tensor \mathbf{G}^0 , find \mathbf{G} in the deformed state using equation (C.11), and then transform \mathbf{G} back to find the deformed-state area tensor \mathbf{A} . As a notational convenience we write this transformation as

$$\mathbf{A} = \mathbf{A}^0 \otimes \mathbf{F}^{-1}. \quad (\text{C.12})$$

For the conversion between the area tensor \mathbf{A} and the droplet shape tensor \mathbf{G} , one is referred to Galaktionov *et al.* (2000a) or appendix D.

In the extended mapping method, the subdomain volume Ω_i serves as the averaging volume for the area tensor. For subdomain i the associated area tensor is

$$\mathbf{A}_i = \frac{1}{\Omega_i} \int_{\Gamma_i} \mathbf{n} \mathbf{n} \, d\Gamma. \quad (\text{C.13})$$

Here Γ_i is the interfacial surface lying within Ω_i . Because Ω_i is explicitly chosen and has finite volume, the subdomain area tensor \mathbf{A}_i is a coarse-grain variable, like C_i .

For each non-zero entry Φ_{ij} in the mapping matrix, we compute an inverse deformation gradient tensor \mathbf{F}_{ij}^{-1} . This is evaluated at the centroid of $\Omega_j|_{t_{k+1}} \cap \Omega_i|_{t_k}$, the intersection between the deformed subdomain j and the undeformed subdomain i . This computation is carried out off-line, at the same time the mapping matrix Φ is being computed, and the results are stored for later use.

The extended mapping method updates the area tensor at each time step according to

$$\mathbf{A}_i^{k+1} = \sum_{j=1}^N \Phi_{ij} \left(\mathbf{A}_j^k \otimes \mathbf{F}_{ij}^{-1} \right). \quad (\text{C.14})$$

That is, the area tensor in any subdomain at time $k + 1$ is the sum of contributions from all donor subdomains, after the donor tensors from time k have been transformed by the appropriate deformation gradients. Equations (C.14) and (2.7) constitute one step of the extended mapping method.

The extended mapping method takes advantage of a key characteristic of the area tensor: it is additive. More precisely, if a domain Ω is the union of two non-overlapping subdomains Ω_1 and Ω_2 , and if the area tensors associated with the subdomains are \mathbf{A}_1 and \mathbf{A}_2 , then the

area tensor for the whole domain is

$$\begin{aligned}
 \mathbf{A} &= \frac{1}{\Omega} \int_{\Gamma} \mathbf{nn} \, d\Gamma \\
 &= \frac{1}{\Omega_1 + \Omega_2} \left[\int_{\Gamma_1} \mathbf{nn} \, d\Gamma_1 + \int_{\Gamma_2} \mathbf{nn} \, d\Gamma_2 \right] \\
 &= \left(\frac{\Omega_1}{\Omega_1 + \Omega_2} \right) \mathbf{A}_1 + \left(\frac{\Omega_2}{\Omega_1 + \Omega_2} \right) \mathbf{A}_2.
 \end{aligned} \tag{C.15}$$

That is, the area tensor for any domain is the sum of the area tensors its subdomains, weighted by the fraction of volume they occupy. This property of the area tensor allows us to sum the contributions from the donor subdomains in equation (C.14). Other microstructural descriptors, such as the droplet shape tensor \mathbf{G} , do not have this additive property, and cannot be used in the same way.

Appendix D

Converting between area tensors and droplet shape tensors*

To transform the area tensor under finite strain, we must convert from the area tensor to the shape tensor for equivalent ellipsoidal droplets, and back again. This appendix shows the details of that conversion.

With the area tensor, the length scale of the microstructure is determined by the trace of the tensor, which equals the interfacial area per unit volume S_V . The ‘shape’ of the tensor is described by the normalized area tensor \hat{A} , defined as

$$\hat{A} \equiv \frac{\mathbf{A}}{S_V}. \quad (\text{D.1})$$

The droplet shape tensor \mathbf{G} , defined in equation (C.8), describes the shape and size of identical ellipsoidal droplets. Initially we choose coordinate axes that coincide with the symmetry axes of the ellipsoid. These are the eigenvectors of the tensor \mathbf{G} . Let the semi-axes of the droplet be a , b , and c , with $a \geq b \geq c$. We number the axes so that the droplet shape tensor is

$$\mathbf{G} = \begin{bmatrix} 1/c^2 & 0 & 0 \\ 0 & 1/b^2 & 0 \\ 0 & 0 & 1/a^2 \end{bmatrix}. \quad (\text{D.2})$$

The shape of the droplet is described by the two axis ratios

$$C = \frac{c}{a} \quad D = \frac{c}{b}. \quad (\text{D.3})$$

Note that both C and $D \in [0, 1]$. Once C and D are known, the droplet size is determined by specifying c .

One can establish the correspondence between \mathbf{A} and \mathbf{G} for ellipsoidal droplets by evaluating the integral in equation (C.1) over the surface of an ellipsoid. The two tensors are coaxial, so if the shape tensor is diagonal as in equation (D.2), the area tensor will also be diagonal.

The normalized area tensor \hat{A} depends only on the axis ratios C and D , and the exact relationships have been derived by [Wetzel & Tucker \(1999a\)](#) and [Wetzel & Tucker \(1999b\)](#).

* This appendix is only enclosed for completeness. It is identical to Appendix C of *A Global, Multi-Scale Simulation of Laminar Fluid Mixing: The Extended Mapping Method*, O. S. GALAKTIONOV, P. D. ANDERSON, G. W. M. PETERS AND C. L. TUCKER, submitted to *International Journal of Multiphase Flow* and temporarily available from <http://polypro.me.uiuc.edu/online.html>

They are

$$\hat{A}_{11} = \frac{1}{1 - D^2} \frac{E(\theta, k) - D^2 F(\theta, k)}{(1 - C^2)E(\theta, k) + C^2 F(\theta, k) + CD\sqrt{1 - C^2}}, \quad (\text{D.4})$$

$$\hat{A}_{22} = \frac{D^2}{D^2 - C^2} \frac{\frac{D^2 - C^2}{1 - D^2} F(\theta, k) - D^2 \frac{1 - C^2}{1 - D^2} E(\theta, k) + CD\sqrt{1 - C^2}}{(1 - C^2)E(\theta, k) + C^2 F(\theta, k) + CD\sqrt{1 - C^2}}, \quad (\text{D.5})$$

$$\hat{A}_{33} = \frac{C^2}{D^2 - C^2} \frac{C^2 E(\theta, k) + (D^2 - C^2) F(\theta, k) - CD\sqrt{1 - C^2}}{(1 - C^2)E(\theta, k) + C^2 F(\theta, k) + CD\sqrt{1 - C^2}}, \quad (\text{D.6})$$

where $F(\theta, k)$ and $E(\theta, k)$ are the Legendre elliptic integrals of the first and second kind, respectively ([Gradshteyn & Ryzhik, 1994](#)), and k and θ are

$$k = \sqrt{\frac{1 - D^2}{1 - C^2}} \quad \theta = \cos^{-1}(C). \quad (\text{D.7})$$

These exact relationships cannot be inverted analytically, and an iterative numerical procedure is required. As an alternative, [Wetzel & Tucker \(1999a\)](#) found that these relationships are well approximated by

$$C \cong \left(\frac{\hat{A}_{33}}{\hat{A}_{11}} \right)^\alpha \quad D \cong \left(\frac{\hat{A}_{22}}{\hat{A}_{11}} \right)^\alpha, \quad (\text{D.8})$$

with $\alpha = 0.5977$. The semi-axis ratio values from this approximation are exact for the limiting cases of uniaxial, biaxial, and isotropic tensors, and they fall within 0.04 of the exact values for all other ellipsoidal shapes. Equations (D.8) can be inverted analytically, to give

$$\hat{A}_{11} \cong \frac{1}{\left(\frac{c}{a}\right)^{1/\alpha} + \left(\frac{c}{b}\right)^{1/\alpha} + \left(\frac{c}{c}\right)^{1/\alpha}} = \frac{1}{(C)^{1/\alpha} + (D)^{1/\alpha} + 1}, \quad (\text{D.9})$$

$$\hat{A}_{22} \cong \frac{1}{\left(\frac{b}{a}\right)^{1/\alpha} + \left(\frac{b}{b}\right)^{1/\alpha} + \left(\frac{b}{c}\right)^{1/\alpha}} = \frac{1}{\left(\frac{C}{D}\right)^{1/\alpha} + 1 + \left(\frac{1}{D}\right)^{1/\alpha}}, \quad (\text{D.10})$$

$$\hat{A}_{33} \cong \frac{1}{\left(\frac{a}{a}\right)^{1/\alpha} + \left(\frac{a}{b}\right)^{1/\alpha} + \left(\frac{a}{c}\right)^{1/\alpha}} = 1 - \hat{A}_{11} - \hat{A}_{22}. \quad (\text{D.11})$$

This is the form used for the calculations in this paper. By definition $\hat{A}_{11} + \hat{A}_{22} + \hat{A}_{33} = 1$, so there are only two independent eigenvalues of the normalized area tensor. Either equations (D.4)–(D.6) or equations (D.8)–(D.11) provide the mapping between the axis ratios C and D and these two components.

To complete the relationship, we must also relate the ‘sizes’ of the two tensors. This is determined from the surface area to volume ratio. The volume of the ellipsoid is

$$V_e = \frac{4}{3}\pi abc, \quad (\text{D.12})$$

while its exact surface area is

$$S_e = 2\pi c^2 \left(1 + \frac{\sqrt{1-C^2}}{CD} E(\theta, k) + \frac{C}{D\sqrt{1-C^2}} F(\theta, k) \right). \quad (\text{D.13})$$

A convenient approximation to the surface area that avoids the elliptic integral functions F and E is (Lehmer, 1950)

$$S_e \cong 4\pi ab \left(\frac{2}{5} \frac{C+D+1}{3} + \frac{3}{5} \sqrt{\frac{C^2+D^2+1}{3}} \right). \quad (\text{D.14})$$

If the ellipsoidal droplets occupy a fraction ϕ of the mixture volume, then their surface area per unit total volume is

$$S_V = \frac{\phi S_e}{V_e}. \quad (\text{D.15})$$

Substituting the exact area formula (D.13) and the volume (D.12), we find

$$S_V = \frac{3\phi c}{2ab} \left[1 + \frac{\sqrt{1-C^2}}{CD} E(\theta, k) + \frac{C}{D\sqrt{1-C^2}} F(\theta, k) \right]. \quad (\text{D.16})$$

For numerical calculations it is useful to rearrange this formula as

$$S_V = \frac{3\phi}{2c} \left[CD + \sqrt{1-C^2} E(\theta, k) + \frac{C^2}{\sqrt{1-C^2}} F(\theta, k) \right]. \quad (\text{D.17})$$

This handles the case where $a \rightarrow \infty$ and $C \rightarrow 0$ smoothly, and also has no problems if in addition $b \rightarrow \infty$ and $D \rightarrow 0$.

Alternately, one can use the approximate area formula (D.14), in which case

$$S_V \cong \frac{\phi}{c} \left[\frac{2}{5} (C+D+1) + \frac{3}{5} \sqrt{3(C^2+D^2+1)} \right]. \quad (\text{D.18})$$

In either case we have a direct relationship between S_V and c .

We now have all the pieces needed transform between the area tensor and the droplet shape tensor. To go from \mathbf{G} to \mathbf{A} the algorithm is:

1. Find the eigenvalues and eigenvectors of \mathbf{G} . The eigenvalues give a , b , and c according to equation (D.2). Normalize the eigenvectors and use them to form the rotation matrix \mathbf{R} between the principal axes and the laboratory axes. Compute C and D from equation (D.3).
2. Determine the principal components of the normalized area tensor $\hat{\mathbf{A}}$, using either the exact relations (D.4)–(D.6) or the approximate relations (D.9)–(D.11).
3. Determine S_V using either the exact formula (D.16) or the approximate formula (D.18).
4. Compute the area tensor in its principal coordinates using equation (D.1), i.e. $\mathbf{A} = S_V \hat{\mathbf{A}}$.

5. Use \mathbf{R} from the first step to rotate \mathbf{A} back to the laboratory axis system.

The reverse transformation, from \mathbf{A} to \mathbf{G} , follows a similar pattern. If the exact shape formulae (D.4)–(D.6) are used, then an iterative numerical procedure is required to find C and D . The approximate formulae can be used to provide a close initial guess, after which a Newton-Raphson iteration should converge without difficulty.

Bibliography

- ADVANCED VISUAL SYSTEMS INC. 1992 *AVS users guide*. Advanced Visual Systems Inc., 300 Fifth Ave., Waltham, MA 02154, USA. [B.2](#)
- ANDERSON, P. D. 1999 Computational analysis of distributive mixing. PhD thesis, Eindhoven University of Technology. [3.2](#), [4.2](#)
- ANDERSON, P. D., GALAKTIONOV, O. S., PETERS, G. W. M., VAN DE VOSSE, F. N. & MEIJER, H. E. H. 1999 Analysis of mixing in three-dimensional time-periodic cavity flows. *Journal of Fluid Mechanics* **386**, 149–166. [1.1](#), [1.2](#), [3.2](#)
- AREF, H. & EL NASCHIE, M. S. 1995 *Chaos applied to fluid mixing*. Oxford: Pergamon. [1.2](#), [2.5](#)
- AVALOSSE, T. & CROCHET, M. J. 1997a Finite-element simulation of mixing: 1. two-dimensional flow in periodic geometry. *AIChE Journal* **43** (3), 577–587. [1.1](#), [1.2](#)
- AVALOSSE, T. & CROCHET, M. J. 1997b Finite-element simulation of mixing: 2. three-dimensional flow through a Kenics mixer. *AIChE Journal* **43** (3), 588–597. [1.1](#), [1.2](#)
- BERTRAND, F., TANGUY, P. A. & THIBAUT, F. 1997 A three-dimensional fictitious domain method for incompressible fluid flow problems. *International Journal for Numerical Methods in Fluids* **25** (6), 719–736. [5.4](#)
- BOOY, L. M. 1978 Geometry of fully wiped twin-screw equipment. *Polymer Engineering and Science* **18** (12), 973–984. [5.3](#)
- BOOY, L. M. 1980 Isothermal flow of viscous liquids in corotating screw devices. *Polymer Engineering and Science* **20** (18), 1220–1228. [5.3](#)
- CAREY, G. F. & SHEN, Y. 1995 Simulation of fluid mixing using least-squares finite elements & particle tracing. *International Journal for Numerical Heat and Fluid Flow* **5**, 549–573. [1.2](#)
- CHELLA, R. & VIÑALS, J. 1996 Mixing of a two-phase fluid by cavity flow. *Physical Review E* **53** (4), 3832–3840. [2.1](#)
- CHEN, Z. & WHITE, J. L. 1994 Dimensionless non-Newtonian isothermal simulation and scale-up considerations for modular intermeshing corotating twin screw extruders. *International Polymer Processing* **VI** (4), 304–310. [5.3](#)
- CHIEN, W. L., RISING, H. & OTTINO, J. M. 1986 Laminar mixing and chaotic mixing in several cavity flows. *Journal of Fluid Mechanics* **170**, 355–377. [1.4](#), [2.1](#)

- DANCKWERTS, P. V. 1952 The definition and measurement of some characteristics of mixtures. *Applied Scientific Research Section A* **3**, 279–296. 1.3, A, A, A
- DANCKWERTS, P. V. 1953 Continuous flow systems; distribution of residence times. *Chemical Engineering Science* **2** (1), 1–13. 1.3
- ELEMANS, P. H. M. & MEIJER, H. E. H. 1990 Approaches to the modelling of mixing equipment. In *Encyclopedia of Fluid Mechanics* (ed. N. P. Chermisinoff), vol. 9. Polymer Flow Engineering, pp. 360–371. Houston: Gulf Publishing Company. 5.4, 5.7
- FRANJIONE, J. G., LEONG, C.-W. & OTTINO, J. M. 1989 Symmetries within chaos: A route to effective mixing. *Physics of Fluids. A, Fluid Dynamics* **1** (11), 1772–1783. 1.1, 2.5, 3.5.2
- FRANJIONE, J. G. & OTTINO, J. M. 1992 Symmetry concepts for the geometric analysis of mixing flows. *Philosophical Transactions of the Royal Society of London A* **338**, 301–323. 1.1
- FUNATSU, K., KATSUKI, S., TAKAYAMA, T. & KIHARA, S. 1999 3D numerical analysis on the effects of combination of forward and backward screw elements in twin screw extruders. In *Proceedings of the Fifteenth Annual Meeting of the Polymer Processing Society* (ed. P. G. M. Kruijt & P. D. Anderson). 5.1
- GALAKTIONOV, O. S., ANDERSON, P. D. & PETERS, G. W. M. 1997 Mixing simulations: tracking strongly deforming fluid volumes in 3D flows. In *Proceedings of The Fourth European PVM-MPI Users' Group Meeting*, vol. 1332, pp. 463–496. Springer Verlag. 1.1, 1.4, 2.4.1, 3.2
- GALAKTIONOV, O. S., ANDERSON, P. D., PETERS, G. W. M. & TUCKER, III, C. L. 2000a A global, multi-scale simulation of laminar fluid mixing: The extended mapping method. *International Journal of Multiphase Flow* (submitted, temporarily available from <http://polypro.me.uiuc.edu/online.html>). 2.6, 6.2, C
- GALAKTIONOV, O. S., ANDERSON, P. D., PETERS, G. W. M. & VAN DE VOSSE, F. N. 2000b An adaptive front tracking technique for three-dimensional transient flows. *International Journal for Numerical Methods in Fluids* **32** (2), 201–218. 1.1, 1.1, 1.4, B.1
- GALAKTIONOV, O. S., MELESHKO, V. V., PETERS, G. W. M. & MEIJER, H. E. H. 1999 Stokes flow in a rectangular cavity with a cylinder. *Fluid Dynamics Research* (24), 81–102. 1.2
- GEIST, A., BEGUELIN, A., DONGARRA, J., JIANG, W., MANCHEK, R. & SUNDERMAN, V. 1994 *PVM: Parallel Virtual Machine. A user's guide and tutorial for networked parallel computing*. Cambridge, Massachusetts: The MIT Press. 2.4.1, 3.3
- GLOWINSKI, R., PAN, T.-W. & PERIAUX, J. 1994a A fictitious domain method for Dirichlet problem and applications. *Computer Methods in Applied Mechanics and Engineering* **111**. 5.4

- GLOWINSKI, R., PAN, T.-W. & PERIAUX, J. 1994*b* A fictitious domain method for external incompressible viscous flow modeled by Navier-Stokes equations. *Computer Methods in Applied Mechanics and Engineering* **112**. 5.4
- GRADSHTEYN, I. S. & RYZHIK, I. M. 1994 *Table of Integrals, Series, and Products*, 5th edn. New York: Academic Press. D
- HIRT, C. V. & NICHOLS, B. D. 1981 Volume of fluid (VOF) methods for the dynamics of free boundaries. *Journal of Computational Physics* **39**, 201–225. 1.1, 1.2
- HOBBS, D. M. & MUZZIO, F. J. 1997 Effects of injection location, flow ratio and geometry on Kenics mixer performance. *AIChE Journal* **43** (12), 3121–3132. 1.1
- VAN DER HOEVEN, J. C., WIMBERGER-FRIEDL, R. & MEIJER, H. E. H. 2000 Homogeneity of multilayers produced with a static mixer. *Polymer Engineering Science* (accepted). 1.4, 4.1, 4.4
- HUTCHINSON, B. C., RIOS, A. C. & OSSWALD, T. A. 1999 Modeling the distributive mixing in an internal batch mixer. *International Polymer Processing* **XIV** (4), 315–321. 1.2, 5.1
- JANA, S. C., METCALFE, G. & OTTINO, J. M. 1994*a* Experimental and computational studies of mixing in complex Stokes flows: The vortex mixing flow and multicellular cavity flows. *Journal of Fluid Mechanics* **269**, 199–246. 2.1, 2.5
- JANA, S. C., TIAHJADI, M. & OTTINO, J. M. 1994*b* Chaotic mixing of viscous fluids by periodic changes in geometry: Baffled cavity flow. *AIChE Journal* **40** (11), 1769–1781. 1.1
- LEHMER, D. H. 1950 Approximations to the area of an n -dimensional ellipsoid. *Canadian Journal of Mathematics* **2**, 267–282. D
- LEONG, C. W. & OTTINO, J. M. 1989 Experiments on mixing due to chaotic advection in a cavity. *Journal of Fluid Mechanics* **209**, 463–499. 2.1
- LEONG, C. W. & OTTINO, J. M. 1990 Increase in regularity by polymer addition during chaotic mixing in two-dimensional flows. *Physical Review Letters* **64** (8), 874–877. 2.1
- LING, F. H. 1994 Interpolated Poincaré map and application to mixing problems. *Chaos, Solitons & Fractals* **4** (5), 681–692. 1.1
- MADAY, Y. & PATERA, A. T. 1989 Spectral element methods for the incompressible Navier-Stokes equations. In *State-of-the-Art surveys on computational mechanics* (ed. A. Noor). New York: ASME. 3.2, 4.2
- MEIJER, H. E. H. & ELEMANS, P. H. M. 1988 Modelling of continuous mixers; part 1: the corotating twin screw extruder. *Polymer Engineering Science* **5** (28), 275–290. 5.4, 5.7

- MEIJER, H. E. H. & ELEMANS, P. H. M. 1990 Modelling of continuous mixers; the corotating twin screw extruder. In *Encyclopedia of Fluid Mechanics* (ed. N. P. Cheremisinoff), vol. 9. Polymer Flow Engineering, pp. 372–402. Houston: Gulf Publishing Company. 5.4, 5.7
- MELESHKO, V. V. 1994 Nonstirring motion of an inviscid fluid by a point vortex in a rectangle. *Physics of Fluids* **6** (1), 6–8. 2.1
- MELESHKO, V. V. & PETERS, G. W. M. 1996 Periodic points for two-dimensional Stokes flow in a rectangular cavity. *Physics Letters A* **216**, 87–96. 1.1, 1.2, 2.1
- MOFFATT, H. K. 1964 Viscous and resistive eddies near a sharp corner. *Journal of Fluid Mechanics* **18** (1), 1–18. 4.1
- MOHR, W. D., SAXTON, R. L. & JEPSON, C. H. 1957 Mixing in laminar flows. *Industrial and Engineering Chemistry* **49** (11), 1855–1856. A.1
- MUZZIO, F. J., MENEVEAU, C., SWANSON, P. D. & OTTINO, J. M. 1992 Scaling and multifractal properties of mixing in chaotic flow. *Physics of Fluids. A, Fluid Dynamics* **4** (7), 1439–1456. 2.3
- NOH, W. F. & WOODWARD, P. 1976 SLIC (simple line interface calculation). In *Lecture Notes in Physics* (ed. A. I. van de Vooren & P. J. Zandbergen), *Numerical methods in fluid dynamics*, vol. VII, pp. 330–340. New York: Springer. 1.1, 1.2
- OTTINO, J. M. 1989 *The kinematics of mixing: stretching, chaos and transport*. Cambridge University Press. 1.1, 1.2, 2.3, 2.5
- OTTINO, J. M., TJAHHADI, M., FRANJIONE, J. G., JANA, S. C. & KUSCH, H. A. 1992 Chaos, symmetry and self-similarity: Exploiting order and disorder in mixing processes. *Science* **257**, 754–760. 1.2
- POTENTE, H., ANSAHL, J. & KLARHOLZ, B. 1994 Design of tightly intermeshing corotating twin screw extruders. *International Polymer Processing* **IX** (1), 11–25. 5.3
- QU, X. & LI, X. 1996 A 3D surface tracking algorithm. *Computational Vision Graphics Image Processing* **64**, 147–156. 3.4
- VAN RENS, B. J. E. 1999 Finite element simulation of the aluminum extrusion process. PhD thesis, Eindhoven University of Technology. 5.4, 5.4, 6.2
- RUDMAN, M. 1997 Volume-tracking methods for interfacial flow calculations. *International Journal for Numerical Methods in Fluids* **24**, 671–691. 1.1, 1.2, 3.4
- SLUIJTERS, R. 1965 Het principe van de multiflux menger. In *De Ingenieur, Chemische Techniek* 3, vol. 77, pp. Ch 33–36. In Dutch. 1.4, 4.1, 4.1
- SOUVALIOTIS, A., JANA, S. C. & OTTINO, J. M. 1995 Potentialities and limitations of mixing simulations. *AIChE Journal* **41** (7), 1605–1621. 1.1

- SPENCER, R. S. & WILEY, R. M. 1951 The mixing of very viscous liquids. *Journal of Colloid Science* **6**, 133–145. 1.1, 2.4.1
- SZYDLOWSKI, W. & WHITE, J. L. 1988 Improved model of flow in the kneading disc region of an intermeshing co-rotating twin screw extruder. *International Polymer Processing II* (3/4), 142–150. 5.1
- TADMOR, Z. & GOGOS, C. 1979 *Principles of Polymer Processing*. New York: Wiley. 1.1
- TIMMERMANS, L. J. P., MINEV, P. D. & VAN DE VOSSE, F. N. 1996 An approximate projection scheme for incompressible flow using spectral elements. *International Journal for Numerical Methods Fluids* **22**, 673–688. 3.2, 4.2
- TUCKER, III, C. L. 1981 Sample variance measurement of mixing. *Chemical Engineering Science* **36** (11), 1829–1839. 1.3
- TUCKER, III, C. L. 1991 Principles of mixing measurement. In *Mixing in polymer processing* (ed. C. Rauwendaal), pp. 101–127. New York: Marcel Dekker Inc. 1.3, A
- WARD-SMITH, A. J. 1980 *Internal fluid flow; the fluid dynamics of flow in pipes and ducts*. Oxford: Clarendon Press. 4.2
- WELANDER, P. 1955 Studies on the general development of motion in a two-dimensional, ideal fluid. *Tellus* **7** (2), 141–156. 1.3, 2.4.1, A
- WETZEL, E. D. & TUCKER, III, C. L. 1997 Area tensors for modeling morphology during laminar liquid-liquid mixing. Technical report UILU-ENG 97-4014. University of Illinois. 2.6, 5.7, C
- WETZEL, E. D. & TUCKER, III, C. L. 1999a Area tensors for modeling microstructure during laminar liquid-liquid mixing. *International Journal of Multiphase Flow* **25** (1), 35–61. 2.6, C, C, C, D, D
- WETZEL, E. D. & TUCKER, III, C. L. 1999b Area tensors for modeling microstructure during laminar liquid-liquid mixing. *Journal of Fluid Mechanics* (submitted, temporarily available from <http://polypro.me.uiuc.edu/online.html>). 2.6, C, C, D
- WONG, T. H. & MANAS-ZLOCZOWER, I. 1994 Two-dimensional dynamic study of the distributive mixing in an internal mixer. *International Polymer Processing IX* (1), 3–10. 5.1
- YANG, H. H. & MANAS-ZLOCZOWER, I. 1992 3-D flow field analysis of a Banbury mixer. *International Polymer Processing VII* (3), 195–203. 5.1
- YANG, H.-H. & MANAS-ZLOCZOWER, I. 1994 Analysis of mixing performance in a VIC mixer. *International Polymer Processing IX* (4), 291–302. 5.1

Samenvatting

Dit proefschrift betreft de analyse van laminair mengen. Mengen komt zowel voor in de industrie als in het huishouden. Mengen in de industrie behelst onder andere toepassingen in polymer blends, fabricage van verf en inkt en in de bereiding van voedsel. In het huishouden komen we laminair mengen tegen bij het maken van deeg voor brood of cake, het bereiden van sauzen, gedurende het koken en in het roeren van stroop of honing in yoghurt.

Mengen is zo alledaags dat het zonder nadenken wordt gedaan. Desondanks ondervindt de industrie moeilijkheden die om een beter begrip van mengprocessen vragen. Productiesnelheden worden opgevoerd, er worden andere materialen verwerkt die temperatuurgevoelig zijn en degraderen, terwijl ook de productievolumes verhoogd worden, zodat er steeds minder tijd overblijft om goed te mengen. Daarnaast worden de eisen die gesteld worden aan het uiteindelijke product steeds hoger. Bovenstaande argumentatie vormt de voornaamste reden waarom analyse van mengen van belang is.

Wanneer we ons beperken tot die gevallen waarbij de reologie van het mengsel niet verandert door het mengen, begint de analyse van het mengen daar waar de analyse van het snelheidsveld in een menger ophoudt. Zelfs voor de complexe vormen in de mengers die in de praktijk gebruikt worden kan dit snelheidsveld tegenwoordig met grote nauwkeurigheid numeriek bepaald worden. Alle bestaande methoden om menggedrag numeriek te analyseren maken gebruik van technieken om deeltjes in de tijd te volgen. Klassieke methoden, zoals bijvoorbeeld de Poincaré methode, volgen in het algemeen een beperkt aantal kleine deeltjes die geen fysieke afmetingen hebben. Wanneer de deeltjes wel een grootte hebben, zoals bijvoorbeeld bij het volgen van randen van oppervlaktes of volumes (blobs), dan is het resultaat vrijwel altijd afhankelijk van de beginpositie van de blob, alsmede van de grootte en vorm van die blob. Wanneer men te maken heeft met een redelijk efficiënte menger, zal het aantal punten dat nodig is om de rand van een blob te beschrijven, exponentieel toenemen. Het volgen van de rand voor langere tijd is dus duur in termen van computertijd en computergeheugen en wordt, ondanks toepassing van adaptieve technieken, bij exponentiële toename van de lengte van de rand, al na geringe (meng-)tijd onmogelijk. Als vervolgens wijzigingen worden aangebracht in de geometrie of het mengprotocol, dient de gehele analyse herhaald te worden. Het behoeft geen betoog dat het optimaliseren van mengers op deze wijze geen haalbare zaak is.

De ‘afbeeldingen-’ of mapping-methode die in dit proefschrift beschreven wordt verschilt niet van de klassieke methode in zoverre dat ook deze methode gebruik maakt van technieken om deeltjes te volgen. Echter, in plaats van analyse van de verspreiding van losse deeltjes in de vloeistofstroom of het volgen van de rand van een enkele blob na te streven, berekent de methode het transport van vloeistof (of een andere behoudende of additieve grootte zoals verblijftijd of de grootte van het oppervlak tussen twee vloeistoffen) gedurende een beperkte mengtijd. De totale mengtijd wordt daartoe opgedeeld in een (groot) aantal karakteristieke deelmengtijden. Het te analyseren mengdomein wordt opgedeeld in een groot aantal subdo-

meintjes. De randen van deze subdomeintjes worden gedurende een (deel van de) periode van de stroming gevolgd. Hierbij hoeft geen onderscheid gemaakt te worden tussen tijd- of plaatsperiodieke stromingen. Vervolgens wordt van elk gevolgd subdomeintje bepaald welke originele subdomeintjes het doorsnijdt. De grootte van deze doorsnijding wordt opgeslagen in een transport-matrix. Deze matrix beschrijft dus hoeveel vloeistof er van een subdomein er na verloop van een bepaalde tijd in andere subdomeintjes terecht komt. Gebruikmakend van deze afbeeldingen-methode kan bijvoorbeeld de invloed van de initiële plaats van een blob op de uiteindelijke verspreiding van die blob eenvoudig berekend worden aangezien deze berekening gereduceerd is tot een eenvoudige (ijle) matrix-vector vermenigvuldiging. Door de matrix-vector vermenigvuldiging nu een (eventueel groot) aantal keer achtereenvolgend te herhalen, wordt het mengproces gemodelleerd.

De gepresenteerde afbeeldingen-methode laat een aantal bezwaren van klassieke methodes links liggen. Het belangrijkste voordeel bestaat eruit dat niet elke wijziging in protocol of geometrie een volledig nieuwe analyse vergt. Omdat de afbeeldingen-methode een 'lineaire' methode is, kan het stroomdomein opgedeeld worden in een aantal kleinere domeinen die onafhankelijk van elkaar geanalyseerd kunnen worden. Deze afzonderlijk geanalyseerde functionele eenheden kunnen dan later gecombineerd worden om het volledige domein, en variaties daarop, te analyseren. Dit maakt de methode met name geschikt voor bijvoorbeeld de analyse van extruder-schroeven. De afzonderlijke delen van een extruderschroef kunnen apart geanalyseerd worden en vervolgens in verschillende schroefontwerpen gecombineerd worden zodat de werking van de gehele schroef beschouwd kan worden.

Dit proefschrift introduceert de afbeeldingen-methode aan de hand van een eenvoudige twee-dimensionale tijdperiodieke prototype-stroming: die van een caviteit waarvan twee tegenoverliggende wanden onafhankelijk van elkaar bewogen kunnen worden en zo een stroming in de caviteit teweegbrengen. Deze stroming wordt al geruime tijd onderzocht en dit geeft de mogelijkheid de resultaten te vergelijken met eerder werk. Om de toepasbaarheid uit te breiden naar drie dimensies is een tweede prototype-stroming onderzocht door de twee-dimensionale caviteit-stroming uit te breiden naar drie dimensies: een kubus waarvan twee tegenoverliggende vlakken onafhankelijk van elkaar kunnen bewegen. De eerste stap die gemaakt is naar industriële mengers betreft de analyse van de plaats-periodieke multflux statische menger. Tenslotte wordt het transport-element van een gelijkdraaiende dubbelschroef-extruder geanalyseerd.

Summary

In this thesis the issue of mixing analysis is addressed. Mixing is found in industrial and domestic practice. Examples of the first include applications in polymer reaction engineering, polymer blending, food manufacturing, paint and ink preparations, while those of the second are involved in preparing dough for baking cake or bread, in mixing of sauces and in cooking, up to the stirring of syrup in yoghurt.

Mixing has become such an integral part of everyday life, that it is performed without thought. However, in industry, it has become clear that mixing needs to be better understood. Residence times are continuously decreasing in order to be able to also process temperature sensitive materials and to reach a higher production volume with imposed properties of the resulting product, despite the complexity caused by the choice of the individual constituents. The time allowed to find the proper mixing actions has become increasingly smaller, the demands are increasingly more severe.

Restricting to those cases where rheology is not changed through the mixing action, analysis of mixing starts where the computation of velocity fields ends (even in complex geometries as generally involved in practical mixers). Once an accurate velocity field is obtained, it can be used to investigate the mixing properties of the flow at hand. Methods applied to analyse mixing without exception use some kind of particle tracking technique. Classical methods, as e.g. the Poincaré method, usually only track infinitely small particles, with no physical size attached. When a physical size is attached, as e.g. boundary or volume tracking techniques, the results with respect to mixing quality tend to strongly depend on the location initially chosen and on the size of the area or volume of the traced blob. In the case of efficient (chaotic) mixing, the length of the boundary of this blob will increase exponentially, as will the number of markers to adequately describe the boundary. To track these boundaries for longer times is expensive in time as well as computer memory. Furthermore, when changes are made to the geometry or mixing protocol, analyses need to be repeated over and over again. Using such an approach, optimization in complex geometries is thus practically impossible.

The mapping method presented in this thesis is not different from the classical methods in the sense that it also uses particle tracking. However, instead of analysing the distribution of individual particles or a boundary of a two- or three-dimensional blob, the mapping method gives an approximate description of the transport of fluid or any other conservative or additive quantity (as e.g. residence time or interfacial area). This is realized by subdividing the flow domain into a number of subdomains. The boundaries of these subdomains are tracked for (a part of) a period of a flow. Both time and spatially periodic flows can be used. The intersection of the tracked subdomains with the initial subdomains is computed and stored in a transport matrix. This transport matrix identifies how much fluid flows from one subdomain to another during a pre-determined interval in time or space. Using this (mapping) matrix, the dependence of e.g. the final dye distribution on the initial dye distribution can easily be

computed, since it has been reduced to a (sparse) matrix–vector multiplication.

This mapping method overcomes a number of drawbacks of classical methods. Most important is the possibility to re-use the results of earlier computations: not every change in protocol or geometry requires a completely new analysis. Since the mapping method presented is a ‘linear’ method, the flow domain can be subdivided into a number of functional units, that can be analysed piecewise. The independent analyses can later be combined to analyse the entire flow domain, and variations upon it. This makes the method extremely useful for mixing devices as e.g. extruders. The separate screw-elements can be analysed independently, and afterwards combined into different screw designs, so the overall mixing performance of the screw can be analysed.

This thesis introduces the mapping method by means of a simple two-dimensional, time-periodic, lid-driven, cavity flow. This flow is well studied and offers possibilities to verify results in a number of ways. Extension of the applicability of the method towards flows in three dimensions is realized by investigating its potential via computations and verifications in a three-dimensional, lid-driven, time-periodic cavity flow. The first step towards industrial, spatially periodic, mixers is made by analysing the multiflux static mixer. Finally the transport element of the co-rotating twin screw extruder is analysed.

Acknowledgements

As with any four or five year project, the results are not the work of just one person. This also holds for the ‘Prototype Mixing Flows’ project, part of which is presented in this thesis. Even more so, since from the beginning of the project at least two, and at some point during the project, even six people were working full-time on it.

I would like to thank Patrick Anderson for implementing spectral elements in the finite element code, the occasional lunch meetings in the city, and for being around the office. Last half year promised to be six months in ‘solitude’. This was prevented by Alexei (or, since the last few years Oleksiy) Galaktionov, whom I need to thank not just for being around, but especially for the numerous lines of code needed for tracking and mapping, and the, sometimes heated, discussions. Discussions I also had with Gerrit Peters, who came up with the idea of mapping and who, at some times, was a perfect ‘devils advocate’ that made me think about things I took for granted.

I was assisted by two graduate students: Frank Schepens and Hervé Camerlynck, the last one from the Université Catholique de Louvain. Despite your efforts, not much of your work has made the thesis: intended to be of an experimental nature, it made a 180° turn to fully numerical. Nevertheless, your work has been useful to me. I also need to thank dr Meleshko and dr Krasnopolskaya for introducing me to chaos in flows and providing an analytical solution to our test case problem.

Op het persoonlijke vlak gaat mijn dank uit naar mijn ouders, die mij altijd in de gelegenheid hebben gesteld te leren, en altijd achter mij gestaan hebben. Zonder jullie was deze persoonlijke mijlpaal niet gehaald. Ook Yvonne verdient een woord van dank, al was het alleen maar omdat ze het laatste jaar met mij heeft uitgehouden. Verder wil ik iedereen bedanken die ‘in de buurt’ was tijdens de koffie- en lunchpauzes en waarmee menige zinnige en zinloze discussie gevoerd is. Ook Leo Wouters en Patrick van Brakel vallen hieronder, maar zij verdienen bovendien nog een vermelding als vraagbaak voor alle PC-perikelen op het werk en thuis.

Peter Kruijt

Eindhoven, mei 2000

Curriculum Vitae

3 januari 1969 Geboren te Gilze en Rijen
1981–1987 Theresialyceum Tilburg
1987–1988 Studie Elektrotechniek aan de TU Eindhoven
1988–1994 Studie Werktuigbouwkunde aan de TU Eindhoven
1995–2000 Assistent in opleiding in de sectie Materials Technology, TU Eindhoven

Stellingen

behorende bij het proefschrift

Analysis and Optimization of Laminar Mixing Flows

Design, Development and Application of the Mapping Method

1. De methode voor de analyse van menging zoals voorgesteld door Spencer en Wiley (1951) heeft haar merites, maar is voor de analyse van industriële mengers nog steeds ongeschikt door de grote hoeveelheid benodigd computergeheugen. De mapping methode gepresenteerd in dit proefschrift gaat weliswaar terug naar dezelfde basisgedachte, maar heeft de genoemde beperking niet, en geeft de mogelijkheid tot optimalisatie.
 - SPENCER, R. S. & WILEY, R. M. 1951 The mixing of very viscous liquids. *Journal of Colloid Science* **6**, 133–145.
 - Dit proefschrift.
2. Bestaande technieken voor de analyse van menging maken veelal gebruik van de distributie van een eindig aantal infinitesimale tracers. Daar deze tracers geen fysische dimensies bezitten is de interpretatie van de resultaten verkregen door toepassing van deze technieken een hachelijke zaak. Het volgen van gebieden met een eindige grootte verdient daarom de voorkeur. Dat dit een wezenlijk verschil is wordt onvoldoende onderkend.
 - Dit proefschrift, Hoofdstuk 2.
3. Ervan uitgaande dat de meeste mengprocessen intrinsiek herhalend zijn (en dus periodiek), moet de berekening van één periode voldoende zijn voor de analyse van de mengwerking van een menger. Dit kan leiden tot een reductie van de rekentijd. Daar één periode vaak nog uit een combinatie van gelijksoortige operaties bestaat kan de rekentijd verder worden teruggebracht door slechts de effecten van één operatie te berekenen.
 - Dit proefschrift, Hoofdstuk 2 en 3.

4. De mogelijkheid een mengproces te reduceren tot een beperkt aantal discrete handelingen is essentieel voor optimalisatie van het mengproces. Door de beschrijving van het transport van vloeistof tijdens een dergelijke handeling terug te brengen tot een matrix–vector vermenigvuldiging, is optimalisatie van complexe mengers ook realiseerbaar geworden.
 - Dit proefschrift.
5. Kwalificatie van menging met behulp van mengmaten is alleen zinnig wanneer men kan definiëren wat voor het mengsel onder beschouwing van wezenlijk belang is. Het zoeken naar één mengmaat die in alle gevallen voldoet is daarom dan ook verspilde moeite.
 - MOHR, W. D., SAXTON, R. L. & JEPSON, C. H. 1957 Mixing in laminar flows. *Industrial and Engineering Chemistry* **49** (11), 1855–1856.
 - DANCKWERTS, P. V. 1952 The definition and measurement of some characteristics of mixtures. *Applied Scientific Research Section A* **3**, 279–296.
6. Vaak is bepaling van het snelheidsveld het einde van een numerieke analyse. Bij mengen is het pas het begin.
7. Veel numeriek werk is heden ten dage experimenteel van aard.
8. Het laten vervallen van de voorgestelde HTML 3.0 standaard waarin de mogelijkheid tot het weergeven van formules door browsers werd beschreven geeft enerzijds weer dat de correcte weergave van formules niet eenvoudig is, maar anderzijds ook dat ‘het web’ steeds meer het domein van de commercie wordt dan van de wetenschap. De moeizame totstandkoming van MathML (Mathematical Markup Language) en de ondersteuning daarvan door moderne browsers onderstreept dit.
 - HyperText Markup Language Specification Version 3.0.
<http://www.w3.org/MarkUp/html3/math.html>.
 - HTML 3.2 Reference Specification.
<http://www.w3.org/TR/REC-html32.html>.
9. De uitwisselbaarheid van Word-documenten wordt beperkt door zowel versienummer als taalgebied, ook wanneer het documenten met slechts engelse tekst betreft. Wanneer figuren of formules in het document aanwezig zijn vermindert de uitwisselbaarheid dramatisch.
 - *Proceedings of the Fifteenth Annual Meeting of the Polymer Processing Society* ed. P. G. M. Kruijt & P. D. Anderson (on CD-ROM).
10. Parallel rekenen kan de kloktijd van een simulatie bijzonder verkorten. Dit heeft echter geen relatie met de promotieduur.
 - Dit proefschrift, pag. 101.

Peter Kruijt,
Eindhoven 5 september 2000.

4.

